Direct and Indirect Probing of Higher-Lying Excited-States of Photoactive Molecules

By

Timothy James Quincy

Submitted to the graduate degree program in Department of Chemistry and the Graduate Faculty of the University of Kansas in partial fulfillment of the requirements for the degree of Doctor of Philosophy.

Committee members

Christopher G. Elles, Chairperson

Cindy L. Berrie

Carey K. Johnson

Timothy A. Jackson

Craig P. Marshal

Date defended: August 09, 2018

The Thesis Committee for Timothy James Quincy certifies
that this is the approved version of the following thesis :

Direct and Indirect Probing of Higher-Lying Excited-States of Photoactive Molecules

Christopher G. Elles, Chairperson

Date approved: August 09, 2018

Abstract

It is often assumed that optically accessible excited-states above S_1 play only a marginal role in the photochemistry and photodynamics of molecular systems. However, many classes of molecules have been found in which the higher-lying electronic states above S_1 can significantly impact the photochemistry as it occurs on the S_1 potential energy surface. Using the resonance condition associated with transient Raman spectroscopy, the higher-lying excited-states are probed directly via the vibration specific enhancements. The vibrational enhancements reveal the forces that the higher-lying resonant state applies in terms of the vibrational coordinates. In turn, the vibrational enhancements directly probe how the electronic potential shifts between the two electronic states, leading to optical control of the excited-state dynamics. Pump-probe and pump-repump-probe spectroscopies indirectly probe higher-lying states by showing the overall impact when those states are accessed either by directly via one-photon excitation or by sequential multiphoton excitation. By combining transient electronic and vibrational spectroscopies, a detailed picture of the excited-state landscape emerges with dynamic information about the higher-lying electronic states.

In this dissertation, the role and structure of higher-lying excited electronic states are studied to understand how those states provide selective optical control. The photoactive molecules studied in this dissertation are related to diarylethene-based photoswitches. These photoswitches provide interesting photochemistry to study with these spectroscopic methods, and a detailed understanding of the optical control of these molecules will aid in their integration into optically active material systems. The primary photoswitch of study is 1,2-bis(2,4-dimethyl-5-phenyl-3-thienyl) perfluoro-

cyclopentene (DMPT-PFCP) which reversibly isomerizes following irradiation and acts as a model system to study photochemical dynamics. Two additional photochromic switches and a phenylthiophene derivative related to the aryl side groups of DMPT-PFCP are investigated to study the effect of structural changes on the excited-state dynamics.

Acknowledgements

First, I would like to thank my advisor, Chris Elles, for his patience and guidance over the last five years as I've developed as a researcher and scientist. His enthusiasm has always been contagious and helped me to find my drive to push my research forward even when the way was unclear. I'm also thankful to Chris for providing opportunities to present our research at a variety of scientific venues and meet many excellent researchers in the process. I am genuinely thankful for the time and energy he has invested in me to help me reach my career and life goals beyond KU.

Next, I would like to thank all of the members of the Elles research group. Especially Dr. Cassie Ward, Dr. Amanda Houk, Jenna Lindsey, Chris Otolski, Matt Barclay, David Stierwalt, Kristen Burns, Sadegh Mahvidi, Emmaline Lorenzo, and Whitney Harmon. All of helped me produce this work through stimulating discussions and simple questions that drove me to consider my research from different perspectives. Also, the time spent commiserating when experiments proved unexpectedly difficult and celebrating victories made the path through graduate school that much easier.

I would also like to thanks my family and friends for their support and understanding throughout my graduate career. At many times over the last five years, I have needed to prioritize my graduate work, and they have consistently provided encouragement and rooted for my success. Most importantly I would like the thank my wife, Marcy Quiason, who has made my graduate career possible. I'm incredibly lucky to have you be part of my life.

Contents

List of Figures **ix**

List of Tables **xii**

1 Introduction **1**

1.1 Exploration of Higher-Lying Electronic Excited-States 1

1.1.1 Probing the Dynamics of Higher-Lying Excited-States 2

1.2 Photoactive Molecular Systems 4

1.2.1 2,5-Diphenylthiophene 4

1.2.2 Diarylethene-Based Photoswitch 5

1.3 Dissertation Overview 7

1.4 Bibliography 10

2 Experimental Methods **18**

2.1 Overview 18

2.2 Transient Absorption Techniques 19

2.3 Resonance Femtosecond Stimulated Raman Spectroscopy (R-FSRS) 20

2.3.1 Picosecond Raman Pump Generation 21

2.3.2 Spectral filter 23

2.3.3 CCD Detector 25

2.3.3.1 Labview integration for PP and FSRS experimentation 25

2.3.3.2 Array Synchronization 26

2.3.3.3 Frequency shifting 27

2.3.4 Data Analysis 29

2.3.4.1 Solvent Calibration 29
2.3.4.2 Baseline Correction 30
2.3.4.3 Solvent Subtraction Correction 32
2.4 Sample Preparation 33
2.5 Bibliography 35

3 Probing Higher-Lying Electronic States with Mode-Specific Excited-State Resonance Raman Spectroscopy 38

3.1 Introduction 38
3.2 Theory 40
3.3 Methods 44
3.3.1 Experimental Details 44
3.3.2 Computational Details 45
3.4 Results 46
3.4.1 Excited-State Dynamics 46
3.4.2 Excited-State Resonance Raman 49
3.4.3 Raman Excitation Profiles 54
3.4.4 Calculated Excited-State Resonance Raman Spectra 57
3.5 Discussion 62
3.6 Conclusions 64
3.7 Appendix 65
3.8 Bibliography 68

4 Directly Probing the Dynamics of Higher-Lying Excited-States in a Diarylethene-based Molecular Switch by Femtosecond Stimulated Resonance Raman Spectroscopy 76

4.1 Introduction 76
4.2 Experimental Methods 78
4.3 Results 81

4.4 Discussion . . . 93
4.5 Conclusion . . . 96
4.6 Bibliography . . . 97

5 Wavelength Dependent Dynamics of Cycloreversion in a Diarylethene-based Photoswitch 101

5.1 Introduction . . . 101
5.2 Experimental . . . 102
5.3 Results . . . 103
5.4 Discussion . . . 109
5.5 Conclusions . . . 113
5.6 Bibliography . . . 114

6 Photoswitching in Diverse Diarylethene Derivatives 117

6.1 Introduction . . . 117
6.2 Experimental . . . 118
6.3 Results and Discussion . . . 119
6.3.1 TPDC Dynamics . . . 119
6.3.1.1 TPDC Cycloreversion . . . 119
6.3.1.2 TPDC Cyclization . . . 122
6.3.2 DTA Cyclization Dynamics . . . 125
6.4 Conclusions . . . 129
6.5 Bibliography . . . 130

7 Conclusions 133

7.1 Bibliography . . . 138

List of Figures

1.1 Structure of 2,5-Diphenylthiophene 5

1.2 Structures of Diarylethene photoswitches 6

2.1 Laser Fundamental and Spectrally Compressed Second Harmonic Spectra 22

2.2 Diagram of Spectral Filter 24

2.3 Pulse Detection of CCD vs SPD 26

2.4 CCD Trigger Timing 27

2.5 Frequency Shifting Correction 29

2.6 Baseline Correction and Solvent Depletion 31

3.1 Evolution of Transient Absorption Spectrum of DPT 47

3.2 Evolution of FSRS spectrum of DPT 48

3.3 Experimental and Calculated Ground-State Raman Spectra 50

3.4 Experimental and Calculated Excited-State Raman Spectra 51

3.5 Excited-State Resonance Raman Spectra for Eight Different Excitation Wavelengths 54

3.6 Excitation Profiles of Excited-state Raman Bands 55

3.7 Comparison of Experimental Transient Absorbtion and Excited-State Raman Spectra With Spectra Simulated With TD-DFT 58

3.8 Comparison of Experimental Transient Absorption and Excited-State Raman Spectra With Spectra Simulated With EOM-CCSD 60

3.9 Electron Densisity Difference Map of DPT 61

3.10 Depolarization Ratios of DPT at Three Raman Pump Wavelengths 67

4.1 Potential Energy Diagram of Resonant Simulated Raman Process 78

4.2 Ground State Raman Spectrum of DMPT-PFCF 83
4.3 DMPT-PFCP Transient Absorption 85
4.4 Diagram of Relative Ground and Excited-State Absorption 86
4.5 Bleach Corrected R-FSRS Spectrum of DMPT-PFCP 87
4.6 DMPT-PFCP Excited-State Raman Evolution 89
4.7 Kinetic Traces of Select Vibration Bands of DMPT-PFCP 92

5.1 DMPT-PFCP Ground State Absorption Spectra 102
5.2 DMPT-PFCP Absorption Comparison with DMPT 104
5.3 DMPT-PFCP Orbitals for HOMO and LUMO orbitals 104
5.4 Sub-picosecond Transient Spectra and Kinetics of DMPT-PFCP 106
5.5 Transient Spectra and Kinetics of DMPT-PFCP 107
5.6 Normalized Transient Absorption Spectra 108
5.7 Triplet Absorption spectra in DMPT-PFCP 109
5.8 DMPT-PFCP Decay Associated Spectra 110
5.9 Kinetic Model for DMPT-PFCP cylization 112

6.1 Structure of TPDC 118
6.2 Structure of DTA and hydrogen bonding orientation 118
6.3 UV-Vis Spectrum of TPDC 120
6.4 TPDC Cycloreversion Spectra after excitation with a 500 nm pump pulse 121
6.5 TPDC Cycloreversion Kinetic Traces after 500 nm excitation 121
6.6 TPDC Cycloreverion Decay Associated Spectra 122
6.7 TPDC Cyclization Spectra 123
6.8 TPCD Cyclization Kinetic Trances 123
6.9 TPDC Cyclization Decay Associated Spectra 124
6.10 DTA UV-Vis spectra 125
6.11 DTA Transient Absorption 0-200fs 126

6.12 DTA Transient Absorption 200fs-2ps 126
6.13 DTA Cyclization Kinetic Cuts 127
6.14 DTA Cyclization Decay Associated Spectra 128
6.15 DTA TA and UVvis comparison 128

List of Tables

3.1 Assignment of Experimental Excited-State Raman Bands 53

4.1 Experimental and Calculated Raman Frequencies 82

4.2 Excited-State Vibrational Assignments of DMPT-PFCP 90

Chapter 1

Introduction

1.1 Exploration of Higher-Lying Electronic Excited-States

This dissertation describes vibrational and electronic spectroscopic measurements used to explore the impact of higher-lying excited-states in photoactivated molecules. Here we define higher-lying excited-states as electronic states above the first excited state which rapidly relax to S_1. Higher-lying excited-states have provided a means of controlling a variety of photochemical processes by linear excitation[1–3], simultaneous two-photon excitation[4–6], and gated, or sequential, two-photon excitation[2,3,7,8]. While the results of using higher-lying states to control reactivity are well documented in photochromic molecular switches[1–4,7–15], directly studying the dynamics of the higher-lying states is challenging. Part of this difficulty comes from the very short lifetimes of high-lying states due to the increasing density of electronic states, leading to Kasha's rule.[16] Ultrafast time-resolved pump-probe (PP) measurements can track the relaxation dynamics from directly excited electronic states, however, in many molecular systems, pump-repump-probe (PRePP), also called sequential two-photon excitation, experiments have shown that photo-initiated isomerizations can display greater quantum yields based on the time delay between excitation and re-excitation events.[1,3,7,8,10,12,13,17,18] Sequential excitation of diarylethene-based photoswitches is an excellent example of time-dependent control. The cycloreversion reaction of most diarylethene-based photoswitches is relatively inefficient but can be increased several times by re-excitation of the excited-state species.[2,19] This reactivity will be discussed in detail in later chapters.

1.1.1 Probing the Dynamics of Higher-Lying Excited-States

Ultimately, the combination of PP and PReP with time-resolved excited-state Raman spectroscopy provide a powerful collection of spectroscopic tools to examine and better understand the importance of higher-lying electronic excited-state in photochemical processes. To study the dynamics of higher-lying states, a secondary excitation pulse is introduced. The PReP measurement uses the second pump pulse to excite molecules to higher-lying states while monitoring the effect, or action, of the re-excitation in the long-time limit of the reaction. With the ability to scan the delay between the first and second pump pulses PReP provides a much more detailed description of the potential energy landscape.[10,14,15,20,21] Unfortunately, while PReP measurements offer more detailed information about the effects of the higher-lying states, the technique still probes those states indirectly by monitoring changes in bleach or product absorption bands. To directly probe these higher-lying electronic states, we employ resonant femtosecond stimulated Raman spectroscopy (R-FSRS).

As a vibrational spectroscopic technique, R-FSRS provides complementary information about vibrational motions compared to the electronic transition information provided by PP and PReP techniques.[22–27] Specifically, the resonance condition and vibrational mode specific enhancements provide information about the resonant higher-lying state in the Franck-Condon region.[28,29] To interpret the stimulated resonance Raman signals that originate from an electronically excited-state, we build off of the Raman theory developed by Albrecht, Heller, Myers Kelly, and Mathies, among others.[28–38]

While a brief description of the theory is provided here, a more detailed approach is presented in chapter 3. For our purposes, it is the electronic resonance condition which is most interesting because the vibrational spectroscopy has information about the higher-lying resonant state embedded in the vibrational intensities which are related to the potential of the higher-lying state.[28,39–43] Importantly this information is specific to the Franck-Condon region of the higher-lying surface. The sensitivity to the Franck-Condon region can be understood by examining the time-dependent description for resonance Raman scattering. We assume a single resonant state and describe the initial, time-dependent vibrational state as a Gaussian wavepacket. Raman scattering intensity for

a vibrational normal mode is proportional to the change in polarizability α, as the molecule moves along the normal mode coordinate. Furthermore, the polarizability is proportional to the vibrational overlap integral between the initial and final vibrational states. The force applied by the upper potential on vibrational wavepacket then increases the time-dependent overlap of the initial and final vibrational states, increasing the Raman scattering intensity.[28,29,31,36,39]

One key result is that the polarizability tensor is quadratically dependent on the transition dipole moment. Meaning even when ignoring the mode-specific enhancement, the transition dipole moment modulates the Raman scattering intensity. However, a more insightful result can be reached by careful consideration of the time-dependent overlap integral. By treating the overlap integral of the initial and final vibrational states, $\langle \nu_f | \nu_i(t) \rangle$, as a time-dependent wavepacket, classical dynamics can be used to relate the integral to the derivative of the upper potential energy surface.[28,44] While the complete mathematical description of Raman involves many terms, we restrict our discussion what is commonly described as the 'A' term which dominates under resonant conditions. In a classical dynamics picture, the wavepacket evolves based on the force applied to it and the force applied is going to be proportional to the gradient of the potential. Effectively, the time-dependent wavepacket will propagate further, and therefore have greater overlap with $|\nu_f\rangle$, when there is a larger gradient on the resonant electronic state potential. Importantly, the intensity of each Raman scattering vibrational mode is dependent upon the changes between the initial and upper electronic potential energy surface along the vibrational coordinate. In other words, the scattering intensity of a normal mode is proportional to the gradient of the upper potential with respect to its vibrational motion.[28] Therefore, the polarizability tensor is proportional to both the electronic transition strength (μ_{ni})and the gradient of the upper potential in terms of the vibrational coordinate ($\partial V / \partial Q_k$).

$$\alpha_{fi} \propto |\mu_{ni}|^2 \left(\frac{\partial V}{\partial Q_k} \right), \tag{1.1}$$

We can take advantage of this vibrational mode intensity dependence to directly probe the effects of higher-lying electronic states on the excited-state dynamics.

To properly interpret the mode-specific resonance enhancements of R-FSRS spectra, it is im-

portant to complement the experimental measurements with calculations of the vibrational normal modes. In an earlier paper, we used the R-FSRS technique to benchmark the calculations of a series of aryl-substituted thiophene derivatives.[45] The R-FSRS spectra of five phenylthiophene derivatives and three oligothiophenes were collected for both singlet and triplet electronic states. With the calculated vibrational normal modes from excited-state frequency calculations, careful consideration of the resonance condition is still required to avoid mis-assignments in the experimental resonant Raman spectrum. While the experimental R-FSRS spectra for the triplet species are similar to the off-resonance calculated spectrum, the singlet species display strong mode dependent enhancements. Both the vibrational symmetry and resonance enhancement provide a means to eliminate potential assignments and select the best candidate for vibrational assignments, even when a vibrational mode is a weak scatterer in the off-resonant calculations.

The information about the immediate influences of the higher-lying state combined with the longtime effects measured with PReP provides exceptional detail about the potential energy landscape of dynamic molecular systems. The R-FSRS mode specific enhancements indicate how the re-excitation affects the trajectory of the excited-state species along the multidimensional potential energy surface. PReP measurements show the impact of re-excitation on the yield of the photochemical reaction. By combining the PReP and R-FSRS, we identify vibrational motions that promote product formation and more clearly describe multidimensional reaction coordinates.

1.2 Photoactive Molecular Systems

1.2.1 2,5-Diphenylthiophene

The first molecular system studied in this dissertation is a phenylthiophene derivative, specifically 2,5-diphenylthiophene (DPT) shown in figure 1.1, which is considered a figurative building block of larger polymeric systems, that is used to study their electronic and optical behavior.

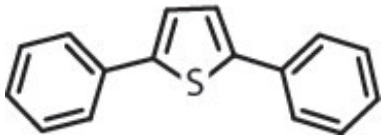

Figure 1.1: Structure of 2,5-Diphenylthiophene

Phenylthiophenes are broadly thought to be an excellent candidate for use as molecule wires and in optoelectronic devices such as LEDs and organic photovoltaics.[46–49] The conjugation and stability of these systems facilitates the charge and energy transport required by such devices. These applications inherently take advantage of the electronic excited states of the molecule, and therefore the electronic excited-states require detailed investigation.

One property of thiophene and phenylthiophene derivatives in solution is that in the ground-state the inter-ring dihedral angle is between 25° and 40 °.[50] However, after excitation to the first excited state, the rings become planar in small oligomers.[50–52] This planar geometry of the π-system increases the conjugation and its ability to transport charge. In addition, the planar geometry increases the overall polarizability of the molecule, providing strong Raman scattering in the excited-state. Furthermore, phenylthiophenes are a common building block in photochromic molecular switches, such as those studied in this dissertation and a thorough understanding of phenylthiophene relaxation mechanisms assist in the interpretation of the molecular switching dynamics.

1.2.2 Diarylethene-Based Photoswitch

The second type of system studied in this dissertation is diarylethene-based photoswitches (DAEs) which exhibit photochromic properties.[12,53–55] The photoswitching process in DAEs manifests as a reversible photo-initiated ring closing of the central hexatriene moiety. The ring opening and closing reactions of DAEs are accompanied by changes in the electronic structure of the molecules. The open-ring isomer is often optically transparent in the visible spectrum with a large absorption in the UV region. By irradiating the molecule within its UV absorption band, cyclization occurs

producing the closed ring structure. The closed ring structure features a new absorption band in the visible region which can be excited to regenerate the open ring isomer.

Three distinct DAEs are examined in this dissertation, DMPT-PFCP, TPDC, and DTTA which are displayed in figure 1.2. DAEs can be employed in a variety of material applications including optical data storage[12,56] and as light activated ligands in metal-organic frameworks.[54,57,58] The switching quantum yields for DAEs with thiophene aryl-groups are near 100% for the cyclization reaction when the aryl-groups are anti-parallel to each other.[19,59] The anti-parallel orientation is referred to as the reactive conformer, while all others conformations do not readily form stable products and are considered non-reactive. However, in solution, the ratio of reactive and non-reactive conformer is 1:1 for many DAEs, including DMPT-PFCP.[12,60] These non-reactive conformers complicate the spectroscopic study of the cyclization reaction as they evolve on similar picosecond timescales as the reactive conformer.

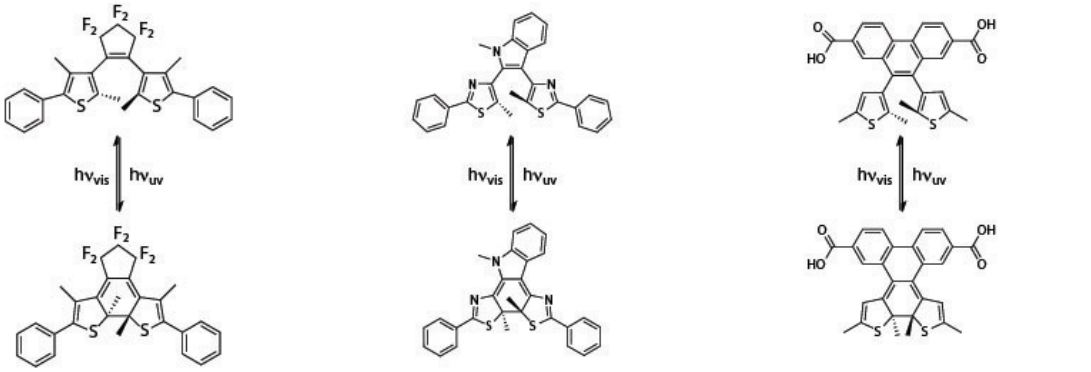

Figure 1.2: Structures of Diarylethene based photoswitches

The cycloreversion reaction of DAEs commonly has quantum yields on the order of 1 to 10%, however Irie and coworkers, as well as previous work by our group, have demonstrated that a second excitation event can increase the cycloreversion reaction yield.[1,2,7,9,10,14,15,61] For DMPT-PFCP the cycloreversion quantum yield is $\sim$1% under one-photon excitation. However, this yield becomes $\sim$7% with appropriately delayed re-excitation.[? ?] Interestingly, this yield enhancement is wavelength dependent, and the role of the higher-lying electronic state is in need of further study

which is begun in this dissertation.

1.3 Dissertation Overview

The following section provides a brief overview of the components of this dissertation.

Chapter 2 describes the experimental equipment and parameters used to perform the R-FSRS experiments. The electronic and optical setup described in this chapter represented new challenges for the research group. This includes generation of the picosecond pump pulse and integration of the charge-coupled device (CCD) array detector. An already existing LabView program was altered to integrate the CCD detector necessary for the R-FSRS measurement. To ensure proper operation of the CCD detector, changes to both the electronic and optical setups were made. These changes are described as well as the necessary data processing procedures for the data files generated by LabView.

Chapter 3 studies the Raman pump wavelength dependence of the DPT excited-state Raman scattering, and the accuracy of calculations (time-dependent density functional theory (TD-DFT) and equation-of-motion coupled cluster with singles and doubles (EOM-CCSD)) in simulating the resonance condition. The excited-state vibrational spectrum and excitation profiles show large enhancements in the C-S bending and stretching modes from the resonant electronic state. It is challenging for calculations to accurately reproduce the excited state absorption which becomes an important limitation of simulating the resonant excite-state Raman spectrum.

Chapter 4 examines the higher-lying excited-states in the cycloreversion of DMPT-PFCP using R-FSRS and via comparison to previous PReP studies. Two distinct excited-state absorption bands are present in the visible region that display wavelength dependence in their dynamic behavior. In this chapter resonance with the higher energy excited-state absorption band is used to generate the excited-state resonance Raman spectrum. The evolution of the cycloreversion reaction is followed via the excited-state Raman active vibrations. Crucially, the decay of the excited-state Raman spectrum and the recovery of the ground-state Raman bleach occur on well-separated timescales. The excited-state vibrational spectrum decays on $\sim$2.4 ps timescale while the excited-state electronic

population decays on a ∼7.2 ps timescale. However, the decay of the excited-state vibrational signature correlates with a barrier crossing on the excited state. This mismatch between the electronic and vibrational timescales points significant change in the resonance condition. Specifically, as the system traverses the excited-state barrier the electronic character of the system changes, resulting in reduced polarizability and Raman scattering intensity for the system.

Chapter 5 studies the wavelength dependence of the cyclization reaction of DMPT-PFCP. The phenylthiophene aryl groups of DMPT-PFCP are the primary chromophores of the molecule, but there is a weakly allowed transition to the LUMO which is localized near the ethene bridge. After excitation two species are present at long time delays, the expected closed-ring product and a triplet species originating from non-reactive conformers Wavelength dependent excitation into higher-lying singlet states shows a change in the relative yield of products, favoring the triplet species as the pump wavelength increases. This trend indicates that the reactive conformer can access an intersystem crossing pathway prior to the complete singlet relaxation and cooling.

Chapter 6 shows the PP spectroscopy and kinetic analysis of DTAA and TPDC photoswitches. As discussed previously for the DMPT-PFCP open-ring isomers, the reactive and non-reactive conformers are present in approximately equal proportions. However, DTAA has weak intramolecular hydrogen bonding between the amine hydrogen and the nitrogen of the thiazole group.[55] This hydrogen bonding provides sufficient stabilization to significantly shift the conformer population in favor of the reactive conformer. The preferential distribution does effectively eliminate spectral contributions from the non-reactive conformer and simplifies the transient spectroscopy. The additional consequence of the change in the structure and conformational distribution is that the molecules are better primed for cyclization. The more favorable ground state geometry results in accelerated kinetics compared to other diarylethene-based photoswitches such as DMPT-PFCP which have completed product formation within one picosecond.

The TPDC molecule is used as a linker in metal-organic frameworks (MOF) made with zinc oxide with the goal of producing active crystalline materials.[54,57,58] To understand the changes in switching behavior with the addition of the phenanthrene dicarboxylic acid both the cyclization

and cycloreversion reaction are studied with PP experiments. The transient absorption of the cyclization reaction displays only minor changes in the first ten picoseconds which are attributed to the vibrational cooling of the excited state. Also, the excited-state spectroscopy indicates that the reaction yield of the UV excitation is extremely low on the timescale of the experiment. It is likely that the excitation localizes on the phenanthrene moiety and the lose of stabilizing energy due to breaking the aromaticity of the phenanthrene structure to form the central cyclohexadiene provides a large barrier to reaction. The cycloreversion reaction grows and shifts over the first few picoseconds before decaying back to baseline. Some residual bleach is observed after the excited-state relaxation, but the magnitude of this feature again points to a low quantum yield for cycloreversion.

Chapter 7 summarizes the work presented in this dissertation and provides some consideration of how this research can be moved forward.

1.4 Bibliography

[1] Miyasaka, H., Murakami, M., Itaya, A., Guillaumont, D., Nakamura, S., and Irie, M. (2001) Multiphoton Gated Photochromic Reaction in a Diarylethene Derivative. *Journal of the American Chemical Society 123*, 753–754.

[2] Ishibashi, Y., Okuno, K., Ota, C., Umesato, T., Katayama, T., Murakami, M., Kobatake, S., Irie, M., and Miyasaka, H. (2010) Multiphoton-Gated Cycloreversion Reactions of Photochromic Diarylethene Derivatives with Low Reaction Yields Upon One-Photon Visible Excitation. *Photochemical and Photobiological Sciences 9*, 172–180.

[3] Ishibashi, Y., Katayama, T., Ota, C., Kobatake, S., Irie, M., Yokoyama, Y., and Miyasaka, H. (2009) Ultrafast Laser Spectroscopic Study on Photochromic Cycloreversion Dynamics in Fulgide Derivatives: One-Photon and Multiphoton-Gated Reactions. *New Journal of Chemistry 33*, 1409–1419.

[4] Mori, K., Ishibashi, Y., Matsuda, H., Ito, S., Nagasawa, Y., Nakagawa, H., Uchida, K., Yokojima, S., Nakamura, S., Irie, M., and Miyasaka, H. (2011) One-Color Reversible Control of Photochromic Reactions in a Diarylethene Derivative: Three-Photon Cyclization and Two-Photon Cycloreversion by a Near-Infrared Femtosecond Laser Pulse at 1.28 mu m. *Journal of the American Chemical Society 133*, 2621–2625.

[5] Houk, A. L., Zheldakov, I. L., Tommey, T. A., and Elles, C. G. (2015) Two-Photon Excitation of trans-Stilbene: Spectroscopy and Dynamics of Electronically Excited States above S-1. *Journal of Physical Chemistry B 119*, 9335–9344.

[6] Larson, E. J., Pyszczynski, S. J., and Johnson, C. K. (2001) Solvent Dependence of Electronic Relaxation in All-Trans Retinal Studied by One- and Two-Photon Induced Transient Absorption. *Journal of Physical Chemistry A 105*, 8136–8144.

[7] Miyasaka, H., Murakami, M., Okada, T., Nagata, Y., Itaya, A., Kobatake, S., and Irie, M.

(2003) Picosecond and Femtosecond Laser Photolysis Studies of a Photochromic Diarylethene Derivative: Multiphoton Gated Reaction. *Chemical Physics Letters 371*, 40–48.

[8] Ishibashi, Y., Murakami, M., Miyasaka, H., Kobatake, S., Irie, M., and Yokoyama, Y. (2007) Laser Multiphoton-Gated Photochromic Reaction of a Fulgide Derivative. *Journal of Physical Chemistry C 111*, 2730–2737.

[9] Ishibashi, Y., Umesato, T., Kobatake, S., Irie, M., and Miyasaka, H. (2012) Femtosecond Laser Photolysis Studies on Temperature Dependence of Cyclization and Cycloreversion Reactions of a Photochromic Diarylethene Derivative. *Journal of Physical Chemistry C 116*, 4862–4869.

[10] Sotome, H., Nagasaka, T., Une, K., Morikawa, S., Katayama, T., Kobatake, S., Irie, M., and Miyasaka, H. (2017) Cycloreversion Reaction of a Diarylethene Derivative at Higher Excited States Attained by Two-Color, Two-Photon Femtosecond Pulsed Excitation. *Journal of the American Chemical Society 139*, 17159–17167.

[11] Asano, Y., Murakami, A., Kobayashi, T., Goldberg, A., Guillaumont, D., Yabushita, S., Irie, M., and Nakamura, S. (2004) Theoretical Study on the Photochromic Cycloreversion Reactions of Dithienylethenes; on the Role of the Conical Intersections. *Journal of the American Chemical Society 126*, 12112–12120.

[12] Irie, M. (2000) Diarylethenes For Memories and Switches. *Chemical Reviews 100*, 1685–1716.

[13] Tani, K., Ishibashi, Y., Miyasaka, H., Kobatake, S., and Irie, M. (2008) Dynamics of Cyclization, Cycloreversion, and Multiphoton-Gated Reaction of a Photochromic Diarylethene Derivative in Crystalline Phase. *Journal of Physical Chemistry C 112*, 11150–11157.

[14] Ward, C. L., Houk, A. L., and Elles, C. G. (2013) Reaction Dynamics of Photochromic Molecular Switches in Their Higher-Excited States: Using Ultrafast Spectroscopy To Study

Molecules Excited Above the S-1 State. *Abstracts of Papers of the American Chemical Society 245*, 1.

[15] Ward, C. L., and Elles, C. G. (2014) Cycloreversion Dynamics of a Photochromic Molecular Switch via One-Photon and Sequential Two-Photon Excitation. *Journal of Physical Chemistry A 118*, 10011–10019.

[16] Kasha, M. (1950) Characterization of Electronic Transitions in Complex Molecules. *Discussions of the Faraday Society* 14–19.

[17] Ishibashi, Y., Umesato, T., Kobatake, S., Irie, M., and Miyasaka, H. (2012) Femtosecond Laser Photolysis Studies on Temperature Dependence of Cyclization and Cycloreversion Reactions of a Photochromic Diarylethene Derivative. *Journal of Physical Chemistry C 116*, 4862–4869.

[18] Ishibashi, Y., Okuno, K., Ota, C., Umesato, T., Katayama, T., Murakami, M., Kobatake, S., Irie, M., and Miyasaka, H. (2010) Multiphoton-Gated Cycloreversion Reactions of Photochromic Diarylethene Derivatives with Low Reaction Yields Upon One-Photon Visible Excitation. *Photochemical and Photobiological Sciences 9*, 172–180.

[19] Nakamura, S., Uchida, K., and Hatakeyama, M. (2013) Potential Energy Surfaces and Quantum Yields for Photochromic Diarylethene Reactions. *Molecules 18*, 5091–5103.

[20] Ward, C. L., and Elles, C. G. (2012) Controlling the Excited-State Reaction Dynamics of a Photochromic Molecular Switch with Sequential Two-Photon Excitation. *Journal of Physical Chemistry Letters 3*, 2995–3000.

[21] Logunov, S. L., Volkov, V. V., Braun, M., and El-Sayed, M. A. (2001) The Relaxation Dynamics of the Excited Electronic States of Retinal in Bacteriorhodopsin by Two-Pump-Probe Femtosecond Studies. *Proc Natl Acad Sci U S A 98*, 8475–9.

[22] McCamant, D. W., Kukura, P., and Mathies, R. A. (2003) Femtosecond Broadband Stimulated Raman: a New Approach For High-Performance Vibrational Spectroscopy. *Appl Spectrosc 57*, 1317–1323.

[23] Dietze, D. R., and Mathies, R. A. (2016) Femtosecond Stimulated Raman Spectroscopy. *Chemphyschem 17*, 1224–1251.

[24] McCamant, D. W., Kukura, P., and Mathies, R. A. (2003) Femtosecond Time-Resolved Stimulated Raman Spectroscopy: Application To the Ultrafast Internal Conversion in Beta-Carotene. *Journal of Physical Chemistry A 107*, 8208–8214.

[25] Kukura, P., McCamant, D. W., and Mathies, R. A. (2007) Femtosecond Stimulated Raman Spectroscopy. *Annual Review of Physical Chemistry 58*, 461–488.

[26] Kukura, P., Yoon, S., and Mathies, R. A. (2006) Femtosecond Stimulated Raman Spectroscopy. *Anal Chem 78*, 5953–5959.

[27] McCamant, D. W., Kukura, P., Yoon, S., and Mathies, R. A. (2004) Femtosecond Broadband Stimulated Raman Spectroscopy: Apparatus and Methods. *Rev Sci Instrum 75*, 4971–4980.

[28] Myers, A. B. (1997) 'Time-Dependent' Resonance Raman Theory. *Journal of Raman Spectroscopy 28*, 389–401.

[29] Ma, H., Liu, J., and Liang, W. (2012) Time-Dependent Approach to Resonance Raman Spectra Including Duschinsky Rotation and Herzberg–Teller Effects: Formalism and Its Realistic Applications. *Journal of Chemical Theory and Computation 8*, 4474–4482.

[30] Albrecht, A. C. (1961) Theory of Raman Intensities. *Journal of Chemical Physics 34*, 1476.

[31] Lee, S. Y., and Heller, E. J. (1979) Time-Dependent Theory of Raman-Scattering. *Journal of Chemical Physics 71*, 4777–4788.

[32] Lee, S. Y., Zhang, D., McCamant, D. W., Kukura, P., and Mathies, R. A. (2004) Theory of Femtosecond Stimulated Raman Spectroscopy. *J Chem Phys 121*, 3632–3642.

[33] Biswas, N., Abraham, B., and Umapathy, S. (2002) Investigation of Short-Time Isomerization Dynamics in p-Nitroazobenzene from Resonance Raman Intensity Analysis. *The Journal of Physical Chemistry A 106*, 9397–9406.

[34] Jarzecki, A. A. (2009) Quantum-Mechanical Calculations of Resonance Raman Intensities: the Weighted-Gradient Approximation. *The Journal of Physical Chemistry A 113*, 2926–2934.

[35] Biswas, N., Abraham, B., and Umapathy, S. (2002) Investigation of Short-Time Isomerization Dynamics in p-Nitroazobenzene from Resonance Raman Intensity Analysis. *The Journal of Physical Chemistry A 106*, 9397–9406.

[36] Myers Kelley, A. (2008) Resonance Raman and Resonance Hyper-Raman Intensities: Structure and Dynamics of Molecular Excited States in Solution. *The Journal of Physical Chemistry A 112*, 11975–11991.

[37] Hong, Z. M., and Asher, S. A. (2015) Dependence of Raman and Resonance Raman Intensities on Sample Self-Absorption. *Applied Spectroscopy 69*, 75–83.

[38] Phillips, D. L., Zgierski, M. Z., and Myers, A. B. (1993) Resonance Raman Excitation Profiles of 1,3-Butadiene in Vapor and Solution Phases. *The Journal of Physical Chemistry 97*, 1800–1809.

[39] Albrecht, A. C. (1961) Theory of Raman Intensities. *Journal of Chemical Physics 34*, 1476.

[40] Myers, A. B., and Pranata, K. S. (1989) Excited-State Geometry and Dynamics of trans-Hexatriene: a Resonance Raman Intensity Study. *The Journal of Physical Chemistry 93*, 5079–5087.

[41] Long, D. A. *The Raman Effect : a Unified Treatment of the Theory of Raman Scattering by Molecules*; Wiley: Chichester ; New York, 2002; pp xxiv, 597 p.

[42] Heller, E. J., Sundberg, R. L., and Tannor, D. (1982) Simple Aspects of Raman-Scattering. *Journal of Physical Chemistry 86*, 1822–1833.

[43] Heller, E. J. (1975) Wavepacket Path Integral Formulation of Semiclassical Dynamics. *Chemical Physics Letters 34*, 321–325.

[44] Heller, E. J. (1981) The Semiclassical Way To Molecular Spectroscopy. *Accounts of Chemical Research 14*, 368–375.

[45] Barclay, M. S., Quincy, T. J., Williams-Young, D. B., Caricato, M., and Elles, C. G. (2017) Accurate Assignments of Excited-State Resonance Raman Spectra: a Benchmark Study Combining Experiment and Theory. *Journal of Physical Chemistry A 121*, 7937–7946.

[46] Facchetti, A. (2011) pi-Conjugated Polymers for Organic Electronics and Photovoltaic Cell Applications. *Chemistry of Materials 23*, 733–758.

[47] Gunes, S., Neugebauer, H., and Sariciftci, N. S. (2007) Conjugated Polymer-Based Organic Solar Cells. *Chemical Reviews 107*, 1324–1338.

[48] Castro, C. M., Delgado, M. C. R., Hernandez, V., Hotta, S., Casado, J., and Navarrete, J. T. L. (2002) Efficiency of the pi Conjugation in a Novel Family of Alpha,Alpha '-Bisphenyl End-Capped Oligothiophenes by Means of Raman Spectroscopy. *Journal of Chemical Physics 116*, 10419–10427.

[49] Chosrovian, H., Rentsch, S., Grebner, D., Dahm, D. U., Birckner, E., and Naarmann, H. (1993) Time-Resolved Fluorescence Studies on Thiophene Oligomers in Solution. *Synthetic Metals 60*, 23–26.

[50] Zheldakov, I. L., Wasylenko, J. M., and Elles, C. G. (2012) Excited-State Dynamics and Efficient Triplet Formation in Phenylthiophene Compounds. *Physical Chemistry Chemical Physics 14*, 6211–6218.

[51] Yu, W. J., Magnanelli, T. J., Zhou, J. W., and Bragg, A. E. (2016) Structural Heterogeneity in the Localized Excited States of Poly(3-hexylthiophene). *Journal of Physical Chemistry B 120*, 5093–5102.

[52] Zhou, J. W., Yu, W. J., and Bragg, A. E. (2015) Structural Relaxation of Photoexcited Quaterthiophenes Probed with Vibrational Specificity. *Journal of Physical Chemistry Letters 6*, 3496–3502.

[53] Irie, M., and Mohri, M. (1988) Thermally Irreversible Photochromic Systems - Reversible Photocyclization of Diarylethene Derivatives. *Journal of Organic Chemistry 53*, 803–808.

[54] Patel, D. G., Walton, I. M., Cox, J. M., Gleason, C. J., Butzer, D. R., and Benedict, J. B. (2014) Photoresponsive Porous Materials: the Design and Synthesis of Photochromic Diarylethene-Based Linkers and a Metal-Organic Framework. *Chemical Communications 50*, 2653–2656.

[55] Fukumoto, S., Nakashima, T., and Kawai, T. (2011) Intramolecular Hydrogen Bonding in a Triangular Dithiazolyl-Azaindole for Efficient Photoreactivity in Polar and Nonpolar Solvents. *European Journal of Organic Chemistry* 5047–5053.

[56] Irie, M., Fukaminato, T., Matsuda, K., and Kobatake, S. (2014) Photochromism of Diarylethene Molecules and Crystals: Memories, Switches, and Actuators. *Chem Rev 114*, 12174–277.

[57] Cox, J. M., Walton, I. M., Patel, D. G., Xu, M. Y., Chen, Y. S., and Benedict, J. B. (2015) The Temperature Dependent Photoswitching of a Classic Diarylethene Monitored by in Situ X-ray Diffraction. *Journal of Physical Chemistry A 119*, 884–888.

[58] Walton, I. M., Cox, J. M., Coppin, J. A., Linderman, C. M., Patel, D. G., and Benedict, J. B. (2013) Photo-Responsive MOFs: Light-Induced Switching of Porous Single Crystals Containing a Photochromic Diarylethene. *Chemical Communications 49*, 8012–8014.

[59] Nakamura, S., Uchida, K., and Hatakeyama, M. (2013) Potential Energy Surfaces and Quantum Yields for Photochromic Diarylethene Reactions. *Molecules 18*, 5091–5103.

[60] Matsuda, K., and Irie, M. (2004) Diarylethene As a Photo Switching Unit. *Journal of Photochemistry and Photobiology C-Photochemistry Reviews 5*, 169–182.

[61] Ward, C. L., and Elles, C. G. (2012) Controlling the Excited-State Reaction Dynamics of a Photochromic Molecular Switch with Sequential Two-Photon Excitation. *Journal of Physical Chemistry Letters 3*, 2995–3000.

Chapter 2

Experimental Methods

2.1 Overview

The reaction dynamics and kinetics were probed using two- and three-beam vibrational and electronic spectroscopic techniques. The electronic spectroscopy techniques are pump-probe(PP) and pump-repump-probe(PReP) spectroscopy. The vibrational techniques are spontaneous and stimulated Raman spectroscopy for measurments of the electronic ground-state, and resonant femtosecond stimulated Raman spectroscopy (R-FSRS) to study the electronic excited-state. Except for ground state Raman spectroscopies, all of the techniques used in this dissertation take advantage of femtosecond laser pulses to collect time-resolved vibrational or electronic spectra of photochemical reactions. Transient absorption (TA) spectra collected using PP are used to inform both the PReP and R-FSRS measurements. For both R-FSRS and PReP techniques a second excitation pulse is used to measure the impact of higher-lying electronic states on the transient species. In the case of PReP, the second excitation promotes molecules to a higher-lying electronic state whose effect is then probed. For R-FSRS, the second laser pulse is a ps pulse which is the Raman pump which induces the time-dependent resonant Raman scattering of the excited-state. This chapter provides a brief background of the PP experimental setup then describes the implementation, methods, and data analysis procedures for R-FSRS.

2.2 Transient Absorption Techniques

The spectroscopic experiments are performed using a Ti:sapphire oscillator (Coherent, Mantis)and amplifier (Coherent, Legend Elite) which produces 35 fs laser pulses at a 1kHz repetition rate. The tunable pump pulses are generated using either a home-built optical parametric amplifier (OPA)[1,2]or a commercial OPA with two optional frequency conversion stages. Detection is performed using a white light continuum (WLC) that is produced by focusing a small fraction of the laser fundamental into a circularly rotating calcium fluoride window.[3,4]

An initial pump pulse populates the electronic excited state of the molecules while a broadband continuum probe measures excited state absorption with a controlled time delay. The excited state absorption spectrum is calculated using alternating measurements of the broadband probe intensity with (I_{ON}) and without (I_{OFF}) the pump pulse incident on the sample. A synchronized optical chopper (Newfocus, 3501) is used to block every other pump pulse and allow shot-to-shot measurements of the white light intensity. These intensities are employed to calculate the change in absorbance, $\Delta A(t)$.

$$\Delta A(t) = -log_{10}\frac{I_{ON}}{I_{OFF}} \tag{2.1}$$

For the PP measurements a 1/8 meter imaging spectrograph disperses the WLC probe using a reflective grating for broadband detection using either a photodiode array or charge-coupled device detector records the intensity. The photodiode array (PDA) (Hamamatsu, S3901-256Q) has 256 pixels and uses a 300 line/mm grating in the spectrograph to simultaneously detect an approximately 300 nm range in the UV to visible spectrum. The grating is manufactured with a 300 nm blaze angle and corresponds to optimal of wavelengths between 200-750 nm. With a 120 μm entrance slit approximately 7.5 nm resolution is achieved over a spectral range of 350-650 nm. Further detail regarding this setup can be found in the dissertation of Cassandra Ward.[2] A synchronized data acquisition (DAQ) card collects the PDA pixel voltages for every laser pulse. A second synchronized DAQ card collects the phase of the optical chopper. The optical chopper outputs a TTL signal to indicate the phase of the chopping wheel. The chopper output wave is used

to automatically determine I_{ON} and I_{OFF} intensities on the PDA for equation 2.1 above. The PDA detector is use only for PP and PReP experiments due to the limited resolution caused by the large pixels and limited sensitivity of the pixels.

The linear charge coupled device (CCD) (Hamamatsu, S11156-2048) with 2068 pixels along with the companion driver circuit (Hamamatsu,C11165-01), can also mount on the 1/8 meter spectrograph which provides comparable spectral range when used with a 600 line/mm grating. The different grating is only required due to the longer length of the CCD array (one inch) relative to the PDA (0.5 inch). This grating has a blaze angle corresponding to 450 nm and usable spectral range from 300-900 nm. With the same 120 μm entrance slit the resolution of the detector is roughly 3.7 nm, however, due to the higher sensitivity of the CCD array a 50 μm entrance slit may be used while maintaining sufficient intensity on the array elements. In this case, the spectrograph has a resolution of 1.5 nm. Again, this setup is limited to PP and PReP experiments as the resolution is still insufficient for vibrational spectroscopic experiments.

Unlike the PDA, the CCD counts are transferred via USB to the PC instead of through the DAQ cards. An additional gating circuit was added to maintain synchronization between the chopper and the LabView software. This is discussed in more detail in section 2.3.3.

2.3 Resonance Femtosecond Stimulated Raman Spectroscopy (R-FSRS)

Resonant femtosecond stimulated Raman spectroscopy is a three laser pulse experiment requiring high resolution and sensitivity compared to the PP and PReP electronic spectroscopies.[5–8] The actinic laser pulse is a femtosecond pulse which initially excites molecules with a wavelength tuned to the ground state absorption of the sample. A picosecond Raman pump pulse with bandwidth $<$30 cm^{-1} is then used to generated the Raman scattering signal. The Raman pump is tuned to the excited-state absorption of the sample to take advantage of the resonance enhancement for the excited-state Raman scattering. The third laser pulse, the WLC, is temporally overlapped with the Raman pump pulse to stimulate the Raman scattering. Due to the finite duration of the Raman pump, the relative delay between the Raman pump and WLC will impact the resolution and quality

of the excited-state Raman spectrum. For further details see references 9 and 10.

To achieve the necessary experimental conditions for R-FSRS experiments, new optics and electronics were required. Key among those optics was a means to generate picosecond narrow bandwidth pulses out of the amplified femtosecond pulses generated by the Ti:sapphire laser system. The stimulated Raman process requires the overlap of the picosecond Raman pump pulse with the WLC probe. The addition of a delay controlled femtosecond actinic pump pulse to excite the sample prior to the arrival of the Raman pump and probe, allows for the collection of the excited-state Raman spectra. However, by blocking the actinic pump, ground-state stimulated Raman spectra may be collected using the same custom LabView software.

The following sections outline the experimental setup, both optical and electronic, developed in order to run R-FSRS measurements. In addition, the data analysis techniques that have been automated via Igor Pro procedures are described.

2.3.1 Picosecond Raman Pump Generation

Because the stimulated Raman scattering signal is the Fourier transform of the vibrational coherence convoluted with the temporal profile of the Raman pump pulse (in the case of a transform-limited pulse) the Raman pump pulse must have a full-width at half-maximum (FWHM) that is greater than the vibrational decoherence lifetime to eliminate artifacts from the Raman spectrum. As with all frequency domain measurements, the bandwidth of the picosecond pulse places an inherent limit on the resolution of the Raman spectra. Even with a Raman pump with infinitely narrow bandwidth, the vibrational peaks have natural linewidths determined by the dephasing lifetime for the vibration and the Fourier relationship between lifetime and bandwidth. A Raman pump with a bandwidth greater than the natural linewidth of a vibration will cause broadening of the vibrational peak and the vibrational linewidth will have a lower limit set by the Raman pump bandwidth.[11] To address the complications in both the time and frequency domain, the fs pulses pass through a birefringent beta-barium borate (BBO) crystal to produces the second harmonic of the incident laser frequency. The second harmonic output at the Raman pump wavelength has both

reduced the pulse bandwidth and lengthened temporal profile compared with the incident fundamental. The bandwidth is reduced by taking advantage of the narrow phase-matching bandwidth caused by the long crystal pathlength to promote temporal walk-off of within the bandwidth of the laser pulse and stretch the femtosecond pulse to >0.5 ps. Figure 2.1 shows the bandwidth of the spectrally compressed second harmonic and, for reference the laser fundamental.

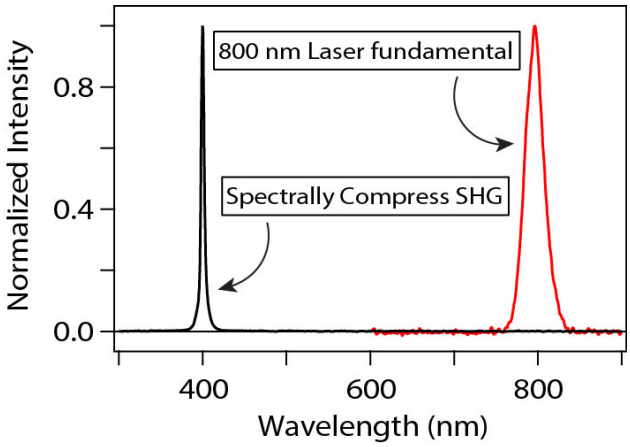

Figure 2.1: The spectrally compressed second harmonic output spectrum and the Ti:sapphire laser fundamental spectrum. The second harmonic spectrum is limited by the instrumental resolution of the spectrograph at 3.7 nm.

The temporal walk-off is a frequency dependent property of the group-delay-mismatch. Consequently, the magnitude of spectral compression is dependent on the difference in index of refraction for the incident and SHG pulses. Therefore, the effectiveness of the spectral compression in the Raman pump pulse decreases as the frequency of the Raman pump decreases.[12,13] Specifically, this means the picosecond pulse generated near the UV will stretch more in time than pulses generated in the red region of the visible spectrum. This effective spectral compression of the second harmonic pulse can be calculated using the following equation[9]:

$$FWHM_{SH} = \frac{0.886}{L(\frac{1}{v_F} - \frac{1}{v_{SH}})} \tag{2.2}$$

where $FWHM_{SH}$ is the approximate frequency bandwidth of the SH pulse, L is the length of the crystal, and v_F and v_{SH} are the group velocities of the fundamental and second harmonic wavelengths, respectively. Because the group velocity mismatch (denominator of equation 2.2)

decreases at longer wavelengths, the Raman pump generation wavelengths above 520 nm does not have sufficiently narrow bandwidth to act as a Raman pump.[9] For more detailed theory see 9 and 10.

For Raman pump wavelengths other than the second harmonic of the Ti:sapphire laser source, tunability is provided by a home built OPA or a commercial OPA (TOPAS) and adjusting the phase matching angle of the BBO crystal. Currently, we have two type 1 BBO crystals for picosecond pulse generation. Both have physical dimensions of 6x6x25 mm but differ in the angle of the optical axis of the crystal relative the exposed incident crystal face. The first crystal has an angle of 27.6 degrees which corresponds to generating SH of 800 nm light at normal incidence. Due to the length of the crystal, the phase-matching tunability is limited by the aperture of the optic. Accounting for the changing beam path through the crystal using Snell's law, the effective aperture limits the picosecond pulse generation from 350 to 520 nm. The second BBO crystal is cut with the optical axis 21.1 degrees from normal incidence. The tunable range of this crystal is 500 to 650 nm.

The profile for the spectrally compressed pulse is asymmetric. As the incident beam propagates through the BBO crystal, the SH lags behind the incident beam causing a temporal profile that gradually increases to the maximum followed by a relatively steep dropoff. Distinctive spectral ringing is observed in the Raman spectrum when the pulse is not sufficiently long in time or the stimulating probe is too close to the peak of the pulse.[14] However, a spectral filter which slighly narrows the spectrally compressed pulse further stretches the pulse and produces a Gaussian temporal profile.

2.3.2 Spectral filter

Due to the limited range in which the BBO spectral compression provides a sufficiently stretched pulse, an additional spectral filter may be added to efficiently extend the usable range of spectral compression into the near-IR.[10] By taking advantage of the the Fourier relationship between time and frequency domains of ultrafast laser pulses, by dispersing a femtosecond pulse with a grating and using a slit to block the majority of the pulse bandwidth, a picosecond pulse with a narrow

bandwidth can be generated. Unfortunately, using a spectral filter has a relative efficiency of $\leq$ 1% using a femtosecond pulse in order to reduce the bandwidth to generate an effective Raman pump.[15] However, when using an already spectrally compressed pulse from the second harmonic process described above, only a small attenuation of the spectral edges of the pulse is needed to produce an effectively Gaussian pulse in time with sufficiently narrow bandwidth to function as a Raman pump.[10]

The approach used for this work employs a double pass 4F spectral filter that is diagrammed in figure 2.2. The picosecond pulse is reflected off a 1200 line/mm grating at a very slight downward angle, and the first order diffracted light is steered through a cylindrical lens with a focal length of 200 mm. Instead of having the slit at the focal position between the gratings and lenses, a mirror is placed in this position with the adjustable slit as close as possible to the mirror face. The spectrally filtered light is then passed back through the lens (represented by the gray outline), off the grating and is directed down the table with a pick-off mirror. Due to the optics involved proper alignment of the spectral filter is crucial to producing a recollimated beam to focus on the sample.

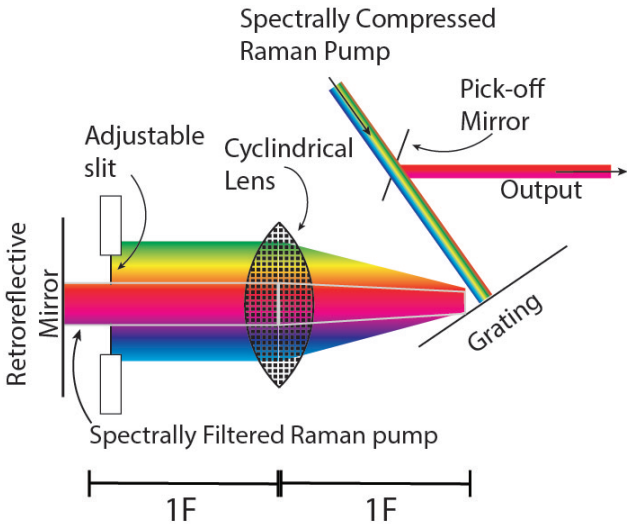

Figure 2.2: The spectrally compressed intput is directed into the spectral filter as indicated by the black arrow. The beam is dispersed by the grating and columnated by a cylindrical lens. The beam is then passed through the adjustable slit to spectrally narrow the pulse. After the slit the dispersed beam is passed back through the lens and grating to re-columnate the pulse, which is represented by the gray outlines.

For best control, both the cylindrical lens and the mirror are mounted on micrometer stages.

The adjustable slit is also mounted on the stage with the retroreflecting mirror. Consistent placement of the beam on the same point of the grating is vital to minimize constant adjustments to the micrometer positions. As changing the point of incidence on the grating changes the path length to the lens and between the lens and the mirror, without adjusting the placement of both optics the picosecond beam will not be collimated. With the focal axis of the cylindrical lens matching the dispersion of the grating and adjustable slit, the alignment of the back reflection from the mirror through the lens should be just below the forward propagating beam before the slit is put in place. The slit placement should be adjusted by maximizing the pulse energy as a function of slit position while stepwise closing the slit down to approximately 20 μm.

If there is any concern regarding the alignment of the cylindrical lens, it is best to verify its orientation after the slit placement has been optimized. With a narrow opening in the slit, the power transmission through the spectral filter should drop very quickly as the cylindrical lens is rotated, but should be observable after the pick-off mirror. Additionally, asymmetric diffraction fringes may be observable to the left and right of the beam when the slit is *not* centered on the beam. The slit should be moved to minimize this effect.

2.3.3 CCD Detector

2.3.3.1 Labview integration for PP and FSRS experimentation

Former lab member Cassandra Ward created and validated LabVIEW software which used the trigger signal generated by the commercial laser and voltage signals from optical choppers to collect pulse sequences for pump-probe and pump-repump-probe experiments. The program written for PReP experimental data collection was used as a starting point to integrate the CCD detector and automate the Raman gain data collection. Significant changes were made to the signal processing VIs to generate the appropriate spectra. The excited-state spectra observed in LabVIEW are

presented as the δgain which is defined as:

$$\delta Gain = (\frac{I_{RamanON}}{I_{RamanOFF}})_{ActinicON} - (\frac{I_{RamanON}}{I_{RamanOFF}})_{ActinicOFF} \tag{2.3}$$

Additionally, the data recording VIs save only the raw counts, after dark count correction, and spectra that are generated in the 'Live View' portion of the program are reconstructed by functions written in Igor Pro which load the data for processing. The Hamamatsu linear CCD array and the driver circuit are integrated into the LabVIEW code using the manufacturer provided VIs which communicate via USB connection with the PC. The driver circuit uses BNC connections for the trigger input and readout is performed via USB.

2.3.3.2 Array Synchronization

The integration of the Hamamatsu linear CCD array and driver unit is complicated by an asynchronous delay between the laser trigger and the initiation of data collection. The typical delay for the CCD array versus a single photo-diode ranged from 15 to 22 ms as seen in figure 2.3. The delay corresponds to a delay between the LabView initiation of data collection and the start of data collection due to the initialization of the CCD. Due to the multiple pulse combinations of the three beam experiments, it is critical to start data collection at a known position in the pulse sequence.

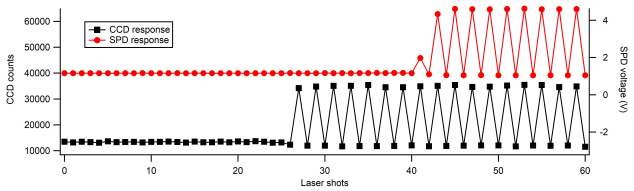

Figure 2.3: The red and black markers show the response of the CCD and PDA to the same laser pulse sequence. The alternating response is due to the chopper positioned before the beam splitter used to ensure the same pulses are being detected. A single software trigger initiates both detectors. The earlier detection of signal in the CCD indicates an inconsistent start time for data collection relative to the PDA.

An additional timing circuit is introduced to control the CCD initialization to account for the delay. The timing diagram for this circuit is presented as figure 2.4. Once Labview has initialized

the array, the counts for 100 laser shots are collected continuously beginning as soon as the CCD is initialized. The rise of the trigger signal initiates the CCD integration and readout, however, to maintain a consistent pulse sequence, the trigger is only passed to the detector circuit once the timing circuit receives three high signals. The first signal is the laser trigger generated at the amplifier as pulses are ejected. Second, is the chopper 2 TTL which is synchronized with the laser trigger via Chopper 1 and ensures that the first pulse collected corresponds to both pump beam choppers in the high position. The use of chopper 2 also ensures that the first laser pulse collected corresponds to when both choppers signals are high. The third is a digital trigger generated via LabVIEW which remains on for 100 ms. However, this digital trigger is delayed by 30 ms to allow the CCD driver unit to fully initialize and begin the collection of the next 100 laser pulses using the laser trigger passed to the CCD.

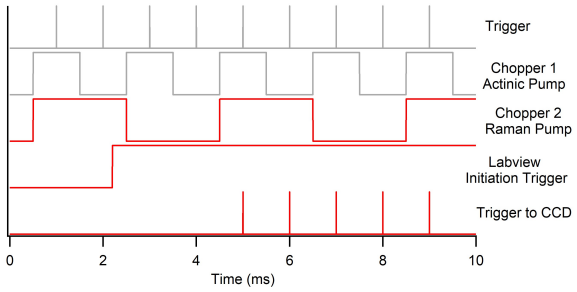

Figure 2.4: The timing diagram used to synchronized the CCD detection and pulse sequence. Chopper 2 is run in series with chopper 1, so only the signal from chopper 2 is needed for synchronous operation. The trigger is only passed to the CCD after both the rising edge of the LabView initiation trigger and chopper 2 signals are detected.

2.3.3.3 Frequency shifting

The signal-to-noise ratio in the CCD detector is sufficient using a simple dark counts correction for transient electronic absorption spectroscopy and most transient Raman spectroscopy, however, for higher sensitivity measurements an additional technique is added to decrease the noise further. The most significant contribution to noise in the linear CCD detector is non-uniform response between pixels that is intensity dependent.[16] The impact of the non-uniform response is made worse by extremely short integration windows. CCD detectors generate charge via photoelectric conversion

which is passed to a storage gate before being binned for readout. However, the transfer rate between the bin and storage gate is on the order of tens of microseconds and dependent on the number of charge carriers.[17] As such, and integration window of 200 μs should be the minimum setting.

Commonly, the ground-state stimulated Raman spectrum of the sample, including the solvent Raman signal, is subtracted from the excited state transient Raman spectrum which minimizes the non-uniform pixel response. However, when the probe pulse is significantly attenuated by excited-state absorption, the non-uniform pixel response will produce fixed-pattern 'noise' in the baseline. Over small spectral regions, the pixel-to-pixel variability is effectively wavelength independent. Therefore, by adjusting the grating angle in the imaging spectrograph the spectral range that is incident on the detector shifts. This shifting is demonstrated in panel (A) of figure 2.5. The experimentally relevant signals will shift with the spectral window while residual fixed pattern noise remains relatively constant.[18] By averaging the spectroscopic signals over a number of pixels, the effect of the variable pixel sensitivity is reduced. Importantly, spectral frequency shifting can reduce the standard deviation of the noise by a factor of three by maintaining the same laser shot averaging and introducing 10 frequency shifts into the averaged data.[18–20]

While frequency shifting can introduce significant time savings, the current manual shifting of the spectrograph grating requires each grating position to be saved individually and combine in post-processing. Automated procedures have been written in Igor Pro to combine frequency shifted data. To combine the data sets with different spectral ranges, a uniform spectral calibration is generated using the approximate pixel width of the individually calibrated spectra from each of the datasets. Each Raman data set is then interpolated to the new array, and all data sets are averaged (see figure 2.5). This procedure is also performed for time-evolving data sets assuming all time delays are matching between spectrally shifted data.

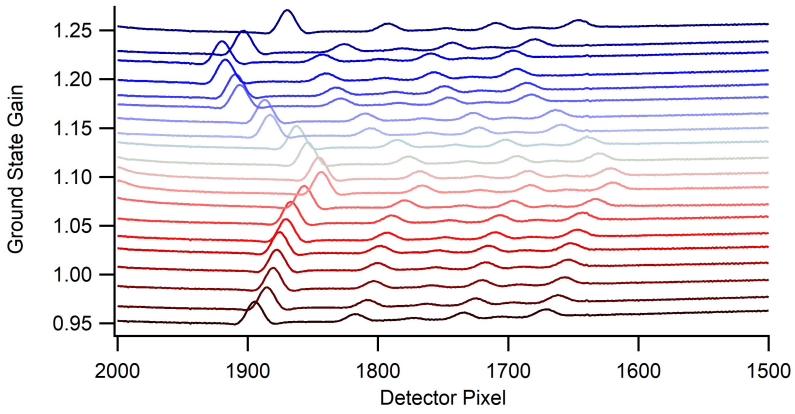

(a)

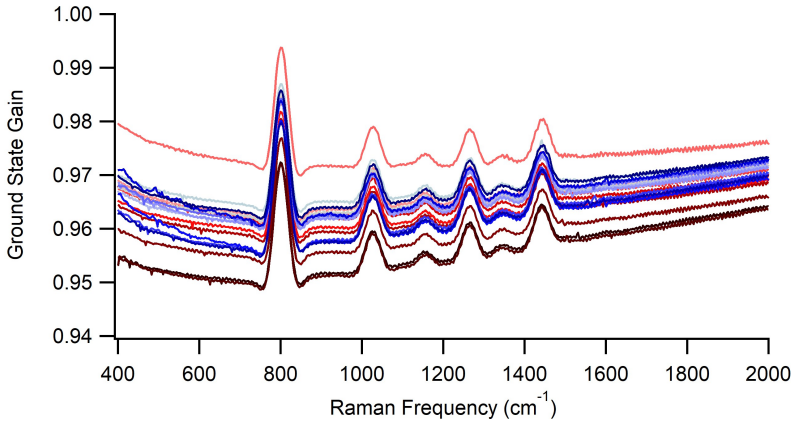

(b)

Figure 2.5: A number of spectra are shown vertically offset in panel (A). Each spectrum has been shifted slightly on the detector so that the Raman frequency shifts correlate with different pixels. Calibration of each spectrum produces the result shown in panel (B) which can then be interpolated and averaged to reduce systematic variation.

2.3.4 Data Analysis

2.3.4.1 Solvent Calibration

Solvent bands are used as an internal standard to calibrate the Raman frequency shifts for the SRS and FSRS measurements.[7] Due to the high concentration of the solvent relative to the solute or excited state species, the solvent Raman spectrum is used to assign the Raman shifts appropriately. Since the SRS spectrum is collected as part of the FSRS measurement, the ground state spectrum is a convenient source of intense and well known Raman peaks. The most commonly used solvent for this work is cyclohexane which has six Raman active peaks between 800 and 1500 cm^{-1} that

allow for this calibration. In experiments with Raman pump attenuation in the sample, two of the Raman peaks can be lost in the fixed pattern noise of the CCD detector. However, the four remaining peaks are sufficient to provide an accurate calibration

The Raman pump wavelength is used along with the literature values for the selected cyclohexane frequencies to determine the wavelength, in nanometers, for the solvent bands to generate the calibrated spectrum. The conversion to nm simplifies the calibration due to the grating dispersion used in the imaging spectrograph, which is linear in nm but reciprocal in frequency. The pixel positions of the solvent bands are then used to fit Gaussian functions to the data and quantitatively extract the Raman peak positions. The Gaussian determined peak positions are then combined with the peak wavelengths to perform a linear regression. The regression results are then used to produce the new calibrated spectrum in nm. The cailbrated spectrum is then converted from nanometers to wavenumbers for use with all associated data.

2.3.4.2 Baseline Correction

In the R-FSRS spectrum, the Raman pump generates a transient vibrational spectrum, however due to the resonance condition, the vibrational spectrum is convoluted with an excited-state absorption.[21] In effect, this electronic absorption depletes the WLC and produces a broad baseline deviation in the desired vibrational spectrum. This can be observed in both the ground- and excite-state as demonstrated in panels (A) and (C) of figure 2.6. A procedure has been written to automate this process. However, for spectra in which the excited-state absorption has narrow features on the order of $\sim$100 cm^{-1}, manual correction may be required. To account for this deviation, a polynomial is fit to the baseline of the spectrum.

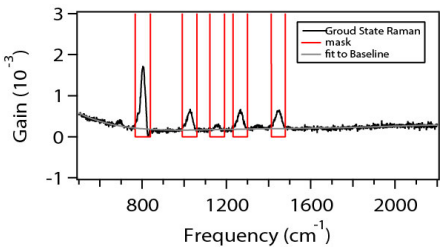

(a)

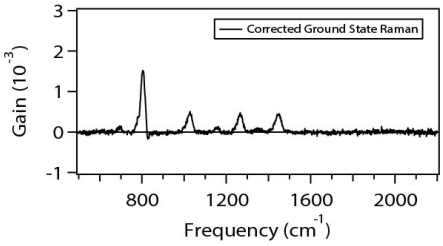

(b)

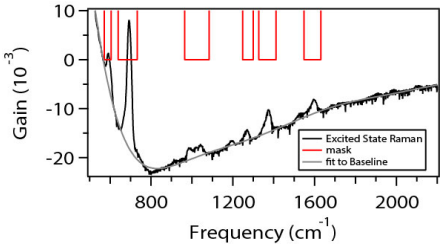

(c)

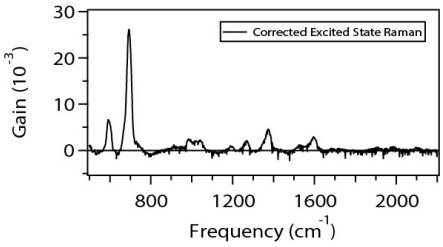

(d)

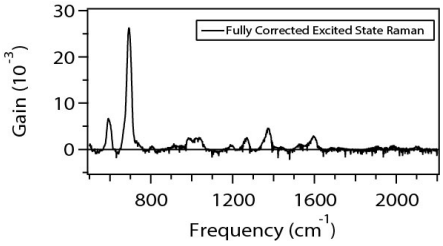

(e)

Figure 2.6: Panel (A) shows the calculated Gain (red) for the ground-state Raman spectrum as well as the mask (grey) used to prevent fitting to the solvent peaks. The corrected spectrum is shown in panel (B). Panels (C)and (D) present the similar spectra for the excited-state. The negative peaks in panel (D) are due to over subtraction of the solvent bands. The over subtraction is corrected by adding the ground-state spectrum in panel (B) scaled to the depletion, resulting in the spectrum in panel (E)

In order to increase the quality of the fit, a spectral mask is used to omit fitting with strong vibrational features, such as the solvent peaks. The mask is based on the solvent band peak positions and sets a masking window of two times the spectral resolution by default. The polynomial fit is subtracted from the corresponding FSRS spectrum. An example of the new baseline corrected spectra are presented in panels (B) and (D) of figure 2.6. Due to the time dependence of the electronic excited-state absorption, new fits are performed at each time delay of the FSRS experiment.

2.3.4.3 Solvent Subtraction Correction

Due to the depletion of the Raman pump pulse by the excited-state absorption, the magnitude of the ground state Raman scattering is larger when the actinic pump is blocked.[21] In reference equation 2.3, this means the 'Actinic OFF' term over corrects the solvent Raman scattering To correct the discrepancy in the solvent subtraction, a percentage of the ground state spectrum is added back into the excited state spectrum. This functionality is also incorporated into the automatic baseline correction procedure written for Igor Pro. The specific amount of correction required is time-dependent and proportional to the magnitude of the excited state absorption at the Raman pump wavelength. Additionally, the focal conditions at the sample can cause small changes in the index of refraction of the sample.[22] These changes are important because they can cause small observed shifts in solvent bands of the excited-state relative to the ground-state and complicate the solvent band correction. This effect is often observed in the 801 cm^{-1} solvent band of cyclohexane and is demonstrated panel (E) of figure 2.6 Without properly addressing the spectral shift, artifacts are introduced into the excited state spectrum when the percentage of ground state signal is added.

This effect is more significant in Raman bands with narrower linewidths that are, therefore, more sensitive to the small spectral shift. To prevent these artifacts, shifting of the ground state spectrum must be performed before addition into the excited state signal. A simplified approach is to shift the spectrum at each time point by a number of pixels that best produces a flat baseline.

2.4 Sample Preparation

Experiments presented in this document are performed exclusively in the solution phase and primarily using cyclohexane as the solvent. Other solvents were used in cases of low solubility of the analyte in cyclohexane and will be highlighted as they are introduced. The selection of cyclohexane as the primary solvent is due to its weakly interacting nature with the conjugated organic analytes, minimizing spectroscopically observable solvent effects and simplifying comparison with gas phase calculations.

For transient absorption measurements, solutions were typically made to generate an absorption at the wavelength of the pump between 0.1 and 0.4 OD in a 1.0 mm cuvette. This absorbtivity corresponds to concentrations between 0.1 and 5.0 millimolar for most species. To produce transient absorption with appropriate signal levels between 2 and 50 mOD, the pump beam power and focal conditions at the sample can be adjusted to increase or decrease the excited state populations being probed and prevent saturation effects. PReP experiments are conducted under similar conditions to the PP experiments. However, more substantial excited state absorption is desirable for PReP measurements. In multi-ring, highly conjugated organic molecules, absorption of 0.5 at the ground state pump wavelengths is typically sufficient to generate a measurable excited state population.

For measurement of transient Raman spectra, determining the concentrations becomes much more complicated due to the dependence on two electronic transitions as well as the shape and relative delay of the picosecond Raman pump pulse. A complete understanding of the TA is invaluable in preparing transient Raman samples for all but the most basic systems. The reasonable starting point for optimizing sample concentration starts using a solution with approximately 0.8 OD absorption in the flow cell at the wavelength of the actinic pump. For molecules with appreciable Raman cross-sections this is often a sufficient concentration to observe the SRS of the ground state, even in off-resonance or pre-resonance conditions. Assuming the spectral region where the Raman scatter appears has contributions from only the transient absorption signal, a roughly 20% depletion of the WLC should provide sufficient excited state population with enough transition

probability to the higher lying resonant state to produce transient Raman spectra. From this point, the transient Raman signals can be further optimized by adjusting the pump intensities and focal conditions. In the case of a spectral region that has contributions from multiple processes (e.g., stimulated emission, ground state bleach, etc.) a systematic approach to sample dilution may be needed to achieve optimal sample concentration.

2.5 Bibliography

[1] Cerullo, G., and De Silvestri, S. (2003) Ultrafast Optical Parametric Amplifiers. *Review of Scientific Instruments 74*, 1–18.

[2] Ward, C. Controlling the Cycloreversion Reaction of a Diarylethene Derivative Using Sequential Two-Photon Excitation. 2014.

[3] Brodeur, A., and Chin, S. L. (1999) Ultrafast White-Light Continuum Generation and Self-Focusing in Transparent Condensed Media. *J. Opt. Soc. Am. B 16*, 637–650.

[4] Nagura, C., Suda, A., Kawano, H., Obara, M., and Midorikawa, K. (2002) Generation and Characterization of Ultrafast White-Light Continuum in Condensed Media. *Appl. Opt. 41*, 3735–3742.

[5] Kukura, P., McCamant, D. W., and Mathies, R. A. (2007) Femtosecond Stimulated Raman Spectroscopy. *Annu Rev Phys Chem 58*, 461–488.

[6] Kukura, P., Yoon, S., and Mathies, R. A. (2006) Femtosecond Stimulated Raman Spectroscopy. *Anal Chem 78*, 5953–5959.

[7] McCamant, D. W., Kukura, P., Yoon, S., and Mathies, R. A. (2004) Femtosecond Broadband Stimulated Raman Spectroscopy: Apparatus and Methods. *Rev Sci Instrum 75*, 4971–4980.

[8] Lee, S. Y., Zhang, D., McCamant, D. W., Kukura, P., and Mathies, R. A. (2004) Theory of Femtosecond Stimulated Raman Spectroscopy. *J Chem Phys 121*, 3632–3642.

[9] Pontecorvo, E., Kapetanaki, S. M., Badioli, M., Brida, D., Marangoni, M., Cerullo, G., and Scopigno, T. (2011) Femtosecond Stimulated Raman Spectrometer in the 320-520nm Range. *Optics Express 19*, 1107–1112.

[10] Pontecorvo, E., Ferrante, C., Elles, C. G., and Scopigno, T. (2013) Spectrally Tailored Narrowband Pulses For Femtosecond Stimulated Raman Spectroscopy in the Range 330-750 Nm. *Optics Express 21*, 6866–6872.

[11] Long, D. A. *The Raman Effect : a Unified Treatment of the Theory of Raman Scattering by Molecules*; Wiley: Chichester ; New York, 2002; pp xxiv, 597 p.

[12] Marangoni, M., Brida, D., Conforti, M., Capobianco, A. D., Manzoni, C., Baronio, F., Nalesso, G. F., De Angelis, C., Ramponi, R., and Cerullo, G. (2009) Synthesis of Picosecond Pulses by Spectral Compression and Shaping of Femtosecond Pulses in Engineered Quadratic Nonlinear Media. *Opt Lett 34*, 241–243.

[13] Marangoni, M. A., Brida, D., Quintavalle, M., Cirmi, G., Pigozzo, F. M., Manzoni, C., Baronio, F., Capobianco, A. D., and Cerullo, G. (2007) Narrow-Bandwidth Picosecond Pulses by Spectral Compression of Femtosecond Pulses in Second-Order Nonlinear Crystals. *Opt Express 15*, 8884–8891.

[14] Yoon, S., McCamant, D. W., Kukura, P., Mathies, R. A., Zhang, D., and Lee, S. Y. (2005) Dependence of Line Shapes in Femtosecond Broadband Stimulated Raman Spectroscopy on Pump-Probe Time Delay. *J Chem Phys 122*, 024505.

[15] McCamant, D. W., Kukura, P., and Mathies, R. A. (2003) Femtosecond Broadband Stimulated Raman: a New Approach For High-Performance Vibrational Spectroscopy. *Appl Spectrosc 57*, 1317–1323.

[16] Gilliland, R., xa,, L,, Goudfrooij, P., Kimble, R., xa,, and A, (1999) Linearity and High Signal to Noise Performance of the STIS CCD. *Publications of the Astronomical Society of the Pacific 111*, 1009–1020.

[17] Teranishi, N., Kohno, A., Ishihara, Y., Oda, E., and Arai, K. (1984) An Interline CCD Image Sensor with Reduced Image Lag. *IEEE Transactions on Electron Devices 31*, 1829–1833.

[18] Challa, J. R., Du, Y., and McCamant, D. W. (2012) Femtosecond Stimulated Raman Spectroscopy Using a Scanning Multichannel Technique. *Applied Spectroscopy 66*, 227–232.

[19] Knoll, P., Singer, R., and Kiefer, W. (1990) Improving Spectroscopic Techniques by a Scanning Multichannel Method. *Applied Spectroscopy 44*, 776–782.

[20] Deckert, V., and Kiefer, W. (1992) Scanning Multichannel Technique For Improved Spectrochemical Measurements with a CCD Camera and Its Application To Raman-Spectroscopy. *Applied Spectroscopy 46*, 322–328.

[21] Hong, Z. M., and Asher, S. A. (2015) Dependence of Raman and Resonance Raman Intensities on Sample Self-Absorption. *Applied Spectroscopy 69*, 75–83.

[22] Righini, R. (1993) Ultrafast Optical Kerr Effect in Liquids and Solids. *Science 262*, 1386–1390.

Chapter 3

Probing Higher-Lying Electronic States with Mode-Specific Excited-State Resonance Raman Spectroscopy

3.1 Introduction

Femtosecond stimulated Raman scattering (FSRS) is a time-resolved technique for probing the structural dynamics of molecules in electronically excited states.[1–3] Vibrational frequency shifts reveal changes in molecular structure and bonding as a molecule evolves along an excited-state potential energy surface. By measuring the time evolution with vibrational resolution, the technique provides more detailed structural information about the excited-state dynamics than is usually available from transient electronic absorption measurements alone.[4] Similar to ground-state Raman spectroscopy, the observed vibrational frequencies of an FSRS spectrum reflect the structure of the molecule in the prevailing electronic state, and therefore report on the dynamics of low-lying excited states, typically S_1. Transient Raman measurements often take advantage of a tunable Raman excitation wavelength to target specific electronic resonances. Matching a specific resonance in the transient electronic absorption spectrum allows one to selectively probe a specific intermediate or product species due to enhanced Raman scattering.[1,4–12] While the resonance condition serves the important purpose of increasing the Raman signal in transient measurements, both for species selectivity and simply to improve signal-to-noise, its influence on the mode-dependent Raman intensities has been largely ignored.[13]

The resonance condition has long been recognized in ground-state Raman spectroscopy as a way to probe the Franck-Condon region of an electronically excited state.[14,15] The vibrational

frequencies still report on the ground electronic state, but mode-dependent enhancements of the vibrational intensities reflect the relative displacement of the upper potential energy surface along each of the ground-state vibrational coordinates. Therefore, tuning the Raman excitation wavelength into resonance with a specific electronic transition reveals detailed information about the upper state through the excitation-wavelength dependent Raman gain profiles of the different vibrational modes.[16] Modes with the largest displacement in the upper state give the largest relative Raman scattering enhancements, thus reporting on the initial dynamics of the molecule moving out of the Franck-Condon region of the upper state. Such detailed information about the upper electronic state has not been explored in FSRS measurements, where the focus of most experiments remains on the time-evolving dynamics of the lower state.

Considering the upper electronic state in FSRS measurements is important in two contexts. On the one hand, the relative intensities in the transient Raman spectrum depend on the identity of the resonant electronic state. We previously showed for a series of thiophene derivatives that the calculated off-resonance Raman activities do not adequately represent the experimental intensities, and that the correct assignment of FSRS bands requires careful consideration of the resonance condition.[13] Neglecting mode-specific resonance enhancement effects can result in erroneous assignments that could affect the interpretation of the transient dynamics. On the other hand, resonance-enhanced FSRS measurements also provide novel information about the higher-lying potential energy surface, analogous to ground-state resonance Raman spectroscopy.

Information about the upper state in the transient Raman measurement reports on the dynamics of a molecule upon sequential excitation with two photons. Sequential excitation opens the possibility of selectively controlling a photochemical reaction by redirecting molecules along a secondary reaction path. The dynamics of a molecule following excitation with a single photon is determined by the potential energy surfaces of the molecule, but re-excitation with a second, time-delayed photon allows the molecule to access new regions of the higher-lying potential energy surfaces that are not accessible from the equilibrium ground-state geometry. For example, we showed that sequential two-photon excitation with a carefully timed secondary excitation laser

pulse selectively increases the cycloreversion yield of a photochromic molecular switch by exploiting higher-lying electronic states that carry the molecule more efficiently along the reaction coordinate.[17,18] The larger quantum yield represents a change in the final outcome of the reaction following sequential excitation, but resonance-enhanced FSRS measurements have the potential to directly probe the ultrafast dynamics immediately after excitation to the upper state.

In this chapter, we examine mode-specific resonance enhancements in the excited-state Raman spectrum of a non-reactive model compound, 2,2'-diphenylthiophene (DPT), in order to show that it is feasible to extract information about the upper potential energy surface from FSRS measurements. Specifically, we measure the excitation-wavelength dependence of the excited-state resonance Raman spectrum of DPT in the relaxed (*i.e.* thermally equilibrated) S_1 state. The excitation-wavelength dependence of the excited-state Raman spectrum reveals strong enhancement of several vibrational modes related to the secondary excitation of the conjugated π electronic structure. We compare the experimental results with calculated excited-state Raman spectra for resonant and off-resonant excitation from the relaxed S_1 state. The resonant calculations consider both the S_1-S_n electronic transition strengths and the relative displacements of the upper (S_n) potential energy surfaces in order to simulate resonance Raman spectra for each of the higher-lying states. The experimental results provide a stringent test of the computational approach, and indicate important limitations based on the level of theory and basis set, whereas the calculated spectra facilitate the interpretation of the experimental spectra. This work provides a foundation for making better assignments of resonance-enhanced excited-state Raman spectra, as well as extracting novel information about higher-lying excited states from FSRS measurements.

3.2 Theory

We briefly summarize key results from Raman scattering theory, including the time-dependent formalism for resonance Raman, in order to illustrate our approach to calculating resonance-enhanced FSRS spectra. More detailed theoretical descriptions of resonance Raman scattering are available in the literature.[15,16,19–25] In general, the intensity of Raman scattering is proportional to the square

of the transition polarizability tensor, α_{fi}. The polarizability term for a transition from initial vibronic state $|i\rangle$ to final state $|f\rangle$ can be represented in a sum-over-states approach,

$$\alpha_{fi} = \frac{1}{\hbar}\sum_{n}\left(\frac{\langle f|\,\hat{\mu}\,|n\rangle\,\langle n|\,\hat{\mu}\,|i\rangle}{\omega_{ni}-\omega_{p}-i\Gamma_{n}}+\frac{\langle f|\,\hat{\mu}\,|n\rangle\,\langle n|\,\hat{\mu}\,|i\rangle}{\omega_{fn}+\omega_{p}+i\Gamma_{n}}\right) \tag{3.1}$$

where $|n\rangle$ are all possible intermediate states, $\hat{\mu}$ is the electric dipole operator, ω_{ni} and ω_{fn} are the transition frequencies, and ω_p is the frequency of the Raman excitation field. States $|i\rangle$, $|f\rangle$, and $|n\rangle$ are vibronic states, and Γ_n are phenomenological broadening terms related to the dephasing time of each intermediate state. The Raman activity increases significantly for resonant or near-resonant electronic excitation due to the decreasing value in the denominator of the first term as ω_p approaches ω_{ni}. The second term in the equation only applies far from resonance, and is negligible under the conditions described here.[22] Equation 3.1 is the A term from the Albrecht description of Raman scattering, which is the dominant contribution to the Raman scattering signal in the absence of Herzberg-Teller coupling in the upper electronic states.[19,26]

The equation simplifies for a resonance condition involving only a single upper electronic state, in which case the summation includes only the vibrational levels $|v_n\rangle$ of that state. We only consider Raman scattering for initial and final vibrational levels $|v_i\rangle$ and $|v_f\rangle$ within the same electronic state; therefore the two electronic transition dipole moments are equal ($\mu_{ni} = \mu_{nf}$), and factor out of the summation. The resulting description of the polarizability term depends on the transition strength between the two electronic states ($|\mu_{ni}|^2$) and the product of Franck-Condon overlap terms for each pair of vibronic transitions.

$$\alpha_{fi} \approx \frac{|\mu_{ni}|^2}{\hbar}\sum_{v_n}\frac{\langle v_f|v_n\rangle\,\langle v_n|v_i\rangle}{\omega_{v_n v_i}-\omega_{p}-i\Gamma_{v_n}} \tag{3.2}$$

The vibrational overlap terms are responsible for the mode-dependent enhancements in a resonance Raman spectrum. Strong transitions require intermediate states that have good Franck-Condon overlap with both the initial and final vibrational levels of the ground electronic state. This condition is most easily satisfied when the equilibrium geometry of the upper electronic state is displaced

relative to the lower state, due to the orthogonality of the ground-state vibrational wave functions. In other words, vibrational coordinates that have a different equilibrium displacement in the upper electronic state generally have larger overlap with both $|\nu_i\rangle$ and $|\nu_f\rangle$, and therefore have the strongest intensities in the resonance Raman spectrum. Based on symmetry considerations, only vibrations from totally symmetric or degenerate irreducible representations have non-zero contributions to the resonance Raman spectrum in the absence of Herzberg-Teller coupling.[20]

The time-dependent formalism for resonance Raman scattering[20,27] provides an intuitive picture to relate the geometry change in an upper state with the mode-dependent resonance Raman intensities. Very briefly, after converting frequencies to energies ($E_{\nu_i} = \hbar\omega_{\nu_i}$, etc.) and replacing the denominator with a formally equivalent half Fourier transform,[20]

$$\frac{1}{(E_{\nu_n} - E_{\nu_i} - E_p - i\hbar\Gamma_{\nu_n})} = \frac{i}{\hbar}\int_0^\infty e^{-i(E_{\nu_n} - E_{\nu_i} - E_p - i\hbar\Gamma_{\nu_n})t/\hbar} dt \tag{3.3}$$

equation 3.2 can be recast in terms of a time-dependent wave packet that propagates on the upper electronic state, $|\nu_i(t)\rangle = e^{-i\hat{H}_n t/\hbar}|\nu_i\rangle$.[22] The resulting expression for the polarizability term is essentially the time-integrated Franck-Condon overlap between the wavepacket $|\nu_i(t)\rangle$ and the vibrational wavefunction of the final state, $|\nu_f\rangle$.[15,20,23]

$$\alpha_{fi} \approx \frac{i}{\hbar}|\mu_{ni}|^2 \int_0^\infty \langle\nu_f|\nu_i(t)\rangle\, e^{i(E_{\nu_i} + E_p)t/\hbar - \Gamma_n t} dt \tag{3.4}$$

Thus, the intermediate states in the Raman scattering process are replaced by the time-dependent wave packet, which represents the propagation of the initial (ground-state) vibrational wavefunction on the potential energy surface of the upper electronic state. As before, the damping term $e^{-\Gamma_n t}$ accounts for dephasing.

The expression further simplifies by using a Gaussian function to approximate the $t = 0$ wavepacket along each vibrational coordinate q_k, which then evolves in time according to Newton's equation, $F_{q_k} = -\frac{\partial V_n}{\partial q_k}$. The subscript n indicates that the motion follows the potential of the upper state, whereas the vibrational coordinates q_k are the normal modes of the lower electronic state. This

description of the time-dependent overlap integral using classical dynamics gives the transition polarizability for each vibration k,[20,27]

$$\alpha_{fi}^{k} \approx -\frac{i}{\hbar}\frac{|\mu_{ni}|^2}{(2\omega_k)^{1/2}}\left(\frac{\partial V_n}{\partial q_k}\right)\int_0^\infty e^{i(E_{\nu_i}+E_p-E_n)t/\hbar-\Gamma_n t}e^{-\left(\frac{\partial V_n}{\partial q_k}\right)^2 t^2/4\omega_k}t\,dt \tag{3.5}$$

where ω_k is the frequency of normal mode k in the lower electronic state, E_n is the vertical electronic transition energy, and the integral is the excitation profile as a function of Raman excitation energy E_p. Finally, the intensity for a resonance Raman transition to the fundamental vibration of mode k is proportional to the square of the polarizability term,

$$I_k \propto E_p E_s^3 |\alpha_{fi}^{k}|^2 \approx E_p E_s^3 \frac{|\mu_{ni}|^4}{2\omega_k}\left(\frac{\partial V_n}{\partial q_k}\right)^2 \tag{3.6}$$

for incident and scattered photon energies E_p and E_s, respectively.

Equation 3.6 introduces the crucial concept that the polarizability, and therefore the Raman intensity of a given mode k, depends on the slope of the resonant (upper) electronic state along that vibrational coordinate. This result provides a foundation for calculating excited-state resonance Raman spectra based on the electronic transition strength, $|\mu_{ni}|^2$, and the gradients of the upper-state potential, $\partial V_n/\partial q_k$. The frequencies are determined by the normal modes of the lower electronic state, while the relative intensities depend on the slope of the upper-state potential energy surface along each of those vibrational coordinates. For the excited-state resonance Raman spectra shown below, $|\nu_i\rangle$ represents the ground vibrational level of the first electronically excited state S_1, and the resonant states $|\nu_n\rangle$ are the vibrational levels of a single higher-lying electronic state S_n. The experimental Raman excitation wavelengths are resonant with a single excited-state absorption band, and are sufficiently far from the stimulated emission band to exclude any contributions from resonance with the ground electronic state. While the gradient approximation makes several important assumptions, this approach provides a valuable starting point for comparison with the experimental resonance-enhanced FSRS spectra.

3.3 Methods

3.3.1 Experimental Details

Our transient absorption and transient stimulated Raman measurements use the modified output of an amplified Ti:Sapphire laser (Coherent, Legend Elite HP) that produces 35 fs pulses at 1 kHz repetition rate. A portion of the amplifier output pumps a commercial optical parametric amplifier (OPA) with two additional stages of non-linear frequency conversion to generate actinic pulses at 310 nm ($\sim$75 fs and $\sim$0.9 μJ at the sample). A home-built double-pass OPA provides tunable near-IR pulses that pass through a 25 mm long BBO crystal (θ_{cut} = 21.1°) for second harmonic generation (SHG) at the Raman pump wavelength. Group velocity mismatch in the long BBO crystal gives spectrally narrow SHG output with nearly ps pulse duration.[28] The second harmonic pulses then pass through a $4f$ spectral filter to further narrow the bandwidth and eliminate asymmetry in the temporal profile.[29] The resulting Raman pump pulses are tunable over a range of 500-620 nm, with <20 cm^{-1} bandwidth, $\sim$1 ps duration, and >0.50 μJ per pulse. We generate fs probe pulses by focusing a small portion of the laser fundamental into a circularly translating CaF_2 window to produce white-light continuum. A 750 nm short-pass filter eliminates residual fundamental and a neutral density filter attenuates the probe to match the dynamic range of the detector. All laser pulses have vertical polarization in the lab frame and intersect at a small angle in a flow cell with 1 mm thick CaF_2 windows and 0.5 mm path length.

After the sample, a 1/8 m imaging spectrograph disperses the probe light onto either a 256-pixel photodiode array (Hamamatsu, S3901-256Q) for transient absorption or a 2068 pixel linear CCD array (Hamamatsu, S11156-2048) for transient Raman measurements. We use a 300 line/mm grating in the spectrograph for transient absorption, or 1800 line/mm grating for transient Raman measurements. In both cases, we measure the transmitted probe intensity at 1 kHz while the actinic pump is chopped at 500 Hz and the Raman pump, when present, is chopped at 250 Hz for active background subtraction. The CCD array has a slightly nonlinear response that varies across the range of pixels and introduces artificial variations in the signal from pixel to pixel.[30] We

compensate the slightly nonuniform response by calibrating the response of each pixel individually, as well as measuring and averaging Raman spectra at five different positions of the spectrograph grating. We shift the frequency range on the CCD array by $\sim$20 cm^{-1} between each measurement, calibrate each spectrum using the frequencies of the cyclohexane solvent bands, and then take the average to obtain the final spectrum. The frequency-shifting approach is similar to previous methods for reducing noise in FSRS measurements.[31,32] We collect 3×10^5 laser shots for each of the individual spectra, resulting in final spectra that are averaged over 1.5×10^6 shots to give a standard deviation of $<10^{-4}$ in the Raman gain signal.

The sample consists of a 1.0 mM solution of 2,5-diphenylthiophene (TCI America) in cyclohexane (spectroscopic grade, Fisher). Irradiating the sample with $\sim$0.8 μJ actinic pump pulses gives a maximum transient absorption of approximately 200 mOD at 560 nm. We measure the ground-state Raman spectrum of DPT (15 mM in cyclohexane) using a commercial Raman spectrometer (StellarNet) with 785 nm CW pump laser and 4 cm^{-1} resolution.

3.3.2 Computational Details

We use a development version of the GAUSSIAN software package[33] for all calculations, except where indicated. First, we calculate off-resonant Raman spectra for both the ground and first excited electronic states using time-dependent density functional theory (TD-DFT) with B3LYP/aug-cc-pVDZ.[13] We obtain the mode-dependent Raman activities by numerical differentiation of the polarizability tensor along each of the normal mode coordinates at the optimized geometry of each state.[25] Our excited-state calculations use analytical polarizabilities for S_1 that are available in the development version of GAUSSIAN.[13,33] Using this method, we previously compared the calculated off-resonance excited-state Raman intensities with experimental resonance-enhanced FSRS spectra for a series of eight aryl-substituted thiophene derivatives, including DPT.[13] Our earlier work shows good agreement between the calculated and experimental frequencies, even though the resonance condition significantly alters the intensities of the experimental spectra.

In order to account for the resonance condition explicitly, we simulate the excited-state Raman

spectrum of DPT based on the time-dependent formalism described above. In short, we calculate the $S_n \leftarrow S_1$ transition moments and the gradients of the S_n potential energy surfaces at the S_1 optimized geometry for states up to $n = 20$. For the resonance Raman calculations, we use both TD-DFT and equation of motion coupled cluster with single and double excitations (EOM-CCSD) to obtain the excited states.[34] We obtain the TD-DFT electronic transition moments from the double residues of the quadratic response functions using the Dalton software package,[35–38] and calculate EOM-CCSD transition moments using the unrelaxed transition density approximation.[39] The TD-DFT calculations are more efficient, but the EOM-CCSD calculations should provide a more accurate representation of the excited states. Due to the computational cost of the EOM-CCSD calculations, we are only able to obtain gradients for a few vibrational modes. Additional details are provided below.

3.4 Results

3.4.1 Excited-State Dynamics

Figure 3.1 shows the evolution of the transient electronic absorption spectrum of DPT following excitation at 310 nm. At early delay times, the transient spectrum has a strong excited-state absorption band centered near 565 nm, and a weaker stimulated emission band near 390 nm. The intensity of the excited-state absorption band oscillates slightly within the first few ps due to quantum beating (not shown), then narrows slightly on a $\sim$15 ps time scale due to structural relaxation and vibrational cooling in the S_1 excited state. Integrating the singlet absorption band at 1 ps after excitation gives an experimental oscillator strength of $\sim$0.3 for the S_n-S_1 transition. Both the excited-state absorption and stimulated emission bands decay with a single exponential time constant of 270 $\pm$ 7 ps due to intersystem crossing (ISC) to a long-lived triplet state. A weaker triplet-triplet absorption band near 430 nm appears on the same timescale as the decay of S_1, similar to previous measurements of two- and three-ring aryl-substituted thiophene derivatives in solution.[13,40–43]

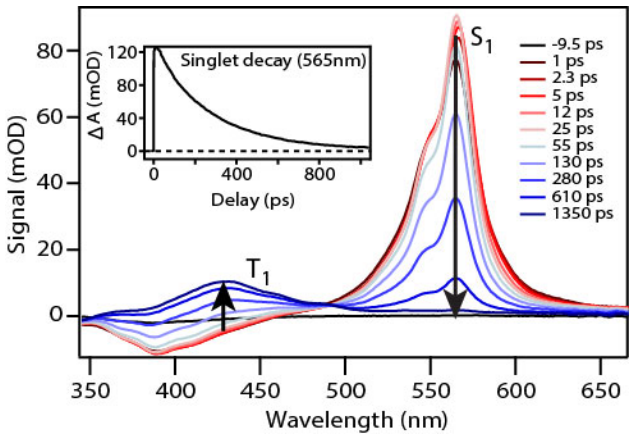

Figure 3.1: Evolution of the transient electronic absorption spectrum of DPT following 310 nm excitation. The inset shows the decay of the S_1 absorption band with a time constant of 270 $\pm$ 7 ps.

Transient stimulated Raman (FSRS) measurements track the structural dynamics of DPT in more detail by following the evolution of the excited-state vibrational spectrum. Here, we measure the FSRS spectrum of DPT following actinic excitation at 310 nm and variable Raman excitation wavelength. The transient FSRS spectra in Figure 3.2 were measured with a Raman excitation wavelength of 620 nm, which is on the low-energy tail of the S_1 excited-state absorption band. All of the FSRS bands decay to the baseline on a similar timescale as the ISC observed in the transient electronic absorption spectrum, and therefore are assigned as S_1 vibrations.[13] We do not readily observe triplet bands because the Raman pump wavelength is off-resonant of the T_1 absorption band.

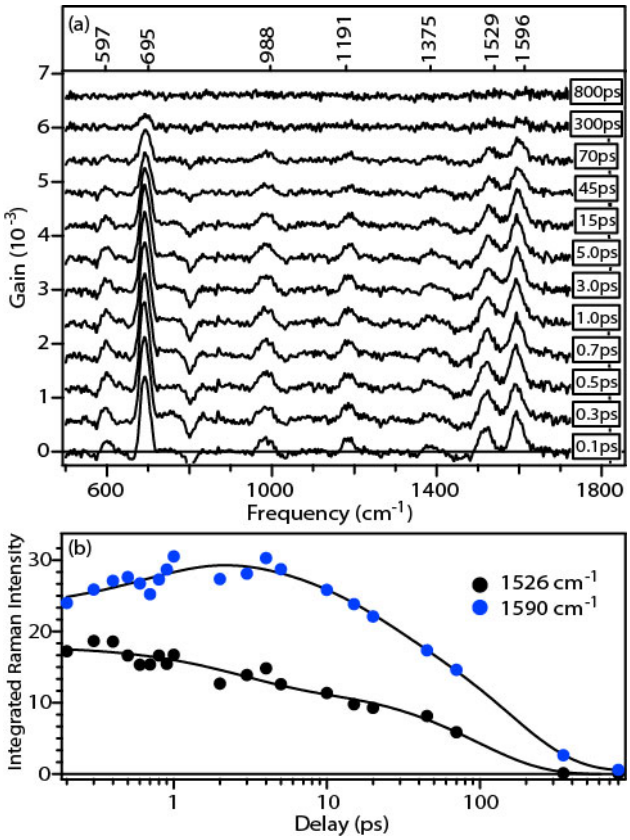

Figure 3.2: Evolution of the FSRS spectrum of DPT following excitation at 310 nm. The Raman pump wavelength is 620 nm. The negative signal at 800 cm^{-1} is an artifact from subtraction of the solvent signal. Panel (b) shows the integrated intensities of the 1529 and 1596 cm^{-1} bands as a function of time. The solid lines are fits to the data with a sum of two exponentials with time constants of 1.6 and 83 ps.

The most dominant features in the transient Raman spectrum include a pair of delocalized ring deformation modes in the 600-700 cm^{-1} range, phenyl and thiophene distortion modes near 988 and 1191 cm^{-1}, and a pair of ethylenic stretching modes in the 1500-1600 cm^{-1} region that are characteristic of π-conjugated molecules.[13] The assignments are discussed in more detail below. Notably, the relative intensities of the 1529 and 1596 cm^{-1} vibrations change within the first few ps following excitation, as highlighted in the lower panel of Figure 3.2. Bragg and coworkers[44] recently showed that the relative intensities of the analogous in-phase and out-of-phase ethylenic stretching modes of quaterthiophene track the evolution of the molecule to a more planar structure in the excited state. Similarly, a change in the relative intensities of the two modes in DPT indicates rapid planarization on a timescale of 0.8 ± 0.2 ps, due to the quinoidal character of the $\pi\pi^*$ excited

state. We note that there is a slight increase in the intensity of the transient electronic absorption signal on this timescale as well, although the transient electronic spectrum does not provide the same level of insight about the structural evolution of the molecule that is available from the Raman measurement.

3.4.2 Excited-State Resonance Raman

While the evolution of the FSRS spectrum reveals information about the structural dynamics on S_1, the primary focus of this chapter is using the mode-specific resonance Raman enhancements to probe the higher-lying excited states, S_n. In order to separate the effects of the time-evolving wavepacket on S_1, we measure the wavelength-dependent transient Raman spectrum of DPT at a fixed delay of 30 ps following the initial excitation. This delay allows the molecule to relax to the geometry of the excited-state minimum and dissipate excess vibrational energy to the solvent. In other words, the 30 ps delay allows us to probe DPT at the minimum of the S_1 potential energy surface, and therefore simplifies the comparison of the experimental and computational spectra.

Before making a direct comparison between experiment and theory for the excited-state Raman spectrum, we first compare the experimental and computational Raman spectra for the ground state of DPT in Figure 3.3. The ground-state calculation provides a reference for the best level of agreement that can be expected for a given computational method and basis set, because both the experimental and computational spectra are off-resonant for the ground state of DPT. One complication in simulating the ground-state spectrum of DPT is the conformational flexibility due to rotation of the phenyl rings. DPT has a non-planar optimized ground-state geometry, with roughly 20° dihedral angle between the central thiophene and each of the phenyl rings. The relative orientation of the two phenyl rings results in two nearly iso-energetic structures with C_S and C_2 symmetry, separated by a torsional barrier below k_BT at room temperature. Even the fully planar (C_{2v}) structure is accessible at room temperature. Figure 3.3 shows the calculated Raman spectrum of the lower-energy C_2 species; however, the spectra for the C_S and C_{2v} structures are nearly identical.

The calculated ground-state frequencies (B3LYP/aug-cc-pVDZ) are within $\sim$20 cm^{-1} of the

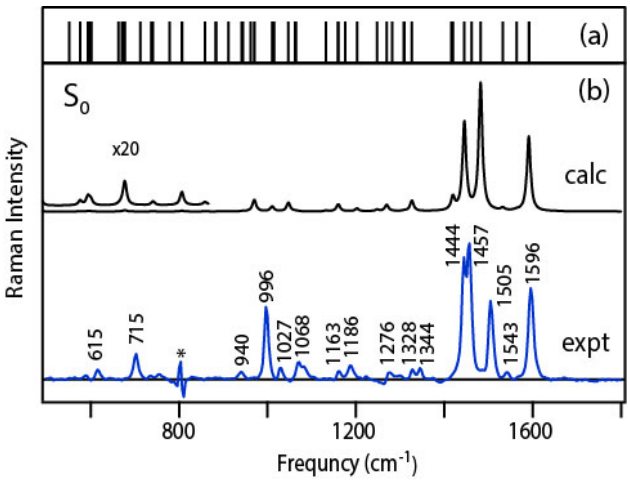

Figure 3.3: Calculated (B3LYP/aug-cc-pVDZ) and experimental ground-state Raman spectra of DPT. The calculated spectrum includes 10 cm^{-1} Lorentzian broadening, and is also shown on an expanded scale below 900 cm^{-1} to emphasize the low intensity bands in this region. The experimental spontaneous Raman spectrum is measured using a 785 nm excitation laser. For reference, the top panel (a) shows all of the calculated vibrational frequencies after applying an empirical frequency scaling factor of 0.970.[45]

experimental values. The calculated intensities are also in reasonably good agreement with the experimental spectrum, although the calculations underestimate the relative intensities of some of the lower frequency bands by up to an order of magnitude. This systematic underestimation of the low-frequency modes is consistent with our previous results across a series of aryl-substituted thiophenes.[13] The most notable discrepancy for DPT is the phenyl ring breathing mode near 996 cm^{-1}, which is stronger than predicted by theory, as is also apparent in earlier work by Castro *et al.*[40] We are currently exploring the reason for this systematic underestimation of the low-frequency intensities, and early indications suggest that including anharmonic effects accounts for some, but not all of the discrepancy. Nevertheless, the calculated off-resonance Raman spectrum provides a good representation of the experimental ground-state spectrum of DPT.

In contrast with the ground-state, the calculated off-resonance Raman spectrum for the excited state of DPT does not adequately reproduce the experimental FSRS spectrum, as shown in Figure 3.4. The figure compares the experimental FSRS spectrum at 600 nm Raman pump wavelength with the calculated off-resonance Raman spectrum at the optimized S_1 geometry.[13] Although the 600 nm Raman pump wavelength is only on the tail of the excited-state absorption band, we ob-

serve mode-specific resonance enhancement effects compared with the off-resonance calculation. Most notably, the low-frequency mode near 695 cm^{-1} is the strongest band in the experimental spectrum, even though the off-resonance calculation predicts relatively weak scattering at low frequencies. The discrepancy is much more significant than in the ground-state spectrum. Furthermore, the off-resonance calculations predict the wrong relative intensities of the two phenyl deformation modes (ν_{18} and ν_{25}), and also of the two ethylenic stretching modes (ν_{67} and ν_{69}). The mode-specific enhancements are even more pronounced when the Raman excitation wavelength approaches the maximum of the excited-state absorption band (see below), which is a clear sign of resonance-enhancement.

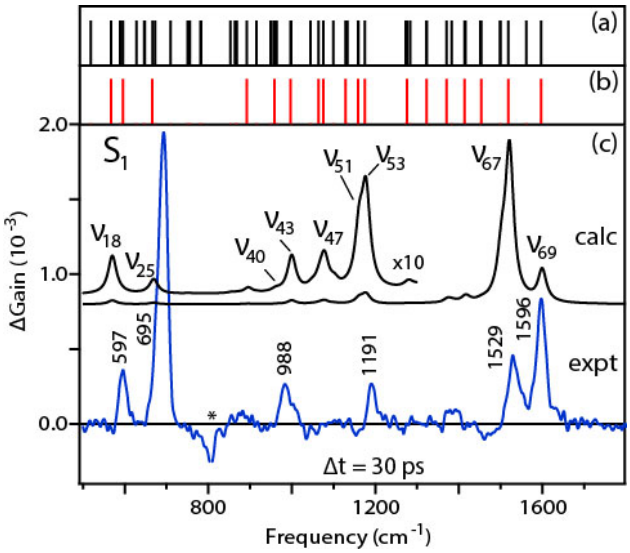

Figure 3.4: Calculated (B3LYP/aug-cc-pVDZ) and experimental excited-state Raman spectra of DPT. The calculated off-resonance spectrum includes 25 cm^{-1} Lorentzian broadening, and is also shown on an expanded scale below 1300 cm^{-1} to emphasize the low intensity bands in this region. The experimental FSRS spectrum is measured at a time delay of 30 ps using 600 nm Raman excitation wavelength, and the asterisk indicates an artifact from subtraction of the solvent background. For reference, the top two panels show (a) all of the calculated vibrational frequencies, and (b) only the totally symmetric vibrations. The calculated frequencies include an empirical scaling factor of 0.970.[45]

Even though the calculated off-resonance spectrum does not accurately reproduce the experimental intensities due to mode-specific enhancements, the calculated frequencies provide a foundation for assigning vibrations in the excited-state Raman spectrum.[13] The top panel of Figure 3.4 shows the full set of calculated vibrational frequencies for the optimized S_1 excited state using

B3LYP/aug-cc-pVDZ.[13] The optimized structure is planar, with C_{2v} symmetry. In the absence of Herzberg-Teller coupling, only totally symmetric (and degenerate) vibrations are symmetry-allowed in resonance Raman,[22] therefore the second panel shows only the subset of a_1-symmetry modes for the DPT excited state. This narrower collection of states provides the basis for our assignment of the experimental spectrum. For example, the experimental bands at 1529 and 1596 cm^{-1} are relatively easy to assign as delocalized ethylenic stretching modes ν_{67} and ν_{69}, respectively, because these are the only two totally symmetric modes in this frequency range. The delocalized character of the two vibrations and the strong coupling with the conjugated π backbone of the molecule explain the strong intensities in both the on- and off-resonant spectra.

We assign other experimental bands in comparison with the calculated frequencies, but also considering which motions are likely to be enhanced by the resonance condition.[13] The S_1 excited-state absorption band represents excitation of π electrons, therefore we anticipate the largest enhancements for modes that are sensitive to changes of the π bonding framework, as these modes should have the largest displacement between S_1 and the upper electronic state. For example, we assign the most intense Raman band at 695 cm^{-1} as ν_{25}, which is a totally symmetric vibration that includes symmetric phenyl ring distortion and thiophene C-S-C stretching motions. This delocalized mode has large displacement along the π-conjugated framework of DPT, consistent with a strong resonance enhancement under π-excitation. Similarly, the 597 cm^{-1} vibration is assigned as ν_{18}, a delocalized phenyl ring distortion and thiophene C-S-C bending mode that is also sensitive to π excitation.

Although the above assignments are supported by the appearance of the corresponding bands in the calculated off-resonance spectrum, we reiterate that assignments should not be made based on intensity alone. We previously showed that the calculated off-resonance intensities can be deceiving if the resonance enhancement effects are not carefully considered.[13] This cautionary point is highlighted by our assignment of the experimental band of DPT at 988 cm^{-1} as ν_{40}, rather than ν_{43}. Based on intensity alone, it would be tempting to assign the experimental FSRS band as the more intense ν_{43} from the calculated spectrum, but the primarily C-H bending motion

associated with that mode is not expected to have the same degree of resonance enhancement as the in-plane C-C-C bending and ring deformation of ν_{40}. Instead, the shoulder of the 988 cm^{-1} mode at roughly 1025 cm^{-1} in Figure 3.4 is tentatively assigned as C-H bending and weak phenyl ring distortion associated with ν_{43}. Similarly, the experimental band at 1191 cm^{-1} could be assigned as either ν_{51} or ν_{53} based on calculated frequencies and intensities alone, but we assign this band as ν_{53} based on the more delocalized C=C and C-S stretching character of the latter, which is likely to have stronger resonance enhancement. Table 1 shows the experimental and calculated vibrational frequencies and assignments for several transitions. All of these modes have strong resonance enhancement related to the distortion of the molecular structure upon secondary excitation of π electrons from the S_1 state of DPT. The assignments are further supported by calculated resonance enhancements that we discuss below.

Table 3.1: Assignment of Experimental Excited-State Raman Bands

Vibration	Calc. Frequency (cm^{-1})[a]	Exp. Frequency (cm^{-1})	Relative Gain[b]	Motion
ν_{18}	569	597	29.5	C-S-C bend and phenyl def.
ν_{25}	669	695	13.5	C-S-C sym. stretch and phenyl def.
ν_{40}	962	988	15.9	C-C-C bend/phenyl distortion
ν_{43}	1000	1025	–	C-H bend and phenyl distortion
$\nu_{10} + \nu_{25}$	–	1048	–	–
ν_{51}	1163	–	–	C-H bend
ν_{53}	1178	1191	6.4	C-H bend and thiophene distortion
$\nu_{18} + \nu_{25}$	–	1267	>100	–
$2\nu_{25}$	–	1375	14.9	–
ν_{67}	1524	1529	4.1	delocalized C=C stretch
ν_{69}	1596	1596	5.1	delocalized C=C stretch
$\nu_{18} + 2\nu_{25}$	–	1899	–	–
$3\nu_{25}$	–	1986	–	–

[a] B3LYP/aug-cc-pVDZ with empirical scaling factor of 0.970.[45] [b] Ratio of integrated band intensities for 565 and 600 nm Raman excitation wavelengths.

3.4.3 Raman Excitation Profiles

We examine the relative enhancements of the excited-state resonance Raman bands in more detail by tuning the Raman excitation wavelength across the S_1 absorption band. Figure 3.5 shows the experimental Raman spectrum at eight different pump wavelengths ranging from 560 to 600 nm. We limit the Raman pump wavelength to the low-frequency side of the absorption band to prevent dispersive peak shapes, as described in the literature,[8,9,46] and to avoid becoming resonant with the stimulated emission band below ~500 nm.

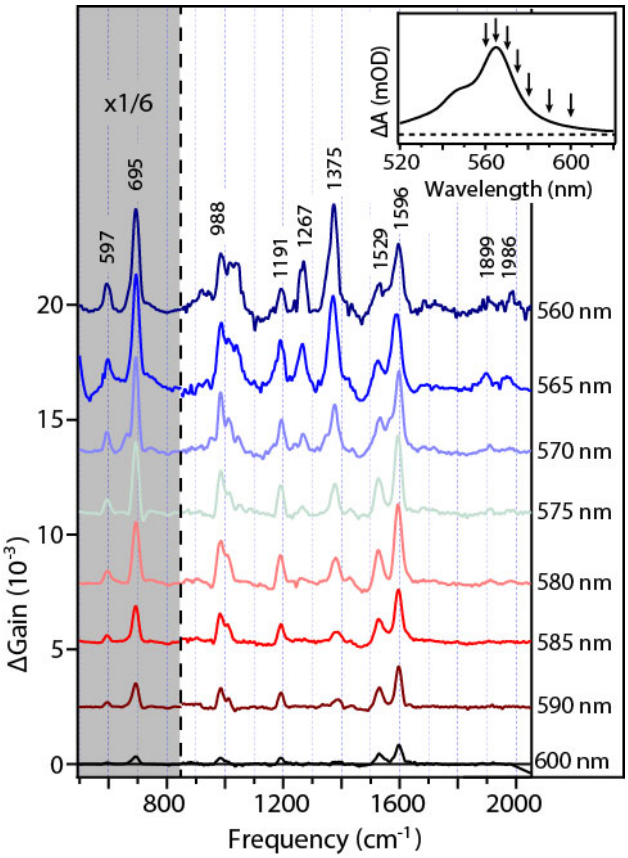

Figure 3.5: Excited-state resonance Raman spectra at $t = 30$ ps delay for eight different Raman excitation wavelengths. The spectra are scaled by 1/6 intensity below 825 cm^{-1} to facilitate comparison of these high-intensity transitions with other regions of the spectrum. Inset shows the Raman excitation wavelengths in reference to the excited-state absorption spectrum.

In order to better highlight the mode dependence of the resonance enhancement effect, Figure 3.6 shows the excitation profiles for eight of the most dominant FSRS bands. The excitation profiles show the variation of the frequency-integrated band intensities as a function of Raman

excitation wavelength. We use integrated band intensities to account for small variations in frequency resolution due to changing experimental parameters at the different excitation wavelengths. By normalizing the integrated intensity of each band to the value obtained at 600 nm, the figure shows the relative enhancements as a function of decreasing wavelength. For reference, the figure also includes the intensity profile of the S_1 excited-state absorption band, which increases by a factor of 9.0 from 600 to 565 nm.

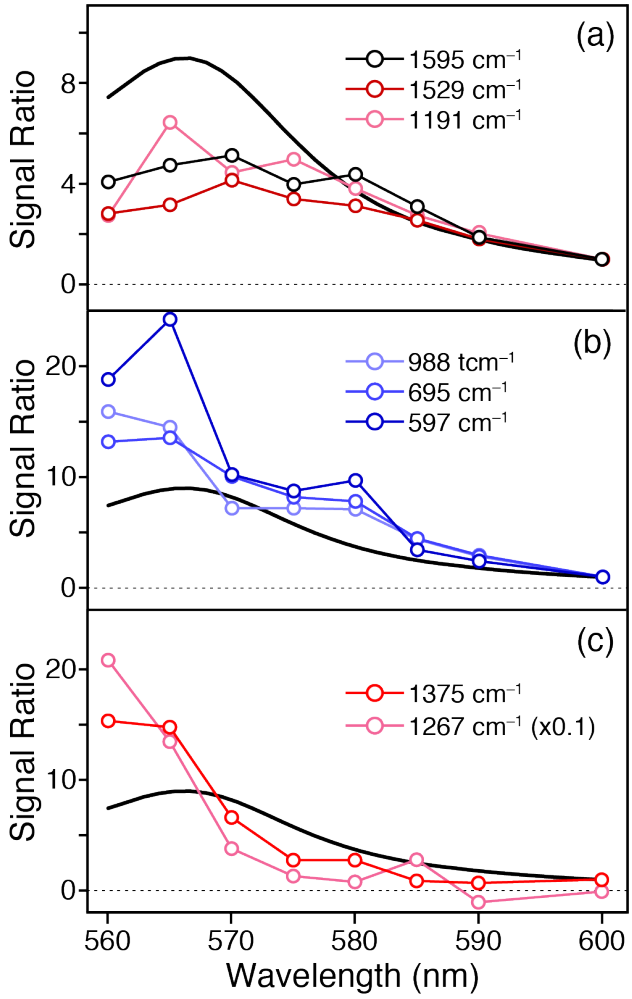

Figure 3.6: Excitation profiles for several excited-state Raman bands. Relative intensity is the integrated Raman gain normalized to the value at 600 nm to show relative enhancement of each band as a function of excitation wavelength. For reference, the solid black line is the excited-state absorption spectrum, also normalized to the value at 600 nm. The three panels show (a) modes with modest gain profiles, (b) modes with stronger resonance enhancement, and (c) overtone and combination modes.

We group the excitation profiles into three different categories based on the relative increase of

the Raman gain between 600 and 565 nm. The first group includes the bands at 1191, 1529, and 1595 cm^{-1}, which have modest gain across the spectrum, increasing slightly less than the 9-fold relative increase of the S_1 absorption band. The second group includes bands that increase more rapidly than the excited-state absorption profile, including those at 597, 695, and 988 cm^{-1}. These two categories have gain profiles that generally follow the intensity of the excited-state absorption band at the Raman excitation wavelength, with the main difference being whether the bands have significant off-resonance intensity or not. Bands with off-resonance intensity are already quite strong for 600 nm Raman excitation, and therefore tend to have more modest gain profiles, while bands that have lower intensity in the off-resonance spectrum increase more rapidly when moving on-resonance.

Finally, a third group of gain profiles includes the bands at 1267 and 1375 cm^{-1}. Notably, these bands are indistinguishable from noise in the early resonance regime, but gain significant intensity as the Raman pump wavelength approaches the S_1 absorption maximum. The delayed onset of the excitation profile for these bands is consistent with the expected behavior for overtone and combination modes in a resonance Raman spectrum, which have essentially no intensity off-resonance, but become quite strong when the resonance condition is fully realized.[22,23,47] Thus, we assign the 1267 and 1375 cm^{-1} bands as the $\nu_{18}+\nu_{25}$ combination and $2\nu_{25}$ overtone modes, respectively. Two features also emerge at 1899 and 1986 cm^{-1} that we assign as transitions to the $\nu_{18}+2\nu_{25}$ combination and $3\nu_{25}$ overtone modes. A band near 1048 cm^{-1} has similar behavior, consistent with the $\nu_{10}+\nu_{25}$ combination mode, based on our previous assignment of the ν_{10} fundamental at 382 cm^{-1}.[13] Strong overtone and combination modes are a signature of large geometry changes in the resonant (upper) electronic state, therefore the prominent progression in ν_{25} points to a very large displacement and correspondingly intense Franck-Condon activity along the thiophene symmetric C-S-C stretching coordinate for $S_n \leftarrow S_1$ excitation of DPT.

3.4.4 Calculated Excited-State Resonance Raman Spectra

For comparison with experiment, we simulate the excited-state resonance Raman spectrum of DPT using either TD-DFT or EOM-CCSD, and the time-dependent formalism described above. In short, we find the optimized S_1 geometry and then use equation 3.6 to calculate resonance Raman intensities from the S_n-S_1 transition strengths and S_n gradients for states up to $n = 20$. We obtain the gradients numerically by calculating the energies at small positive and negative displacements along each of the S_1 normal mode coordinates relative to the S_1 equilibrium geometry.

Figure 3.7 shows the results from TD-DFT with B3LYP/aug-cc-pDVZ. The top panel of the figure compares the experimental transient absorption spectrum with the calculated $S_n \leftarrow S_1$ transitions, including a simulated excited-state absorption spectrum with 0.25 eV Gaussian broadening. We estimate an experimental oscillator strength of $f \approx 0.3$, but only two of the calculated transitions have $f > 0.01$, and both of these are shifted to much longer wavelength. Nevertheless, the lower panel of the figure compares the experimental FSRS spectrum at an excitation wavelength of 570 nm with the simulated excited-state resonance Raman spectra for each of the higher-lying states with $f > 0.004$. The simulated Raman spectra include 25 cm^{-1} Lorentzian broadening, and we divide the spectrum for each state by the oscillator strength ($f \propto E_p|\mu_{ni}|^2$) to allow comparison among states with very different transition strengths.

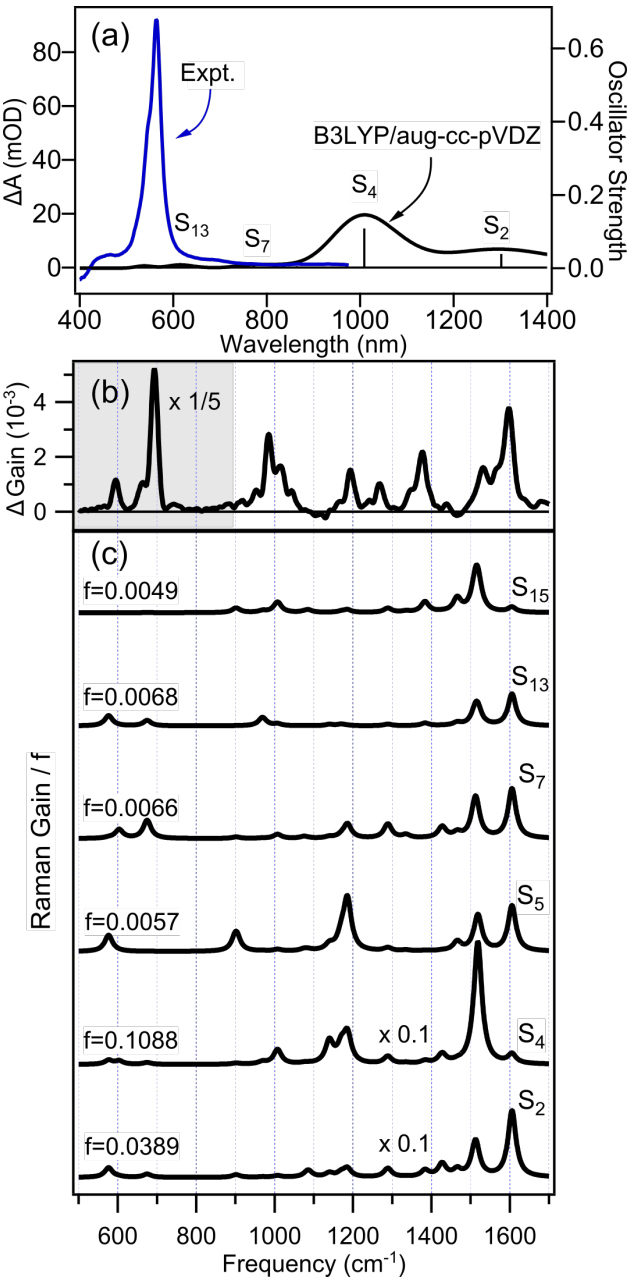

Figure 3.7: Comparison of experimental transient absorption and FSRS spectra at $t = 30$ ps delay with the simulated excited-state spectra from TD-DFT (B3LYP/aug-cc-pVDZ). The simulated electronic spectrum in (a) includes 0.25 eV Gaussian broadening. The lower panel compares (b) the experimental FSRS spectrum at 570 nm Raman excitation wavelength, with (c) the simulated resonance Raman spectra for calculated transitions with $f > 0.004$. Simulated Raman spectra include 25 cm^{-1} Lorentzian broadening, and have been divided by f to facilitate comparison of states with low S_n-S_1 transition strength.

The simulated spectra in the lower panel of Figure 3.7 highlight the important role of geometry changes in the upper states in determining the relative resonance Raman scattering intensities.

Each of the electronic states gives a distinct resonance Raman spectrum, but most have a relatively large gradient in the ethylenic stretching modes at 1524 and 1596 cm^{-1} due to excitation of the conjugated π electrons. In contrast with the calculated off-resonance spectrum in Figure 3.4, several of the states also have noticeable intensity in the lower frequency thiophene distortion modes at 569 and 669 cm^{-1}, although none are as intense as the experimental bands. Notably, the TD-DFT spectrum for S_7 is the only one that correctly predicts the relative intensities for the pair of modes at 569 and 669 cm^{-1}. The spectrum for S_7 also correctly predicts that there are several bands in the intermediate frequency range (not including overtone and combination modes, which are excluded from our simulation). However, given the low oscillator strength (0.0066), the calculated S_7-S_1 transition is not a good candidate to explain the experimental FSRS spectrum. Transitions to S_4 and S_2 have more reasonable oscillator strengths, but are shifted to much longer wavelength and do not match the experimental FSRS spectrum very well.

The poor agreement between the calculated and experimental spectra in Figure 3.7 suggests that TD-DFT does not accurately reproduce the higher-lying electronic states of DPT. This result is not unexpected, because TD-DFT is a single reference method that neglects double excitation and other effects that are likely to play a role in states that are accessible by sequential two-photon excitation.[48,49] Higher-level EOM-CCSD calculations are computationally more expensive than TD-DFT, but explicitly treat double excitations.

Figure 3.8 compares the experimental results with simulated electronic and resonance Raman spectra from EOM-CCSD/6-31G*. We use a relatively small basis set for the EOM-CCSD calculations because the S_1 geometry optimization and vibrational frequency calculations are computationally expensive. Even with the small basis set, the calculated $S_n \leftarrow S_1$ transitions from EOM-CCSD are in better agreement than TD-DFT with the experimental transient absorption spectrum. Specifically, the $S_5 \leftarrow S_1$ transition has the correct oscillator strength, and is relatively close to the experimental wavelength. The 0.64 eV difference between the experimental transient absorption band and the calculated $S_5 \leftarrow S_1$ transition energy may be a result of the limited basis set for the EOM-CCSD calculations. S_5 also has up to $\sim$25% double excitation character, which might ex-

plain the absence of a similar transition in the TD-DFT calculation.

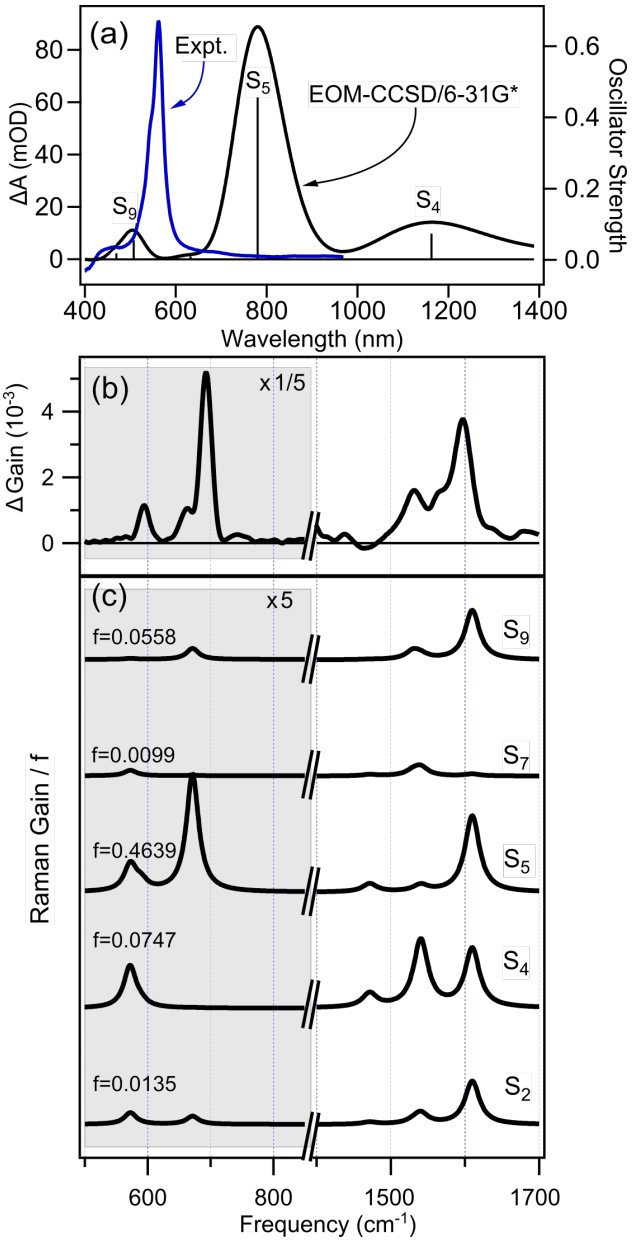

Figure 3.8: Comparison of experimental transient absorption and FSRS spectra with the simulated spectra from EOM-CCSD/6-31G*. See Figure 3.7 caption for details. The simulated Raman spectra in (c) include only seven vibrations due to computational cost.

The lower panel of Figure 3.8 shows the simulated resonance Raman spectra using EOM-CCSD/6-31G* for all of the electronic states with $f > 0.004$. Although EOM-CCSD is too expensive for a complete vibrational analysis, we simulate two key regions of the Raman spectrum by calculating S_n gradients along seven of the S_1 normal mode coordinates. These modes include

some that are responsible for the strongest transitions in the experimental spectrum, as well as a few that are not as prominent. Several of the calculated spectra have features that resemble the experimental FSRS spectrum, but the best agreement is for state S_5, which also has the largest oscillator strength. The simulated spectrum for S_5 correctly predicts the relative Raman intensities in both the high- and low-frequency regions of the experimental spectrum, including most notably the relatively strong transition near 700 cm^{-1}. The transition to S_9 also has some favorable features, but a much lower calculated oscillator strength. Considering both the calculated electronic transition strengths and the simulated resonance Raman spectra, S_5 provides the best representation of the upper electronic state in the experimental transient absorption spectrum of DPT.

The electron density difference map in Figure 3.9 shows the electronic structure change associated with the $S_5 \leftarrow S_1$ transition in the EOM-CCSD calculation. The electron density alternates along the long axis of the molecule due to the change in π bonding pattern, and there is a reduction of electron density in non-bonding sulfur orbitals. The net change in electron density is responsible for the displacement of the upper potential energy surface relative to S_1, but the gradients provide a more intuitive picture by projecting those structural changes onto the S_1 normal modes.

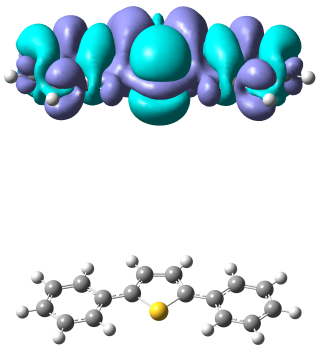

Figure 3.9: Electron density difference map for the $S_5 \leftarrow S_1$ transition from EOM-CCSD/6-31G*. Blue indicates a decrease in density and purple indicates an increase. The ball and stick model shows the orientation of the molecule for reference.

3.5 Discussion

The dynamics of higher-lying excited states are difficult to probe, because strong coupling and a high density of states above S_1 leads to rapid non-adiabatic dynamics. As Kasha's rule predicts,[50] molecules typically relax back to S_1 within $\sim$200 fs or less.[51] This rapid electronic relaxation does not leave much time for the system to evolve on the upper surfaces, therefore the initial, "impulsive" motions out of the Franck-Condon region are likely to be important in determining the efficacy of reaction channels that are only accessible from the higher-lying states. Given the very short lifetimes, transient electronic absorption does not usually have sufficient time (or frequency) resolution to observe wave packet motions in the higher-lying states of a polyatomic molecule.[17,18] However, resonance Raman inherently probes the motion out of the Franck-Condon region. Therefore, the mode-dependent resonance enhancements in FSRS spectra provide a direct window on the ultrafast dynamics within the first few tens of fs, including structural information based on the vibrational motions involved.

The mode-specific resonance enhancements in the experimental FSRS spectrum of DPT probe the upper electronic state in the $S_n \leftarrow S_1$ transient absorption of DPT. The resonance Raman measurement gives a projection of the Franck-Condon dynamics in S_n onto the S_1 normal modes.[52] The strong resonance enhancement of ν_{25}, including a prominent progression of overtone and combination bands involving this mode, indicates that the primary motion in S_n is initially along a delocalized C-S-C symmetric stretching and phenyl deformation coordinate, with additional contributions from the ring distortion and ethylenic stretching motions identified in Table 3.1. While some of these motions could be predicted *a priori* based on the change in π bonding between the two states (as in Figure 3.9), or even from the vibronic structure of the experimental excited-state absorption spectrum (Figure 3.1), the relative Raman intensities provide a more quantitative picture of the upper-state potential energy surface by mapping the initial dynamics onto the S_1 normal modes.

There are many examples where resonance Raman spectroscopy probes the ultrafast dynamics of a molecule excited above S_1.[11,44,53–55] In this case, however, we use the transient FSRS spec-

trum to probe the upper-state dynamics after excitation from the relaxed S_1 geometry, rather than the equilibrium ground-state geometry. Not only is it possible to access different electronic states using sequential excitation, but also the geometry change between S_0 and S_1 allows access to new regions of the upper potential energy surface. In the case of DPT, the Franck-Condon dynamics in the higher-lying state simply respond to a change in the conjugated π bonding configuration. In more reactive molecules, a similar measurement could reveal new reaction pathways that are not accessible directly from S_0. For example, we have shown elsewhere that the sequential two-photon excitation of a photochromic molecular switch leads to a different reaction efficiency than single photon excitation from the ground-state geometry.[17,18] It remains to be seen if the resonant FSRS measurement can provide similar information about the upper state for a molecule that is still evolving on the first excited state.

Experimental resonance enhancements from FSRS spectra also provide a benchmark for comparison with excited-state calculations. For example, there has been growing interest in calculating accurate excited-state absorption spectra of conjugated polymers and related compounds, in order to better understand the nature of the electronic transition, and therefore to extract the most information content from the experimental transient absorption spectrum.[49] Comparison of the calculated and experimental excited-state resonance Raman spectra could provide an important reference point for assessing the quality of calculated transient absorption spectra. Higher-lying electronic states are particularly challenging to calculate because of strong electronic coupling and the rapidly increasing density of states above S_1. The situation is even more complicated for transitions between two excited states, due to additional contributions from states with double (or higher) excitation character. Although it can be difficult to evaluate the quality of excited-state calculations based on electronic transition energies and oscillator strengths alone, a comparison of the experimental Raman intensities with the calculated gradients is a more sensitive test of the calculated upper-state potential energy surface.

In the case of DPT, poor agreement between the simulated spectra and experiment reveal significant short-comings in the TD-DFT calculations for predicting the upper electronic states, possibly

due to multiple excitation character for transitions originating from the $S_1(\pi\pi^*)$ state. The EOM-CCSD calculations are more promising, although further evaluation is necessary to confirm that the better agreement with experiment is not fortuitous. DPT has many favorable characteristics that allow us to probe the upper state. In particular, DPT has a long excited-state lifetime and an intense, isolated excited-state absorption band in the transient absorption spectrum. The measurement is further simplified by allowing the molecule to dissipate excess energy and relax to the thermally equilibrated S_1 minimum in order to probe the upper state from a stationary intermediate. The theoretical treatment, in this case, is also simplified by making several key approximations. For example, we neglect any contributions from Herzberg-Teller coupling or Duschinsky rotation, which often complicate even ground-state Raman measurements. In addition, Raman de-enhancement effects due to competing contributions from different upper states could be significant for higher-lying states due to the rapidly increasing density of states above S_1.[56–58]

3.6 Conclusions

Although most FSRS studies do not explicitly consider the resonance condition, the experimental resonance Raman spectra are sensitive to the upper state. Using a tunable Raman excitation wavelength, we have investigated the mode-specific resonance enhancements for DPT in order to probe the higher-lying excited state. The Raman gain profiles indicate that the resonant upper electronic state (S_n) is primarily displaced along delocalized coordinates with significant C-S-C bending and symmetric stretching. The Raman gain profiles for DPT also highlight contributions from combination and overtone bands involving these modes.

Simulating the resonance Raman spectrum using a very simple implementation of the time-dependent resonance Raman formalism is sufficient to reproduce the basic details of the experimental measurement. However, our results show that the calculated spectra depend on the level of theory. Although limited to only a few vibrations, the simulated resonance Raman spectrum using EOM-CCSD/6-31G* provides a better representation of the experimental spectrum than either the off-resonance calculation or the simulated Raman spectrum using TD-DFT.

3.7 Appendix: Depolarization Ratios

The depolarization of a Raman transition is defined by the ratio of the scattering polarized perpendicular to the Raman pump versus the scattering polarized parallel to the Raman pump.[22] The theoretical values allowed for the ratio range from zero to infinity but commonly are limited to between 0.3 and 0.75 based largely on the symmetry of the vibrations.[59] In the case of resonantly enhanced Raman scattering the polarizability matrix elements which result in the enhanced Raman transitions can only be observed in totally symmetric vibrations. Based on this condition when only resonantly enhanced vibrations are observed in the spectrum, the resulting depolarization ratio has a default value of one third in the absents of Herzberg-Teller coupling.[60] The depolarization ratio can vary from this quantity under specific conditions. If two electronic transitions are resonant with the Raman pump wavelength and the transition dipole for the two electronic states have different vectors, an anomalously large depolarization ratio will be observed.[22,59] A consequence is that as a wavepacket evolves along an adiabatic potential energy surface the character of the adiabatic state changes leading to changes in the depolarization ratio.

However, since Raman is inherently sensitive to changes in molecular structure, a dynamic system that evolves along an adiabatic potential can also be observed as frequency shifts of the pertinent vibrations.[60] However, the depolarization ratio is going to be more sensitive to the wave packet motion in modes that affect the transition dipole. This scattering is represented by the "B term" and represents a breakdown in the Condon approximation.[22]

As discussed so far the considerations for depolarization ratios is independent of the starting state and only assumes that an electronic transition exists near the Raman pump wavelength. In FSRS additional conditions complicate the application of depolarization ratios. When starting from the S_1 state, the density of states within spectral region corresponding to visible re-excitation is significantly more congested. Based on calculations of state transition energies, having ten states near resonance with the Raman pump wavelength is reasonable. Two pathways can lead to the anomalous depolarization of Raman bands. As described above having two electronic transitions with different dipole orientations causes anomalous ratios. The second pathway involves non-

adiabatic coupling of two states near the Franck-Condon geometry of the resonant state. In this case, the transition dipoles for the two states must still have different orientations. These two mechanisms are not easily distinguishable experimentally and given the density of states inherent with FSRS measurements, are commonly viable.

For spectral analysis of molecular species, depolarization ratios will often have anomalous ratios which does provide additional information about vibrational symmetry and electronic state symmetry, but will otherwise match the evolution of the transient electronic spectrum. However, in short time dynamics, the evolution of the depolarization ratio can tell us about the relaxation along the S_1 state, where the most dramatic changes in state character are likely to occur.[60]

With the large density of states in the adiabatic state picture, the number of potentially coupling states quickly becomes difficult to manage. As state degeneracy near conical intersections is difficult to handle computationally, states with strong non-adiabatic coupling near the Franck-Condon geometry are simultaneously the most important and most difficult to assess when predicting the structure of the Raman spectrum and the depolarization ratios.

The A^{IV} term for Raman scattering, assuming the final and initial electronic states are the same is represented by:

$$A^{IV} = \frac{1}{\hbar}(\rho^0_{e^g e^n})(\rho^0_{e^n e^i}) \sum_{\nu_k} \left(\frac{\langle \nu^f_k | \nu^n_k \rangle \langle \nu^n_k | \nu^i_k \rangle}{\omega_{e^n \nu^n; e^i \nu^i} - \omega_p - i\Gamma_{e^n \nu^n_k}} \right), \tag{3.7}$$

where $\rho^0_{e^n e^g}$ is the electronic transition dipole integral between the unperturbed states containing the ν^n and ν^g vibrational states, $\langle \nu^n | \nu^i \rangle$ is the integral between the vibrational states n and i, $\omega_{e^n \nu^n; e^i \nu^i}$ is the frequency difference between states n and i, ω_p is the frequency of the incident electric field and Γ_n is the dephasing lifetime of state n.[22]

$$\begin{aligned} B^{IV} = &\frac{1}{\hbar^2}(\rho^0_{e^g e^s}) \frac{h_{e^s e^r}}{\omega^r_e - \omega^s_e} (\rho^0_{e^r e^i}) \sum_{\nu_k} \left(\frac{\langle \nu^f_k | Q_k | \nu^n_k \rangle \langle \nu^n_k | \nu^i_k \rangle}{\omega_{e^n \nu^n_k; e^i \nu^i_k} - \omega_p - i\Gamma_{e^n \nu^n_k}} \right) + \\ &\frac{1}{\hbar^2}(\rho^0_{e^g e^r}) \frac{h_{e^r e^s}}{\omega^s_e - \omega^r_e} (\rho^0_{e^s e^i}) \sum_{\nu_k} \left(\frac{\langle \nu^f_k | \nu^n_k \rangle \langle \nu^n_k | Q_k | \nu^i_k \rangle}{\omega_{e^n \nu^n_k; e^i \nu^i_k} - \omega_p - i\Gamma_{e^n \nu^n_k}} \right), \end{aligned} \tag{3.8}$$

The additional term $h_{e^s e^r}$ represents the vibrationally dependent coupling of the electronic states

e^s and e^r which are both dipole allowed transitions. Specifically:

$$h_{e^s e^r} = \langle e^s(Q_0)| \left(\frac{\partial \hat{H}_e}{\partial Q_k} \right) |e^r(Q_0)\rangle \tag{3.9}$$

where Q_k is the normal mode displacements and $\hat{H}_e$ is the electronic hamiltonian. The electronic coupling is assumed to be weak to remain in the perturbative limit.

The measured depolarization ratios for the resonant FSRS measurement of DPT are shown in figure 3.10. These ratios all show anomalously large values and show no explicit trend as the Raman pump wavelength changes the resonance condition. Since we have established that these are resonantly enhanced, totally symmetric vibrations, contributions from electronic states with differing symmetry is not possible. We can conclude that there are contributions from multiple electronic transitions to the enhancement, but in the case of DPT, no explicit insight is provide about those states or their structure.

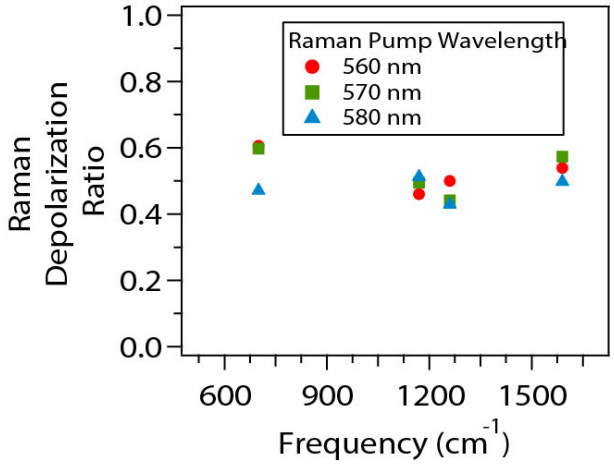

Figure 3.10: The depolarization ratios of select vibrational modes at three Raman pump wavelength. The wavelengths of 580, 570, and 560 nm approach the peak of the excited state absorption. In all cases the ratios are anomalously large.

3.8 Bibliography

[1] McCamant, D. W., Kukura, P., and Mathies, R. A. (2003) Femtosecond Time-Resolved Stimulated Raman Spectroscopy: Application To the Ultrafast Internal Conversion in Beta-Carotene. *Journal of Physical Chemistry A 107*, 8208–8214.

[2] Lee, S. Y., Zhang, D., McCamant, D. W., Kukura, P., and Mathies, R. A. (2004) Theory of Femtosecond Stimulated Raman Spectroscopy. *J Chem Phys 121*, 3632–3642.

[3] McCamant, D. W., Kukura, P., and Mathies, R. A. (2003) Femtosecond Broadband Stimulated Raman: a New Approach For High-Performance Vibrational Spectroscopy. *Appl Spectrosc 57*, 1317–1323.

[4] Kukura, P., McCamant, D. W., and Mathies, R. A. (2007) Femtosecond Stimulated Raman Spectroscopy. *Annual Review of Physical Chemistry 58*, 461–488.

[5] Pontecorvo, E., Ferrante, C., Elles, C. G., and Scopigno, T. (2014) Structural Rearrangement Accompanying the Ultrafast Electrocyclization Reaction of a Photochromic Molecular Switch. *Journal of Physical Chemistry B 118*, 6915–6921.

[6] Tang, L. T., Liu, W. M., Wang, Y. L., Zhao, Y. X., Oscar, B. G., Campbell, R. E., and Fang, C. (2015) Unraveling Ultrafast Photoinduced Proton Transfer Dynamics in a Fluorescent Protein Biosensor for Ca2+ Imaging. *Chemistry-a European Journal 21*, 6481–6490.

[7] Valley, D. T., Hoffman, D. P., and Mathies, R. A. (2015) Reactive and Unreactive Pathways in a Photochemical Ring Opening Reaction From 2D Femtosecond Stimulated Raman. *Physical Chemistry Chemical Physics 17*, 9231–9240.

[8] Batignani, G., Pontecorvo, E., Giovannetti, G., Ferrante, C., Fumero, G., and Scopigno, T. (2016) Electronic Resonances in Broadband Stimulated Raman Spectroscopy. *Sci Rep 6*, 18445.

[9] Cen, Q. Y., He, Y. H., Xu, M., Wang, J. J., and Wang, Z. H. Wavelength Dependent Resonance Raman Band Intensity of Broadband Stimulated Raman Spectroscopy of Malachite Green in Ethanol. *Journal of Chemical Physics 142*, 114201.

[10] Yu, W. J., Donohoo-Vallett, P. J., Zhou, J. W., and Bragg, A. E. Ultrafast Photo-Induced Nuclear Relaxation of a Conformationally Disordered Conjugated Polymer Probed with Transient Absorption and Femtosecond Stimulated Raman Spectroscopies. *Journal of Chemical Physics 141*, 044201.

[11] Fujisawa, T., Kuramochi, H., Hosoi, H., Takeuchi, S., and Tahara, T. (2016) Role of Coherent Low-Frequency Motion in Excited-State Proton Transfer of Green Fluorescent Protein Studied by Time-Resolved Impulsive Stimulated Raman Spectroscopy. *Journal of the American Chemical Society 138*, 3942–3945.

[12] Weigel, A., Dobryakov, A., Klaumunzer, B., Sajadi, M., Saalfrank, P., and Ernsting, N. P. (2011) Femtosecond Stimulated Raman Spectroscopy of Flavin after Optical Excitation. *Journal of Physical Chemistry B 115*, 3656–3680.

[13] Barclay, M. S., Quincy, T. J., Williams-Young, D. B., Caricato, M., and Elles, C. G. (2017) Accurate Assignments of Excited-State Resonance Raman Spectra: a Benchmark Study Combining Experiment and Theory. *Journal of Physical Chemistry A 121*, 7937–7946.

[14] Myers, A. B., and Pranata, K. S. (1989) Excited-State Geometry and Dynamics of trans-Hexatriene: a Resonance Raman Intensity Study. *The Journal of Physical Chemistry 93*, 5079–5087.

[15] Myers, A. B., Mathies, R. A., Tannor, D. J., and Heller, E. J. (1982) Excited State Geometry Changes From Preresonance Raman Intensities: Isoprene and Hexatriene. *The Journal of Chemical Physics 77*, 3857–3866.

[16] Ma, H., Liu, J., and Liang, W. (2012) Time-Dependent Approach to Resonance Raman Spec-

tra Including Duschinsky Rotation and Herzberg–Teller Effects: Formalism and Its Realistic Applications. *Journal of Chemical Theory and Computation 8*, 4474–4482.

[17] Ward, C. L., and Elles, C. G. (2012) Controlling the Excited-State Reaction Dynamics of a Photochromic Molecular Switch with Sequential Two-Photon Excitation. *Journal of Physical Chemistry Letters 3*, 2995–3000.

[18] Ward, C. L., and Elles, C. G. (2014) Cycloreversion Dynamics of a Photochromic Molecular Switch via One-Photon and Sequential Two-Photon Excitation. *The Journal of Physical Chemistry A 118*, 10011–10019.

[19] Albrecht, A. C. (1961) Theory of Raman Intensities. *Journal of Chemical Physics 34*, 1476.

[20] Heller, E. J., Sundberg, R. L., and Tannor, D. (1982) Simple Aspects of Raman-Scattering. *Journal of Physical Chemistry 86*, 1822–1833.

[21] Johnson, A. E., and Myers, A. B. (1996) Solvent Effects in the Raman Spectra of the Triiodide Ion: Observation of Dynamic Symmetry Breaking and Solvent Degrees of Freedom. *Journal of Physical Chemistry 100*, 7778–7788.

[22] Long, D. A. *The Raman Effect : a Unified Treatment of the Theory of Raman Scattering by Molecules*; Wiley: Chichester ; New York, 2002; pp xxiv, 597 p.

[23] Myers, A. B. (1997) 'Time-Dependent' Resonance Raman Theory. *Journal of Raman Spectroscopy 28*, 389–401.

[24] Myers Kelley, A. (2008) Resonance Raman and Resonance Hyper-Raman Intensities: Structure and Dynamics of Molecular Excited States in Solution. *The Journal of Physical Chemistry A 112*, 11975–11991.

[25] Neugebauer, J., Reiher, M., Kind, C., and Hess, B. (2002) Quantum Chemical Calculation of Vibrational Spectra of Large Molecules - Raman and IR Spectra for Buckminsterfullerene. *J. Comp. Chem. 23*, 895–910.

[26] Silverstein, D. W., and Jensen, L. (2012) Vibronic Coupling Simulations For Linear and Nonlinear Optical Processes: Simulation Results. *The Journal of Chemical Physics 136*, 064110.

[27] Heller, E. J. (1975) Wavepacket Path Integral Formulation of Semiclassical Dynamics. *Chemical Physics Letters 34*, 321–325.

[28] Pontecorvo, E., Kapetanaki, S. M., Badioli, M., Brida, D., Marangoni, M., Cerullo, G., and Scopigno, T. (2011) Femtosecond Stimulated Raman Spectrometer in the 320-520nm Range. *Optics Express 19*, 1107–1112.

[29] Pontecorvo, E., Ferrante, C., Elles, C. G., and Scopigno, T. (2013) Spectrally Tailored Narrowband Pulses For Femtosecond Stimulated Raman Spectroscopy in the Range 330-750 Nm. *Optics Express 21*, 6866–6872.

[30] Luo, G., Chutatape, O., and Fang, H. (2001) Experimental Study on Nonuniformity of Line Jitter in CCD Images. *Applied Optics 40*, 4716–4720.

[31] Challa, J. R., Du, Y., and McCamant, D. W. (2012) Femtosecond Stimulated Raman Spectroscopy Using a Scanning Multichannel Technique. *Applied Spectroscopy 66*, 227–232.

[32] Grumstrup, E. M., Chen, Z., Vary, R. P., Moran, A. M., Schanze, K. S., and Papanikolas, J. M. (2013) Frequency Modulated Femtosecond Stimulated Raman Spectroscopy of Ultrafast Energy Transfer in a Donor-Acceptor Copolymer. *Journal of Physical Chemistry B 117*, 8245–8255.

[33] Frisch, M. J. et al. Gaussian09 Revision D.01. Gaussian Inc. Wallingford CT 2009.

[34] Stanton, J. F., Gauss, J., Ishikawa, N., and Headgordon, M. (1995) A Comparison of Single Reference Methods For Characterizing Stationary-Points of Excited-State Potential-Energy Surfaces. *Journal of Chemical Physics 103*, 4160–4174.

[35] Aidas, K. et al. (2014) The Dalton Quantum Chemistry Program System. *WIREs Comput. Mol. Sci. 4*, 269–284.

[36] Vahtras, O., Ågren, H., Jørgensen, P., Jensen, H. J. A., Helgaker, T., and Olsen, J. (1992) Multiconfigurational Quadratic Response Functions For Singlet and Triplet Perturbations: the Phosphorescence Lifetime of Formaldehyde. *J. Chem. Phys. 97*, 9178–9187.

[37] Hettema, H., Jensen, H. J. A., Jørgensen, P., and Olsen, J. (1992) Quadratic Response Functions For a Multiconfigurational Self-Consistent Field Wave Function. *J. Chem. Phys. 97*, 1174–1190.

[38] Ågren, H., Vahtras, O., Koch, H., Jørgensen, P., and Helgaker, T. (1993) Direct Atomic Orbital Based Self-Consistent-Field Calculations of Nonlinear Molecular Properties. Application To the Frequency Dependent Hyperpolarizability of Para-Nitroaniline. *J. Chem. Phys. 98*, 6417–6423.

[39] Caricato, M., Trucks, G. W., Frisch, M. J., and Wiberg, K. B. (2010) Electronic Transition Energies: a Study of the Performance of a Large Range of Single Reference Density Functional and Wave Function Methods on Valence and Rydberg States Compared to Experiment. *Journal of Chemical Theory and Computation 6*, 370–383.

[40] Castro, C. M., Delgado, M. C. R., Hernandez, V., Hotta, S., Casado, J., and Navarrete, J. T. L. (2002) Efficiency of the pi Conjugation in a Novel Family of alpha,alpha '-bisphenyl End-Capped Oligothiophenes by Means of Raman Spectroscopy. *Journal of Chemical Physics 116*, 10419–10427.

[41] Chosrovian, H., Rentsch, S., Grebner, D., Dahm, D. U., Birckner, E., and Naarmann, H. (1993) Time-Resolved Fluorescence Studies on Thiophene Oligomers in Solution. *Synthetic Metals 60*, 23–26.

[42] Zheldakov, I. L., Wasylenko, J. M., and Elles, C. G. (2012) Excited-State Dynamics and Efficient Triplet Formation in Phenylthiophene Compounds. *Physical Chemistry Chemical Physics 14*, 6211–6218.

[43] Zhou, J., Yu, W., and Bragg, A. E. (2015) Structural Relaxation of Photoexcited Quaterthiophenes Probed with Vibrational Specificity. *The Journal of Physical Chemistry Letters 6*, 3496–3502.

[44] Zhou, J., Yu, W., and Bragg, A. E. (2015) Structural Relaxation of Photoexcited Quaterthiophenes Probed with Vibrational Specificity. *The Journal of Physical Chemistry Letters 6*, 3496–3502.

[45] NIST Computational Chemistry Comparison and Benchmark Database, NIST Standard Reference Database Number 101. 2016; `http://cccbdb.nist.gov/`.

[46] Oscar, B. G., Chen, C., Liu, W. M., Zhu, L. D., and Fang, C. (2017) Dynamic Raman Line Shapes on an Evolving Excited-State Landscape: Insights from Tunable Femtosecond Stimulated Raman Spectroscopy. *Journal of Physical Chemistry A 121*, 5428–5441.

[47] Phillips, D. L., Zgierski, M. Z., and Myers, A. B. (1993) Resonance Raman Excitation Profiles of 1,3-Butadiene in Vapor and Solution Phases. *The Journal of Physical Chemistry 97*, 1800–1809.

[48] Cave, R. J., Zhang, F., Maitra, N. T., and Burke, K. (2004) A dressed TDDFT treatment of the 2Ag states of butadiene and hexatriene. *Chemical Physics Letters 389*, 39–42.

[49] Roseli, R. B., Tapping, P. C., and Kee, T. W. (2017) Origin of the Excited-State Absorption Spectrum of Polythiophene. *The Journal of Physical Chemistry Letters 8*, 2806–2811.

[50] Kasha, M. (1950) Characterization of Electronic Transitions in Complex Molecules. *Discussions of the Faraday Society* 14–19.

[51] Houk, A. L., Zheldakov, I. L., Tommey, T. A., and Elles, C. G. (2015) Two-Photon Excitation of trans-Stilbene: Spectroscopy and Dynamics of Electronically Excited States above S-1. *Journal of Physical Chemistry B 119*, 9335–9344.

[52] Bailey, S. E., Zink, J. I., and Nelsen, S. F. (2003) Contributions of Symmetric and Asymmetric Normal Coordinates To the Intervalence Electronic Absorption and Resonance Raman Spectra of a Strongly Coupled P-Phenylenediamine Radical Cation. *Journal of the American Chemical Society 125*, 5939–5947.

[53] Valley, D. T., Hoffman, D. P., and Mathies, R. A. (2015) Reactive and Unreactive Pathways in a Photochemical Ring Opening Reaction From 2D Femtosecond Stimulated Raman. *Physical Chemistry Chemical Physics 17*, 9231–9240.

[54] Liu, W. M., Tang, L. T., Oscar, B. G., Wang, Y. L., Chen, C., and Fang, C. (2017) Tracking Ultrafast Vibrational Cooling during Excited-State Proton Transfer Reaction with Anti-Stokes and Stokes Femtosecond Stimulated Raman Spectroscopy. *Journal of Physical Chemistry Letters 8*, 997–1003.

[55] Hoffman, D. P., and Mathies, R. A. (2012) Photoexcited Structural Dynamics of An Azobenzene Analog 4-nitro-4 '-Dimethylamino-Azobenzene From Femtosecond Stimulated Raman. *Physical Chemistry Chemical Physics 14*, 6298–6306.

[56] Sun, Z., Lu, J., Zhang, D. H., and Lee, S.-Y. (2008) Quantum Theory of (Femtosecond) Time-Resolved Stimulated Raman Scattering. *The Journal of Chemical Physics 128*, 144114.

[57] Wang, X. H., Valverde-Aguilar, G., Weaver, M. N., Nelsen, S. F., and Zink, J. I. (2007) Resonance Raman De-Enhancement Caused by Excited State Mixed Valence. *Journal of Physical Chemistry A 111*, 5441–5447.

[58] Wu, M., Ray, M., and Sedlacek, A. J. (1998) Raman Resonance De-Enhancement in the Excitation Profile of CS2. *Journal of Chemical Physics 109*, 1352–1358.

[59] Strommen, D. P. (1992) Specific Values of the Depolarization Ratio in Raman-Spectroscopy - Their Origins and Significance. *Journal of Chemical Education 69*, 803–807.

[60] Myers, A. B. (1991) Resonance Raman Depolarization Ratios as a Probe of Ultrafast Excited-State Torsional Dynamics - a Critical-Evaluation. *Journal of Physical Chemistry 95*, 1536–1538.

Chapter 4

Directly Probing the Dynamics of Higher-Lying Excited-States in a Diarylethene-based Molecular Switch by Femtosecond Stimulated Resonance Raman Spectroscopy

4.1 Introduction

Diarylethene-based photoswitches are an interesting class of molecules that exhibit distinct, reversible structural changes when exposed to UV or visible light.[1,2] Exposure to UV light causes a change in the bond order of the ethene bridge and adjacent aryl groups leading to the formation of a new sigma bond. The altered bonding order changes the electronic structure sufficiently to produce a new absorption band, typically in the visible spectrum. Exposure of the closed-ring isomer to visible light then causes cycloreversion to regenerate the open-ring isomer, but often with lower quantum yield than the cyclization reaction. While the cycloreversion quantum yield is often low, studies show that a secondary excitation with a second photon either within a long duration laser pulse or two carefully timed fs pulses can enhance the product formation.[3–7] This reactivity is of particular interest because it provides greater selective control of the cycloreversion process. Developing precision control in diarylethene-based photoswitches makes them attractive candidates for optical data storage and other opto-electronic applications.[2,8–11]

While there is interest in implementing diarylethene photoswitches in larger optical systems, a detailed understanding of the potential energy landscape is required to engineer the desired qualities into molecular systems. In order to probe the impact of higher-lying states, sequential two-photon studies have probed the time dependence and wavelength dependence of the second

absorption event.[3–5,7,12] Higher-lying states refer specifically to electronic states above S_1. The sequential two-photon excitation measurements monitor the ground state bleach at long time delays while changing the delay between the two pump pulses. In this way, the ground-state bleach shows the effect of the secondary excitation on the cycloreversion yield.[3,4] While this is a powerful approach to study the impact of higher-lying electronic states, these 'action' measurements are indirect and do not probe the S_n state directly as the system evolves.

For the diarylethene derivative 1,2-bis(2,4-dimethyl-5-phenyl-3-thienyl) perfluoro-cyclopentene (DMPT-PFCP), when using two 500 nm pump pulses, re-excitation as the molecule relaxes out of the Franck-Condon region has no significant effect on the product formation.[3] In figure 4.1, this corresponds to the S_{1A} region of the potential. However, when the secondary excitation comes after an excited-state barrier crossing, from the region of S_{1B}, product formation of the open ring conformer is enhanced. The spectral shifting and decay of the transient absorption signal associated with the barrier crossing is of particular interest in understanding the structure of DMPT-PFCP excited-states because of its strong wavelength dependence and time dependence of the re-excitation dynamics.[3,13] Specifically, when the re-excitation pulse is changed to an 800 nm pump pulse, the time delayed enhancement correlates with system relaxing out of the Franck-Condon region.[4]

The wavelength dependence of the secondary excitation in the sequential two-photon process sets the stage for the study of DMPT-PFCP with excited-state femtosecond stimulated Raman spectroscopy. While Valley et al. have measured the excited-state Raman spectrum of DMPT-PFCP with an 800 nm Raman pump, their work focused on the S_1 dynamics and did not consider the higher-lying states or their ability to change cycloreversion efficiency via sequential excitation.[14] Through the excited-state resonance condition, excited-state Raman measurements allow us to directly probe the S_n state.

In this chapter, the excited-state Raman spectrum of DMPT-PFCP is measured at a Raman pump wavelength of 400 nm. This measurement complements earlier sequential two-photon absorption measurements[3,4,6,15] by directly probing the S_n state that is responsible for the time-

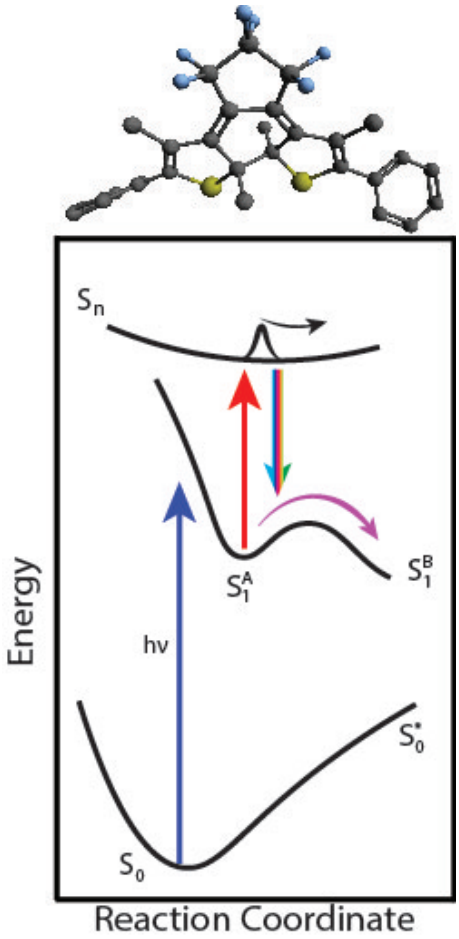

Figure 4.1: The initial population in S_0 is excited by a fs actinic pulse to an electronic excited-state. The system evolves based on the forces applied by the new potential to an energy minimum at S_{1A}. As the system evolves, a ps Raman pump pulse is used to generate Resonant Raman scattering using a higher-lying S_n state. A fs white light continuum pulse overlapped with the ps Raman pump pulse stimulates the Raman scattering.

delayed quantum yield enhancement which occurs with the secondary excitation. Additionally, we compare our results with those of Valley et al. who used an 800 nm Raman pump to perform similar measurements.[14] The comparison highlights the importance of the excited-state resonance condition in terms of the in terms of both the vibrational and electronic spectroscopies.

4.2 Experimental Methods

An amplified Ti:Sapphire laser (Coherent, Legend Elite) with an output of 35 fs pulses at 1 kHz repetition rate pumps additional optical systems. A commercial optical parametric amplifier (OPA;

TOPAS) with two additional stages for non-linear frequency conversion uses a portion of the amplified output to generate the 560 nm actinic pump pulses (75 fs and 6.5 μJ at the sample). The Raman pump beam is produced using 40 μJ of the 800 nm fundamental and a 25 mm long BBO crystal (θ_{cut}=26.6°). Taking advantage of the group velocity mismatch in the long BBO, a spectrally narrow SHG output with approximately ps pulse duration is generated.[16] The Raman pump pulse is further tailored by a $4f$ spectral filter that further narrows the pulse bandwidth and minimizes the temporal asymmetry of the pulse.[17] At the sample, the Raman pump pulses have <20 cm^{-1} bandwidth and >1.0 μJ per pulse. The fs probe pulse is a white-light continuum (WLC) generated by focusing a small portion of the laser fundamental into CaF_2 window on a circularly translating stage. After the sample, a neutral density filter is placed in the path of the probe to attenuate the light and match the dynamic range of the CCD array detector. All three laser pulses intersect in the sample and at a small angle while remaining parallel to the plane of the laser table. The polarization of all laser pulses is vertical in the lab frame.

The sample flows through a cell with 1mm thick CaF_2 windows and 0.5 mm pathlength. Detection is performed using a 1/8 m imaging spectrograph that disperses the probe light onto a 2068 pixel linear CCD array (Hamamatsu, S11156-2048). For stimulated Raman measurements, an 1800 line/mm grating is installed in the spectrograph, and a 50 μm entry slit on the imaging spectrograph leads to a resolution limit of 25 cm^{-1}. Transient absorption measurements used the same imaging spectrograph with a 600 line/mm grating and a 120 μm entry slit for 120 cm^{-1} resolution. The probe intensity is measured using the CCD at a rate of 1 kHz. The actinic pump is chopped at 500 Hz, and the Raman pump is chopped at 250 Hz, relative to the probe, for shot-to-shot averaging and background compensation. Stimulated Raman gain of the ground state is calculated as the ratio of the WLC with and without the Raman Pump incident on the sample. The excited-state Raman spectrum is the difference between the gain with the actinic pump incident minus the gain without the actinic pump.

Due to the combination of resonant actinic and Raman pump pulses, additional electronic absorption produces offset baselines in the excited-state Raman spectra. To correct for this effect,

at each time point the spectrum is fit to a tenth order polynomial to provide a course baseline correction. The polynomial fit takes advantage of a spectral mask to prevent solvent bands from affecting the fit to the baseline. Similar baseline correction is performed on the ground state Raman spectrum and the corrected ground state spectrum is then scaled and added back to the baseline corrected excited-state spectrum to remove negative peaks from solvent depletion. A brief analysis of any suspect features provides an indication of the quality of the baseline and reliability of the correction. Features that appear adjacent to solvent bands must be carefully assessed as they can be artifacts of the baseline correction. Bands that are an artifact of the baseline correction are insensitive to changing excited-state populations and are sensitive to solvent depletion correction. The standard deviation of such regions is several factors larger than the baseline noise of the spectrum. When performing more detailed analysis of the spectra, such as global fitting, inconsistent or unrealistic results isolated in regions of the spectrum can indicate problems with baseline corrections.

The sample solution of 5 mM 1,2-bis(2,4-dimethyl-5-phenyl-3-thienyl)perfluoro-cyclopentene (TCI America) (DMPT-PFCP) is prepared in 20 mL of cyclohexane (spectroscopic grade, Fisher). The sample is then converted to a photostationary state by irradiating the solution using a 310 nm LED for several hours. The solution is flowed through the sample cell by a gear pump and recycled into the sample reservoir. The same 310 nm LED irradiates the sample reservoir during the measurements to help maintain the photostationary state over several hours of laser excitation. Based on UV-vis spectra, there is no evidence of fatigue over the duration of the experiment.

For comparison with the calculated and stimulated Raman spectra of the ground state, the spontaneous Raman spectrum of DMPT-PFCP is collected using a commercial Raman spectrometer (Ramulaser-785 laser source and Raman-HR-TEC-X2 spectrometer, Stellarnet). The spectrometer provides 4 cm^{-1} resolution with a pump laser wavelength of 785 nm. The pump laser is pre-resonant with the visible absorption band of the closed form of DMPT-PFCP, contrasting with the stimulated Raman spectrum with a 400nm Raman pump wavelength which is resonant with the UV ground state absorption.

The ground state Raman spectrum of DMPT-PFCP is calculated using density functional theory (DFT) with B3LYP/aug-cc-pVDZ to optimize the ground state structure, determine normal mode frequencies, and to find Raman intensities. The Raman spectrum for the excited-state is calculated using time-dependent DFT (TD-DFT) with B3LYP/6-31+G* following the same procedure as used for the ground state species. For both spectra, we calculated the Raman intensities by numerical differentiation of the polarizability tensor in each normal mode coordinate using the analytical polarizabilities in the development version of GAUSSIAN.[18,19] No resonance condition is explicitly included in the calculations. However, the resonance condition only affects the magnitude of Raman scattering and not the frequencies.[20] Previous work shows good agreement between the experimental and calculated frequencies at this level of theory, even in the excited-state.[18]

4.3 Results

Figure 4.2 shows the spontaneous and stimulated Raman spectra of DMPT-PFCP along with the calculated Raman spectrum. The calculated Raman spectrum uses DFT with B3LYP/aug-cc-pVDZ to simulate the off-resonance spontaneous Raman scattering and a 0.970 empirical frequency scaling factor.[21] The calculated Raman spectrum is used to assign the vibrations in both experimental spectra. A full table of vibrational frequencies for the Raman spectrum is available in table 4.1, but several vibrational modes are described here due to their contribution to bleaching in the excited-state Raman measurements. The spontaneous Raman spectrum shows a dominant vibrational band (ν_{142}) at 1497 cm^{-1} corresponding to delocalized ethylenic stretching along the backbone of the molecule. An additional peak (ν_{148}) near 1600 cm^{-1} is assigned to localized ethylenic stretching on the phenyl rings.

Stimulated ground-state Raman spectrum collected using the 400 nm ps pump pulse has the same dominant peak as the spontaneous Raman measurement near 1600 cm^{-1} but also includes a stronger shoulder at 1420 cm^{-1}. The increased intensity of the shoulder at 1420 cm^{-1} is due to the resonance of the Raman pump at 400 nm with the low-energy tail of the second absorption band in the ground state spectrum. This band at 1420 cm^{-1} is assigned as ethylenic stretching and

Table 4.1: Experimental and Calculated Raman Frequencies

Exp. Freq. (cm^{-1})	Calc. Freq. (cm^{-1})[a]	Calc. Vibration
505	495	ν_{49}
555	550	ν_{53}
575	567	ν_{55}
592	604	ν_{58}
697	709	ν_{68}
990	973	ν_{90}
1022	1023	ν_{95}
1072	1086	ν_{105}
1120	1112	ν_{107}
1198	1222	ν_{116}
1310	1300	ν_{121}
1370	1386	ν_{129}
1392	1392	ν_{131}
1412	1421	ν_{133}
1480	1482	ν_{145}
1587	1581	ν_{149}

[a]: Calculated frequencies are scaled by a 0.970 empirical factor.[21]

in-plane C-H wagging based on the calculated transitions in this spectral region. Due to the 25 cm^{-1} instrumental resolution limit and lower signal to noise ratio compared with the spontaneous Raman spectrum, many of the peaks with low amplitude are not well resolved in the stimulated Raman spectrum.

Figure 4.3 shows the evolution of the transient electronic absorption spectrum after excitation of DMPT-PFCP using a 560 nm actinic pulse to match the maximum of the ground state absorption. The transient signal represents the electronic absorption of the excited species which is used to track the relaxation of the excited molecules. Panel A shows the spectral evolution over the entire visible spectrum after excitation with a 500 nm pulse The ground-state absorption is shown for comparison. The negative peak centered at 560 nm in the transient spectrum recovers on an 8.6 ps timescale and corresponds the ground state bleach caused the excitation of the sample. The positive signal at 400 nm is the excited-state transition that is probed by the transient Raman measurement.

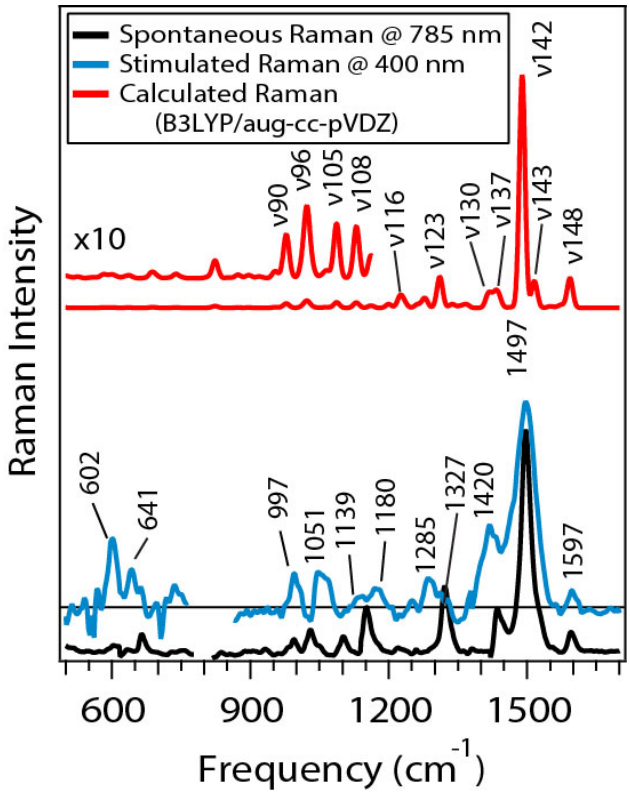

Figure 4.2: The calculated off-resonant Raman spectrum (red) of DMPT-PFCP includes labels of the vibrational normal modes which have been used to make experimental assignments in the stimulated Raman spectrum (blue). The Spontaneous Raman Spectrum (black) of DMPT-PFCP is also presented to highlight the resonance enhancement observed in the stimulated spectrum with the 400 nm Raman pump.

The sample has a static ground-state absorption of <0.1 OD over the probe range (404-462 nm) for the transient Raman measurement. The ground-state absorption decreases by roughly half after excitation with the actinic pump promoting 50% of the ground-state population to the excited-state. During the first few ps, the transient absorption signal in this probe range is several times stronger than the remaining ground state absorption, leading to favorable conditions for transient Raman measurements of the excited-state.

Global analysis of the transient absorption in the 400-460 nm region reveals two time constants of 2.4 $\pm$ 0.1 and 7.2 $\pm$ 0.5 ps for the overall spectral decay. The decay of the spectrum at 404 nm is shown in panel C of figure 4.3. In the spectral region of the excited-state Raman measurement, the 2.4 ps component contributes to less than half of the overall amplitude decay

in the excited-state absorption bands. This short time constant has previously been attributed to spectral shifting associated with a barrier crossing on the excited-state potential surface while the longer time constant corresponds to population relaxation to the ground state.[3,13] Earlier work by our group using the full spectral window reproduced in figure 4.3B, revealed time constants of 3.8 ± 0.3 and 8.6 ± 0.9 ps as a result of global fitting across a wider range of wavelengths.[3] The longer time constants attributed to additional spectral evolution which is poorly captured by the global analysis. Bi-exponential fits to the spectral extremes near 400 and 650 nm show longer time constants, pointing to additional vibrational dynamics, implying that the barrier crossing occurs faster than the measured 3.8 ps.[3]

Previous anisotropy work by our group has shown that the excited state absorptions on either side of the ground state bleach are generated by two different electronic states. The existence of two states allows us to use the two resonance conditions used in both PReP and R-FSRS to reveal important information about the different higher-lying states.

Figure 4.4 shows the excitation wavelengths and the resonance condition that is used in the experiment. The resonance condition at 400nm is close to the minimum of the ground state absorption while providing a strong resonance with the excited state absorption.

The transient Raman spectrum presented in figure 4.6 is obtained in resonance with the excited-state absorption band shown in figure 4.3. The actinic pulse is tuned to 560 nm, and the Raman pump pulse is tuned to 400 nm with a 0.3 ps delay between the actinic and probe pulses. At early times the excited-state Raman spectrum of DMPT-PFCP has a negative peak near 1500 cm^{-1} that is due to the depletion of the ground state population. To simplify excited-state vibrational assignments, we scale the ground-state SRS spectrum to the negative bleaching of Raman bands in the excited-state spectrum then add the scaled ground-state SRS spectrum back into the excited-state spectrum. Figure 4.5 shows the resulting spectrum in which a new peak at 1490 cm^{-1} becomes apparent.

Vibrational assignments in the excited-state are made while accounting for the sensitivity of the measurement to totally symmetric vibrational modes.[18] Briefly, the stimulated resonant Raman

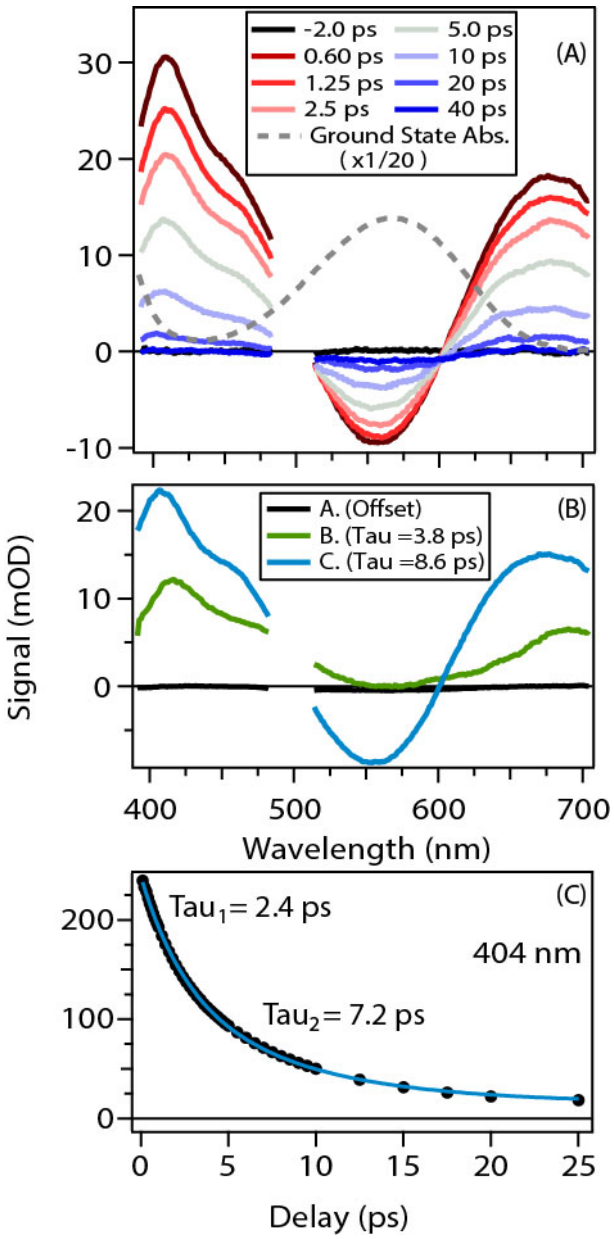

Figure 4.3: The figure shows the excited-state spectrum of DMPT-PFCP. Panel (A) shows the cycloreversion reaction after 500 nm excitation. The negative feature in the center of the spectrum represents the ground state bleach. The excited state absorption decays with 2 time constants with the decay associated spectrum shown in panel (B). Panel (C) uses markers to display data of a single wavelength taken from the R-FSRS data overlaid with a bi-exponential fit to the data.

scattering takes advantage of the electronic transition and therefore the Raman polarizability tensor is dominated by a single tensor element that corresponds to the electronic transition dipole.[22] The selection rules require that the product of the vibronic transitions must span the totally symmetric representation. Since the electronic transition is used twice to generate the vibrational coherence

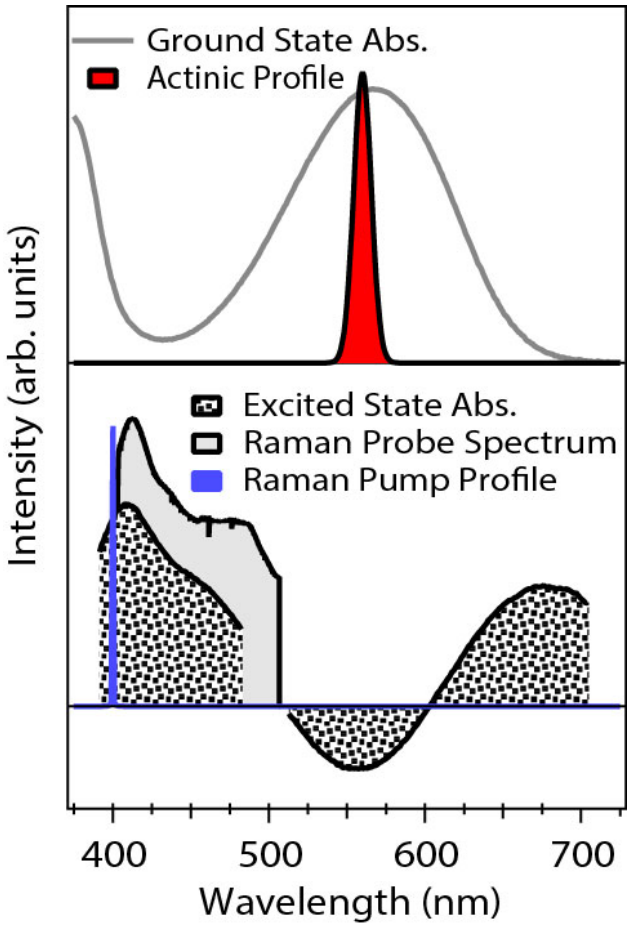

Figure 4.4: The top panel illustrates the ground-state absorption and the wavelength of the actinic pulse used to produce the excited-state population. The bottom panel shows the absorption profile of the excited-state species. The Raman pump and probe profiles are also shown relative to the excited-state absorption.

in the Raman scattering, fundamental vibrations must be totally symmetric to maintain overall transition symmetry. For both ground and excited-state species, the strength of Raman scattering is dependent on the changing polarizability as the molecule vibrates along its normal modes. Furthermore, for the excited-state Raman spectrum, normal modes that correspond to structural changes between the S_1 and S_n electronic states also represent vibrational modes which are enhanced by resonance Raman conditions.

Using the calculated excited-state Raman spectrum and the depletion corrected spectrum in figure 4.5, peaks are assigned while giving consideration the excited-state normal modes symmetry and resonance condition as described above. The Raman spectrum is calculated using TD-DFT

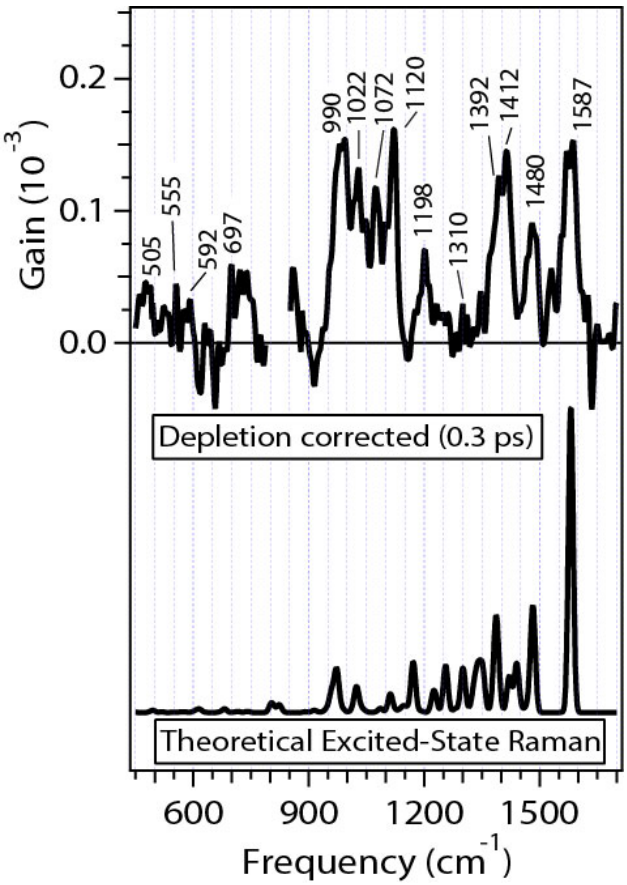

Figure 4.5: FSRS spectrum generated with a 400 nm Raman pump and corrected for ground-state bleach. Vibrational frequencies are listed above the experimental spectrum. The calculated off-resonance excited-state spectrum is also included for reference.

with B3LYP/6-31+G* to both optimize the structure in S_1 and determine Raman activity. No resonance correction is applied to the excited-state calculation, making proper consideration of the normal mode symmetry and resonance condition all the more crucial.[18]

All of the excited-state vibrational assignments are listed in table 4.2 with several key vibrations described here. The 1587 cm^{-1} mode (with calculated assignment ν_{149}) is a C-C stretch primarily in the phenyl rings with small displacements along the thiophene and cyclohexadiene rings. The peak at 1480 cm^{-1} (ν_{145}) is delocalized ethylenic stretching along the carbon backbone. Both the 1480 and 1587 cm^{-1} vibrations are analogous to prominent ground-state vibrations, 1497 and 1597 cm^{-1} respectively, but shifted to lower frequency. The shift is due to the widened potential from relaxed bonding in the $\pi\pi*$ excited-state, relative to the ground state. The 990 cm^{-1} mode (ν_{90}) is

assigned as delocalized ring breathing across the whole molecule, except in the cyclopentane ring, with methyl wagging.

Figure 4.6 shows the evolution of the excited-state Raman spectrum after actinic excitation as well as the off-resonance calculated excited-state Raman spectrum. The semi-log time steps in the figure illustrate the decay of the excited-state vibrational spectrum. Importantly, two new peaks between 1400 and 1500 cm^{-1} grow in before the entire spectrum decays to the baseline by 25 ps. The spectra in figure 4.6 do not include the bleach correction used for the spectrum in figure 4.5 because the bleach represents a direct measurement of the ground-state recovery alongside the excited-state decay.

In figure 4.7 several vibrational bands are chosen to represent the evolution of the vibrational spectrum. The fits overlaying the data are from either single exponential decays or the sum of three exponentials to represent multiple decay processes contributing to the vibrational evolution at each Raman frequency. The only restriction applied to the sum of exponentials fit is that the offset in the long-time limit equals zero. The peak at 1120 cm^{-1} includes only positive contributions and decays monotonically. The decay of the 1120 cm^{-1} peak is representative of the vibrational bands below 1200 cm^{-1} which are well represented by single exponential decays. The signal at 1422 cm^{-1} overlaps several excited-state vibrational features but is centered on the peak that grows on a few ps timescale before decaying back to the baseline at long delay. The signal at 1497 cm^{-1} corresponds to the peak of the most intense ground state vibrational band. The initial negative amplitude of the 1497 cm^{-1} band corresponds to ground state bleach which recovers and leaves a slightly positive feature at intermediate times. The last trace of at 1587 cm^{-1} is centered on the large excited-state vibration just outside of the ground state bleach and exclusively shows excited-state decay.

In order to properly represent the evolution of the Raman spectrum between 1350 and 1550 cm^{-1} three exponential terms are required. The transient absorption spectrum provides time constants of 2.4 and 7.2 ps. A time constant of approximately 2 ps is responsible for decay in all of the vibrational bands. For many vibrational peaks, such as those at 1020, 1120, and 1587 cm^{-1}

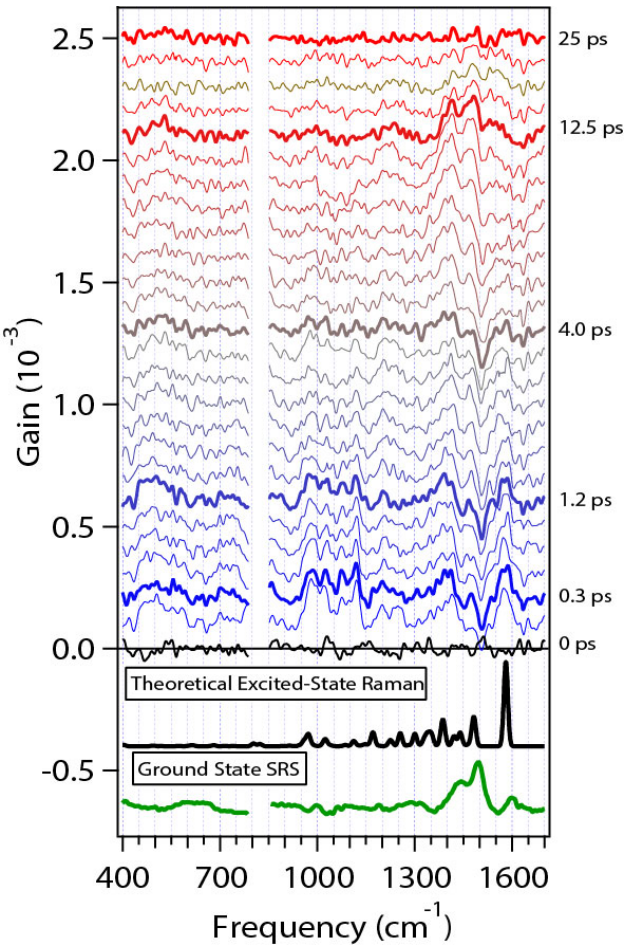

Figure 4.6: The progression of the R-FSRS spectrum of DMPT-PFCP using a 400 nm Raman pump. The offset time delays begin at 0.1 ps delay and recover the baseline structure by 25 ps. A majority of the positive features have completely decayed within the first few ps, however the negative peak at 1500 remains. By 12.5 ps the negative feature has also decayed and two new positive peaks have grown in between 1400 and 1500 cm^{-1}. For comparison the theoretical excited-state Raman spectrum and the experimental ground-state simulated Raman spectrum are displayed.

in figure 4.7, the decay is mono-exponential with this short time constant. The 1020 cm^{-1} peak decays with a time constant of 1.8 ps while the fit to the 1120 cm^{-1} data results in a 2.9 ps time constant and the 1587 cm^{-1} peak reveals a 2.1 ps time constant. Therefore, we fix the fast time constant to 2.4 ps for all fits presented in figure 4.7.

In the trace of 1422 cm^{-1} a large peak is seen to growing into the spectrum on a timescale longer than the initial decay of the 1120 cm^{-1} band and decay to produce a flat baseline. Interestingly the additional time constant from the fit to the data is an intermediate timescale relative to the two time constants from the electronic spectroscopy. The delayed appearance and vibra-

Table 4.2: Excited-State Vibrational Assignments of DMPT-PFCP

Exp. Freq. (cm^{-1})	Calc. Freq.[a] (cm^{-1})	Vibration	Description
505	495	ν_{49}	C-S str.; out of plane CH wagging;
555	550	ν_{53}	Thiophene ring torsion causing cyclohexane ring deformation and C-C str.
575	567	ν_{55}	Thiophene rocking causing ring deformation of cyclohexadiene and phenyl rings; In plane methyl rocking
592	604	ν_{58}	Phenyl ring breathing; Alternating out of plan carbon bending along backbone
697	709	ν_{68}	C-S str.; Alternating out of plane carbon wagging (torrsion) in cyclohexadiene; low amp methyl rocking; low amp phenyl ring breathing
990	973	ν_{90}	Ring breating in cyclohexadiene, thiophene, and phenyl groups; low amp in plane methyl wagging
1022	1023	ν_{95}	C-C str. between reactive carbons; C-C str. in thiophenes; methyl rocking of in plane methyls
1072	1086	ν_{105}	Ring breating in cyclohexadiene; Ring deformation in thiophene and cyclopentane
1120	1112	ν_{107}	Methyl str.; Ring deformation of cyclohexadiene; CH rocking on phenyls
1198	1222	ν_{116}	C-C str. between thiophene and phenyl groups; ring breathing in cyclopentane
1310	1300	ν_{121}	C-C str. coupled between cyclopentane, cyclohexadiene, and thiophene rings
1370	1386	ν_{129}	C-C stetching along conjugated thiophene and cyclohexadiene; Methyl umbrella motions
1392	1392	ν_{131}	C-C str. along conjugated thiophene and cyclohexadiene; Methyl umbrella motions
1412	1421	ν_{133}	C-C str. along carbon backbone; CH rocking on phenyl groups
1480	1482	ν_{145}	C-C str. along carbon backbone
1587	1581	ν_{149}	C-C str. in phenyl rings; small amp str. in thiophene and cyclohexadiene

[a]: Calculated frequencies are scaled by a 0.970 empirical factor.[21]

tional frequency are consistent with the presence of ground state hot bands of the 1496 and 1440 cm^{-1} modes as population relax back to the ground electronic state and energy is distributed into molecular vibrations and the solvent. The hot bands represent vibrational scattering from excited

vibrational states.[20] Due to anharmonic coupling, the frequency of these bands redshifts and appear adjacent to the vibrational bleach of the ground-state species.[20,23] As the Raman pump is positioned on the red edge of the 370 nm electronic absorption band, the experimental conditions provide additional sensitivity to the vibrationally excited ground state. Due to the expected broadening, the absorption band will increase the resonance condition with the 400 nm Raman pump.

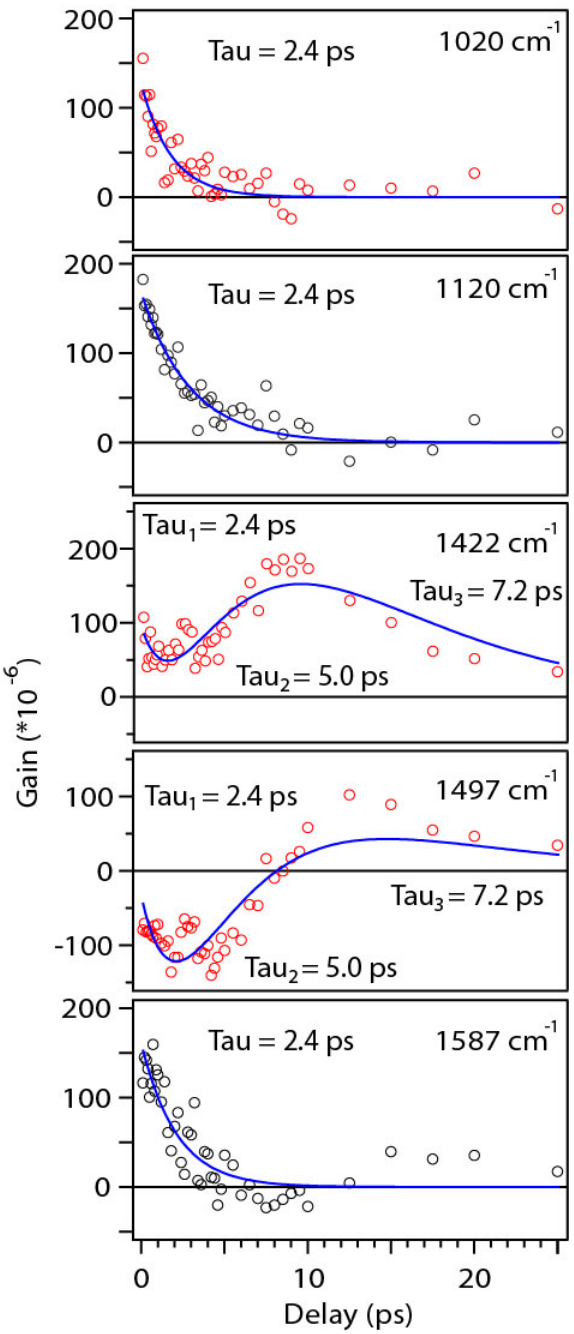

Figure 4.7: The decay kinetics of vibrations at 1020, 1120, and 1587 cm^{-1} show monotonic decay with time constants consistent with the fast electronic decay of 2.4 ps. The 1422 and 1497 cm^{-1} vibrations display more complex evolution. The trace at 1497 cm^{-1} corresponds to the bleach of the ground-state vibrational spectrum. The peak at 1422 cm^{-1} follows the evolution of one of the observed hot bands.

4.4 Discussion

The reactivity of the DMPT-PFCP system can be discussed by considering the central cyclohexadiene ring. Historically, the reaction is described by a conrotatory motion of the p-orbitals on the reactive carbon to break the σ-bond to regenerate the hexatriene moiety. Vibrational modes that preserve C_2 symmetry localized on the cyclohexadiene ring are particularly important since, in the context of the Woodard-Hoffmann rules, these motions closely associated with the cycloreversion reaction coordinate.[24] The conrotatory p-orbital motion associated with the cycloreversion of the cyclohexadiene moiety has C_2 symmetry, and thus vibrations that preserve this symmetry can drive the system to products.[14,24]

The vibrational signature of the excited-state species largely decays on a 2.4 ps timescale while the overall decay of the excited-state species occurs on a 7.2 ps timescale. Therefore, the evolution observed in the 2.4 ps dramatically impacts the Raman scattering of the excited-state species. Since the resonant excited-state Raman measurement is sensitive to the character of the electronic states, in this case S_1 and S_n, the initial 2.4 ps barrier crossing on the excited-state surface is associated with a change in the resonance condition.

A slightly different method of interpreting the disparity between the electronic population decay and vibrational spectral decay is to consider how the Raman resonance condition changes as the system evolves along the S_1 potential energy surface. Specifically, the impact of rehybridization of the reactive carbons on the central cyclohexadiene ring on the electronic transition and overall electronic transition strength. By considering the reactive carbon rehybridization, both the nuclear and electronic components of DMPT-PFCP will evolve with the same timescales through the reaction coordinate. Using this rehybridization framework, it becomes more intuitive to consider the excited-state adiabatic surface in terms of the contributions of diabatic states. The initial excitation is from the 1A to an electronic state of 1B ($\pi\pi^*$) symmetry which quickly relaxes to a lower energy dark state, 2A ($\pi^*\pi^*$), from which the cycloreversion reaction can occur.[25,26]

Calculations by Irie and coworkers, using complete active space self-consistent field methods, showed that for model systems the region of the potential near the S_n to S_1 conical intersection cor-

responds an electronic character to more closely resemble that of the excited open-ring species.[27,28] The change in electronic character is consistent with the rehybridization of the reactive carbons. Specifically, the S_1 minimum near the conical intersection with the ground state has more open-ring (sp^2) character. Importantly, the 2A open form has reduced conjugation between the aryl groups compared to the closed form and overall lower polarizability due to the altered electronic structure induced by the rehybridization. This is further supported by the weak scattering of the open-ring species compared to the closed form in the ground-state.[29] It then follows that rehybridization on the S_1 excited-state reduces the Raman scattering cross-section as DMPT-PFCP evolves along the excited-state reaction coordinate, even for electronic transitions of comparable strength.

Previous work to study excited-state structure and mechanism for cycloreversion used time-resolved pump-repump-probe spectroscopy (PReP) with femtosecond duration pulses. While ps pump-probe measurements of diarylethene derivatives indicate a sequential two-photon process enhanced the cycloreversion yield,[13] PReP measurements of DMPT-PFCP show that the secondary excitation at 500 nm increases the overall quantum yield of the cycloreversion only after a delay between the first and second absorption events.[3] Specifically, the ground state bleach and conversion yield are maximized when the secondary excitation at 500 nm is delayed 5 ps.[3] Meaning that the re-excitation is most effective in driving product formation once the excited-state population is over the initial barrier. When the secondary absorption excites vibrational modes that efficiently couple into the reaction coordinate a significant increase in the quantum yield is expected.

While all enhanced vibrational modes preserve the C_2 symmetry in the central cyclohexadiene ring that drives the ring-opening, those vibrational signatures decay as population crosses the excited-state barrier preventing direct observation of product promoting vibrational modes. Vibrations such as the peaks at 990 and 1120 cm^{-1} should promote the formation of the closed-ring isomer, however, any change in frequency or intensity associated with the excited-state barrier crossing cannot be observed in our measurements. Nonetheless, the effective loss of Raman scattering intensity associated with the barrier crossing and the required delay for enhancement by the secondary excitation at wavelengths <500 nm suggest significant changes to the electronic charac-

ter of S_1 are associated with the excited-state barrier.

While the Raman scattering intensity decreases after crossing the excited-state barrier when resonant with the 400 nm excited-state absorption, the PReP measurements indicate that traversing the barrier before re-excitation is required to observe an increase in cycloreversion yield. Crucially, the time dependent behavior observed when the secondary excitation occurs at 800 nm only requires leaving the Franck-Condon region in order to observe a cycloreversion yield increase. This difference indicates that the two S_n states have very different structural displacements compared with the S_1 state. We can then conclude that the resonance with the S_n state at the 400 nm excited-state absorption band is sensitive the electronic character, specifically as it relates to the hybridization of the reactive carbons. However, the S_n state resonant with the 800 nm excited-state absorption is insensitive to the barrier on the S_1 potential energy surface.

The resonant condition at 400 nm is dominated by modes that evolve with the 2.4 ps lifetime although the transient absorption decay on this timescale is one third or less of the overall amplitude. The 800 nm resonance condition reported by Valley et al. displayed vibrational kinetics with either 3 or 6 ps time constant which is all mono-exponential on the >1 ps time frame. Many of the vibrational peaks reported for the 800 nm resonance Raman agree well with the assignments provided here, but as expected the different higher lying states cause differences in the relative intensities of the vibrational scattering. The 400 nm Raman pump shows greater enhancement in vibrational motions which span the cyclohexadiene and thiophene ring structures, such as the cluster of vibrations between 990 and 1120 cm^{-1}. Meanwhile, the strongest vibrational peaks generated with the 800 nm Raman pump correspond to more isolated motions on either the phenylthiophene aryl groups or the cyclopentane and cyclohexadiene rings. Only the 1587 and 990 cm^{-1} show relatively large scattering intensity in both spectra. The 1587 cm^{-1} mode is largely localized on the phenyl groups, meaning it cannot drive the cycloreversion reaction. However, the 990 cm^{-1} mode involves ring breathing along the carbon backbone and methyl wagging which result in lengthening of the distance between the reactive carbons. Importantly, stretching of the reactive carbon bond corresponds with the cycloreversion reaction coordinate. The differences between these two

studies highlight the importance of the resonance condition. By changing Raman pump resonance in the excited-state, the measurement becomes more or less sensitive to different dynamics along the excited-state potential depending on how the different higher-lying states are displaced from the S_1 excited-state.

4.5 Conclusion

In conclusion, the excited-state resonance Raman of DMPT-PFCP indicates that the resonance wavelength used to observe the excited-state stimulated Raman spectrum significantly impacts the sensitivity to dynamics on the S_1 excited-state surface. The excited-state vibrational spectrum evolves in a manner significantly different relative to the electronic transient absorption. While a $\sim$2 ps component in the excited-state Raman spectrum corresponds to a majority of the vibrational peak decay, it represents less than half of the spectral decay in the electronic transient absorption. The excited-state resonance Raman spectrum pumped at 400 nm in DMPT-PFCP is sensitive to the changing electronic character of the S_1 surface as the system approaches the conical intersection leading back the electronic ground state. Importantly, the sensitivity of the Raman pump to different excited-state dynamics is wavelength dependent. The resonant vibrational spectroscopy provides a means to probe both the evolution along the S_1 surface, but also how the S_n electronic states map onto the reactive coordinate in the S_1 state. Again, this emphasizes the importance of the resonant higher-lying state in the context of changing photochemical reaction yields and the impact the resonance has with regard to experimental observables.

4.6 Bibliography

[1] Irie, M., and Mohri, M. (1988) Thermally Irreversible Photochromic Systems - Reversible Photocyclization of Diarylethene Derivatives. *Journal of Organic Chemistry 53*, 803–808.

[2] Irie, M. (2000) Diarylethenes For Memories and Switches. *Chemical Reviews 100*, 1685–1716.

[3] Ward, C. L., and Elles, C. G. (2012) Controlling the Excited-State Reaction Dynamics of a Photochromic Molecular Switch with Sequential Two-Photon Excitation. *Journal of Physical Chemistry Letters 3*, 2995–3000.

[4] Ward, C. L., and Elles, C. G. (2014) Cycloreversion Dynamics of a Photochromic Molecular Switch via One-Photon and Sequential Two-Photon Excitation. *The Journal of Physical Chemistry A 118*, 10011–10019.

[5] Sotome, H., Nagasaka, T., Une, K., Morikawa, S., Katayama, T., Kobatake, S., Irie, M., and Miyasaka, H. (2017) Cycloreversion Reaction of a Diarylethene Derivative at Higher Excited States Attained by Two-Color, Two-Photon Femtosecond Pulsed Excitation. *Journal of the American Chemical Society 139*, 17159–17167.

[6] Ishibashi, Y., Okuno, K., Ota, C., Umesato, T., Katayama, T., Murakami, M., Kobatake, S., Irie, M., and Miyasaka, H. (2010) Multiphoton-Gated Cycloreversion Reactions of Photochromic Diarylethene Derivatives with Low Reaction Yields Upon One-Photon Visible Excitation. *Photochemical and Photobiological Sciences 9*, 172–180.

[7] Miyasaka, H., Murakami, M., Okada, T., Nagata, Y., Itaya, A., Kobatake, S., and Irie, M. (2003) Picosecond and Femtosecond Laser Photolysis Studies of a Photochromic Diarylethene Derivative: Multiphoton Gated Reaction. *Chemical Physics Letters 371*, 40–48.

[8] Patel, D. G., Walton, I. M., Cox, J. M., Gleason, C. J., Butzer, D. R., and Benedict, J. B. (2014)

Photoresponsive Porous Materials: the Design and Synthesis of Photochromic Diarylethene-Based Linkers and a Metal-Organic Framework. *Chemical Communications 50*, 2653–2656.

[9] Walton, I. M., Cox, J. M., Coppin, J. A., Linderman, C. M., Patel, D. G., and Benedict, J. B. (2013) Photo-Responsive MOFs: Light-Induced Switching of Porous Single Crystals Containing a Photochromic Diarylethene. *Chemical Communications 49*, 8012–8014.

[10] Tani, K., Ishibashi, Y., Miyasaka, H., Kobatake, S., and Irie, M. (2008) Dynamics of Cyclization, Cycloreversion, and Multiphoton-Gated Reaction of a Photochromic Diarylethene Derivative in Crystalline Phase. *Journal of Physical Chemistry C 112*, 11150–11157.

[11] Irie, M., Fukaminato, T., Matsuda, K., and Kobatake, S. (2014) Photochromism of Diarylethene Molecules and Crystals: Memories, Switches, and Actuators. *Chem Rev 114*, 12174–277.

[12] Logunov, S. L., Volkov, V. V., Braun, M., and El-Sayed, M. A. (2001) The Relaxation Dynamics of the Excited Electronic States of Retinal in Bacteriorhodopsin by Two-Pump-Probe Femtosecond Studies. *Proc Natl Acad Sci U S A 98*, 8475–9.

[13] Ishibashi, Y., Okuno, K., Ota, C., Umesato, T., Katayama, T., Murakami, M., Kobatake, S., Irie, M., and Miyasaka, H. (2010) Multiphoton-Gated Cycloreversion Reactions of Photochromic Diarylethene Derivatives with Low Reaction Yields Upon One-Photon Visible Excitation. *Photochemical and Photobiological Sciences 9*, 172–180.

[14] Valley, D. T., Hoffman, D. P., and Mathies, R. A. (2015) Reactive and Unreactive Pathways in a Photochemical Ring Opening Reaction From 2D Femtosecond Stimulated Raman. *Physical Chemistry Chemical Physics 17*, 9231–9240.

[15] Miyasaka, H., Murakami, M., Itaya, A., Guillaumont, D., Nakamura, S., and Irie, M. (2001) Multiphoton Gated Photochromic Reaction in a Diarylethene Derivative. *Journal of the American Chemical Society 123*, 753–754.

[16] Pontecorvo, E., Kapetanaki, S. M., Badioli, M., Brida, D., Marangoni, M., Cerullo, G., and Scopigno, T. (2011) Femtosecond Stimulated Raman Spectrometer in the 320-520nm Range. *Optics Express 19*, 1107–1112.

[17] Pontecorvo, E., Ferrante, C., Elles, C. G., and Scopigno, T. (2013) Spectrally Tailored Narrowband Pulses For Femtosecond Stimulated Raman Spectroscopy in the Range 330-750 Nm. *Optics Express 21*, 6866–6872.

[18] Barclay, M. S., Quincy, T. J., Williams-Young, D. B., Caricato, M., and Elles, C. G. (2017) Accurate Assignments of Excited-State Resonance Raman Spectra: a Benchmark Study Combining Experiment and Theory. *Journal of Physical Chemistry A 121*, 7937–7946.

[19] Frisch, M. J. et al. Gaussian09 Revision D.01. Gaussian Inc. Wallingford CT 2009.

[20] Long, D. A. *The Raman Effect : a Unified Treatment of the Theory of Raman Scattering by Molecules*; Wiley: Chichester ; New York, 2002; pp xxiv, 597 p.

[21] NIST Computational Chemistry Comparison and Benchmark Database, NIST Standard Reference Database Number 101. 2016; `http://cccbdb.nist.gov/`.

[22] Long, D. A. *The Raman Effect : a Unified Treatment of the Theory of Raman Scattering by Molecules*; Wiley: Chichester ; New York, 2002; pp xxiv, 597 p.

[23] Shin, K. S. K., and Zink, J. I. (1989) Quantitative-Evaluation of the Relationships between Excited-State Geometry and the Intensities of Fundamentals, Overtones, and Combination Bands in Resonance Raman-Spectra. *Inorganic Chemistry 28*, 4358–4366.

[24] B., W. R., and Roald, H. (1969) The Conservation of Orbital Symmetry. *Angewandte Chemie International Edition in English 8*, 781–853.

[25] Garavelli, M., Page, C. S., Celani, P., Olivucci, M., Schmid, W. E., Trushin, S. A., and Fuss, W. (2001) Reaction Path of a sub-200 fs Photochemical Electrocyclic Reaction. *Journal of Physical Chemistry A 105*, 4458–4469.

[26] Vanderlugt, W. T., and Oosterhoff, L. J. (1969) Symmetry Control and Photoinduced Reactions. *Journal of the American Chemical Society 91*, 6042–6049.

[27] Guillaumont, D., Kobayashi, T., Kanda, K., Miyasaka, H., Uchida, K., Kobatake, S., Shibata, K., Nakamura, S., and Irie, M. (2002) An ab Initio MO Study of the Photochromic Reaction of Dithienylethenes. *The Journal of Physical Chemistry A 106*, 7222–7227.

[28] Asano, Y., Murakami, A., Kobayashi, T., Goldberg, A., Guillaumont, D., Yabushita, S., Irie, M., and Nakamura, S. (2004) Theoretical Study on the Photochromic Cycloreversion Reactions of Dithienylethenes; on the Role of the Conical Intersections. *Journal of the American Chemical Society 126*, 12112–12120.

[29] Pontecorvo, E., Ferrante, C., Elles, C. G., and Scopigno, T. (2014) Structural Rearrangement Accompanying the Ultrafast Electrocyclization Reaction of a Photochromic Molecular Switch. *Journal of Physical Chemistry B 118*, 6915–6921.

Chapter 5

Wavelength Dependent Dynamics of Cycloreversion in a Diarylethene-based Photoswitch

5.1 Introduction

Diarylethenes (DAEs) are a class of photochromic molecular switches which reversibly convert between open- and closed-ring isomers with different optical and electronic properties.[1–4] The specific structure of the aryl groups and the ethene bridge dramatically affects the properties and fatigue resistance of the molecule.[1,2,4–6] The switchable electronic and optical properties, as well as the fatigue resistance, have led to the proposed applications of DAEs in molecular electronics, optical data storage, and other optoelectronics.[1,7,8] To effectively take advantage of DAEs in these applications understanding of the reactivity of the system is crucially important. The open-ring isomer of most DAEs photoswitches allow the aryl groups to rotate freely around the bond to the ethene bridge. This rotation results in a distribution of reactive conformers, with aryl groups in an anti-parallel orientation and non-reactive conformers, with aryl groups oriented parallel to each other, in a one-to-one ratio.[6,9]

Commonly, the cyclization reaction for reactive conformers of DAE have between 50 and 100% quantum yield while the non-reactive conformers relax to the ground state.[10,11] However, in some cases, the non-reactive species undergo intersystem crossing to generate a triplet species.[1,5] The addition of the triplet species significantly complicates the studying the spectroscopy of the cyclization reaction as it is long-lived on the timescale of ultrafast measurements. The DAE 1,2-bis(2,4-dimethyl-5-phenyl-3-thienyl)perfluorocyclo-pentene (DMPT-PFCP) shown in figure 5.1

exhibits triplet formation. Earlier work studying the ultrafast evolution of the 2,4-dimethyl-5-phenylthiophene has shown that it also efficiently generates a triplet species in solution.[12] Therefore, considering the wavelength dependence of DMPT-PFCP absorption band, specifically, transitions localized in the cyclopentene bridge provide a promising approach to limit triplet formation and simplify the spectroscopy of the cyclization reaction.

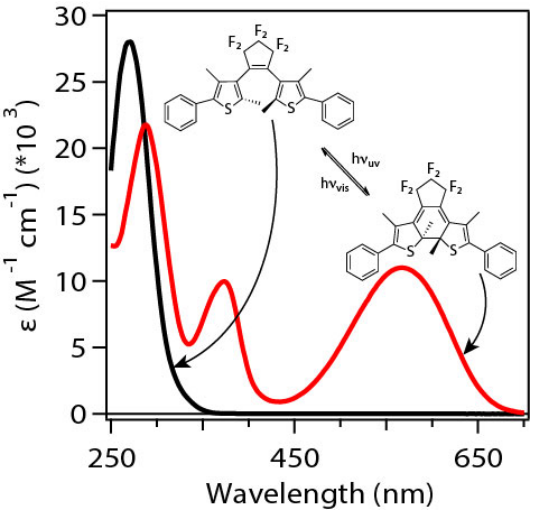

Figure 5.1: DMPT-PFCP Ground State Absorption Spectra
The static absorption spectra for both the open- and closed-ring isomers of DMPT-PFCP. The open-ring isomer is limited to a strong absorption band in the UV region, while the closed-ring isomer displays two additional absorption bands at 410 and 570 nm. The structures of the two isomers are also displayed.

This chapter examines the wavelength dependence of the cyclization reaction of DMPT-PFCP. The transient absorption indicates that the relative population of the long-lived species is dependent on the excitation wavelength. Increasing the energy for excitation promotes the formation of the long-lived species. Also, the similarity in the ps evolution at each excitation wavelength point to the branching taking place on the sub-picosecond timescale.

5.2 Experimental

As described in previous chapters, an amplified Ti:Sapphire laser (Coherent, Legend Elite) with an output of 35 fs pulses at a 1 kHz repetition rate is used to generate pulses with the requisite

characteristics for these experiments. Pump laser wavelengths of 267, 308, and 335 nm are used for the cyclization experiments with powers of 0.3, 0.9 and 1.1 μJ per pulse, respectively. The same detection equipment and parameters are used as described with pump-probe experiments from previous chapters.

The sample solution of 0.5 mM 1,2-bis(2,4-dimethyl-5-phenyl-3-thienyl) perfluoro-cyclopentene (TCI America) (DMPT-PFCP) is prepared in 20 mL of cyclohexane (spectroscopic grade, Fisher). For experiments at 335 nm, the sample concentration was doubled to account for lower absorbance. The sample is then converted to a photostationary state by irradiating the solution using a 310 nm LED for several hours. The sample flowed through a jet nozzle by a mechanical pump to produce a windowless sample volume and recycled into the sample reservoir. The results reported in this chapter are collected with the pump oriented at magic angle relative to the probe polarization. This configuration eliminates changes in the signals due to the re-orientation of the excited molecules and produces an isotropic signal. The same 310 nm LED irradiates the sample reservoir during the measurements to help maintain the photostationary state over several hours of laser excitation. No evidence of photo-degradation was observed.

5.3 Results

The first band in the absorption spectrum of the open form of DMPT-PFCP occurs at 270 nm as shown in figure 5.2. The main chromophore of the species is the dimethyl-phenylthiophene (DMPT) side groups. Comparison of the DMPT absorption spectrum with that of the larger photoswitch shows that most of the electronic transitions are associated with the DMPT side group. Interestingly, the absorption spectrum of DMPT-PFCP does extend further into the visible region with a relatively small amplitude tail.

Time-dependent density functional theory (TD-DFT) calculations of the electronic transitions for DMPT-PFCP performed by our group indicate that this tail is due to a weak electronic transition in the cyclopentane ring. The HOMO and LUMO orbitals which represent this transition are shown in figure 5.3.

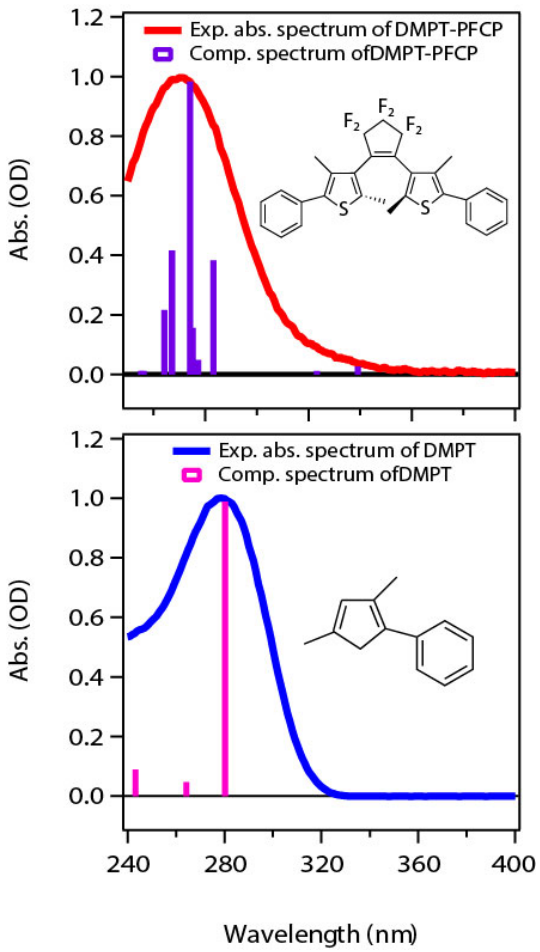

Figure 5.2: The absorption spectra of open-ring DMPT-PFCP and the aryl side group DMPT are shown. The calculated transitions correspond to TD-DFT calculations of the transitions of the DMPT-PFCP open-ring isomer in the reactive conformer and the optimized ground state of DMPT. While the absorption of DMPT-PFCP is comprised of a number of transitions, DMPT is dominated by a single transition. Attention should be drawn to the difference in the tail of the two absorption bands where the lowest energy transition is DMPT-PFCP is observed.

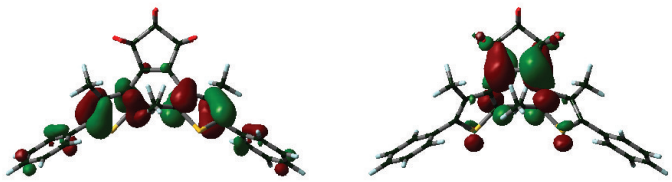

(A) HOMO (B) LUMO

Figure 5.3: The HOMO and LUMO orbitals for DMPT-PFCP illustrate shifting of electron density for the lowest energy transition. The HOMO is distributed across the phenylthiophene groups while the LUMO shifts electron density to the central cyclopentene ring.

The transient absorption spectra following excitation of the open-ring isomer at three different pump wavelengths are presented in figure 5.4. At each excitation wavelength, the spectrum quickly evolves on a fs timescale. For the 335 nm excitation, the spectrum grows in over the first 300 fs and the cross-phase modulation in the solvent provides an upper limit of the instrument response at 75 fs. The transient spectrum for 308 nm excitation shifts and a secondary growth appears on the <1.0 ps timescale. The secondary growth is primarily in the spectral region between 460 and 520 nm. In both the excited-state bands at 605 and 395 nm the peaks begin to blueshift after approximately 200 fs and continue to shift on a several ps timescale. However, this shifting is due to decay of the excited-state species and growth of the ground-state closed-ring isomer. These two species have a difference in their absorption peaks of 35 nm in the visible band and 20 nm in the UV band amounting to 0.08 and 0.17 eV, respectively.

The 266 nm spectrum, which has a comparatively flat excited state absorption, has an isosbestic point at 430 nm. The initial population of the excited-state is impulsive, but a signal grows in that is similar to the secondary growth observed in the 308 nm excitation. The subsequent rise in the 266 nm data is of sufficiently low amplitude and in a narrow range of the spectrum from 460 to 520 nm that global fits of the entire spectrum fail to capture the rise accurately. To capture this ultrafast rise, fits are performed over a narrow range of the spectrum, for the first few picoseconds in both the 266 and 308 nm excitation data. The fit was limited to a range of 460 to 520 nm revealing time constants of 150 $\pm$ 50 and 240 4$\pm$ 40 fs for the 266 nm and 308 nm excitations, respectively.

The data for all three excitations wavelengths have two time constants that are well resolved in this experiment on timescales >1.0 ps. These time constants are found by global analysis using the sum of two exponentials to fit to the data. The first time constant is a 1-3 ps component that represents population transfer from the excited reactive conformer to the closed-ring product. In the case of the 266 and 308 nm excitation, this first time constant is 1.1 $\pm$ 0.5 ps and 1.5 $\pm$ 0.8 ps respectively. The 335 nm excitation has a slightly longer time constant of 3 $\pm$ 1 ps. In all three cases, the excited state absorption near 600 nm shifts on a few ps timescale to 570 nm, matching the peak absorbance of the ground-state visible band. The second time constant is a 27

ps decay component which corresponds to a decay of the excited state absorption and emergence of the long-lived spectral signature, that includes the ground-state closed-ring species. There is no further evolution of the spectrum out to 1 ns after excitation. The excited state bands at each excitation wavelength reach a long-lived state with a lifetime that is not observed in our <1.0 ns experiment.

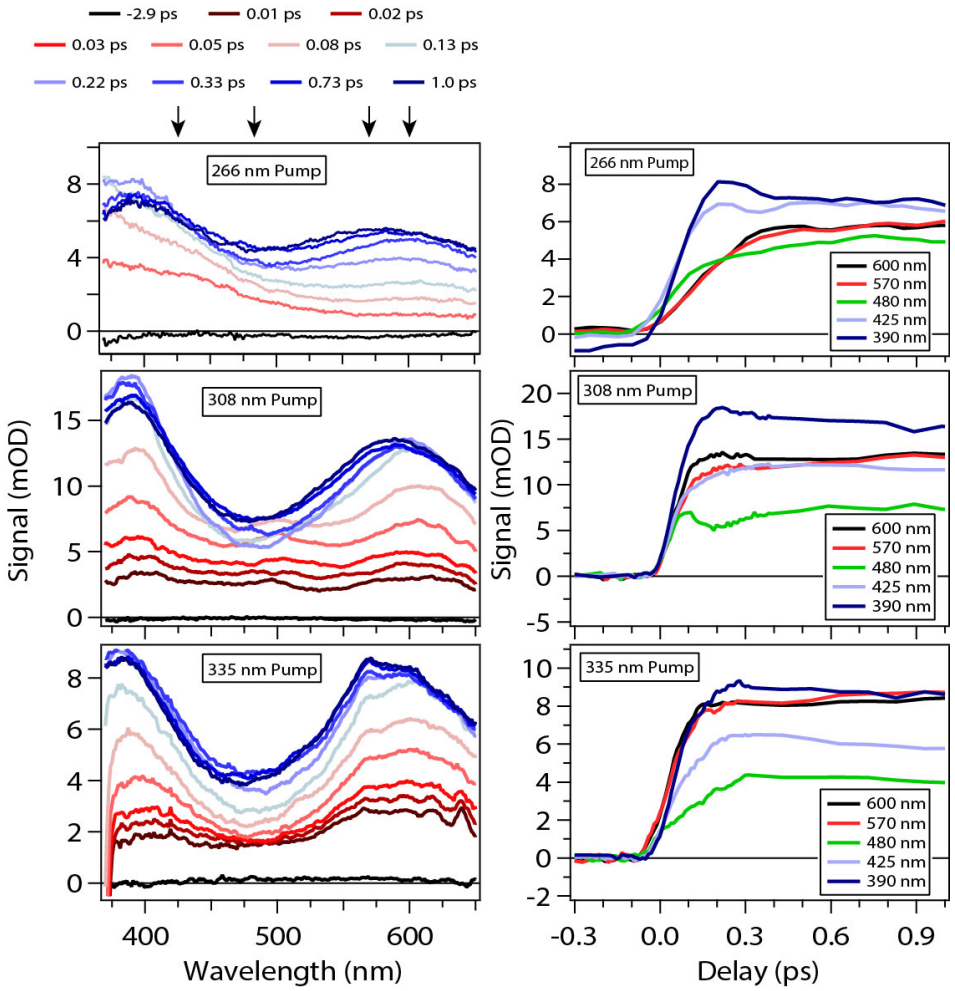

Figure 5.4: The spectra and kinetics of DMPT-PFCP are presented for the three pump wavelengths. The spectra of all three excitations show two major peaks near 600 and 400 nm. The depth of the valley between the peaks varies dramatically with excitation wavelength. The kinetics at several wavelengths are shown. Of particular interest is the slow rise in the red region of the 266 nm spectrum as well as the ultrafast decay at 480 nm in the 308 nm excitation spectrum.

The spectra in figure 5.6 show the transient absorption at two time delays, normalized to the peak of the visible absorption band of the closed-ring species. At long time delays, as shown in

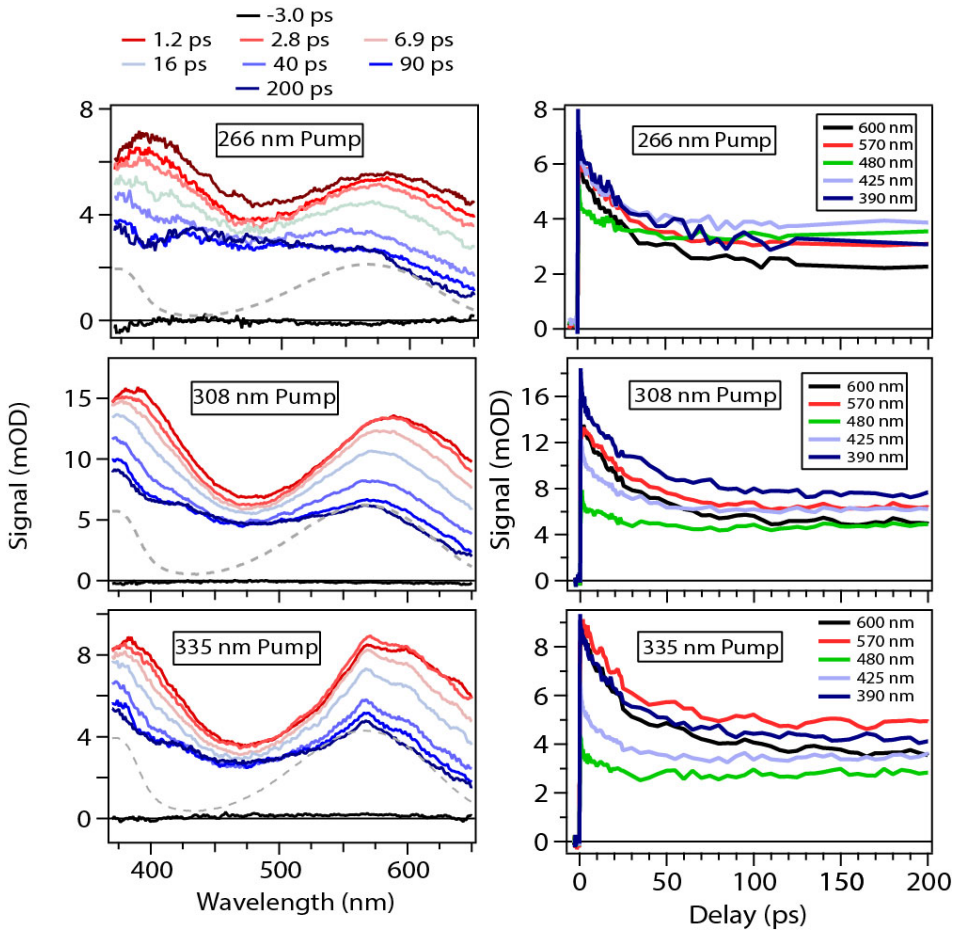

Figure 5.5: The transient absorption spectra and kinetic cuts highlighting the 1 to 200 ps time range. All of the spectra decay on this timescale with some vibrational cooling observed. The dashed line in each set of spectra represents the absorption spectrum of the closed-ring isomer.

figure 5.6B, the remaining transient absorption is attributed to a combination of the newly generated closed form and any non-reactive long-lived species. For comparison, spectra displayed at 5 and 400 ps are displayed. Interestingly, the structure of spectra at both the 5 and 400 ps delay times changes with excitation wavelength. As the excitation wavelength decreases the relative contribution of spectral intensity between 400 and 500 nm increases. This region has low molar absorptivity in the closed-ring product. Using the visible band to approximate the closed-ring contribution indicates that more of the long-lived signal is generated as the excitation shifts to higher energy.

Figure 5.7 shows the normalized spectra at 400 ps with the ground-state absorption subtracted from the transient absorption. By normalizing the spectra to the visible absorption band, we em-

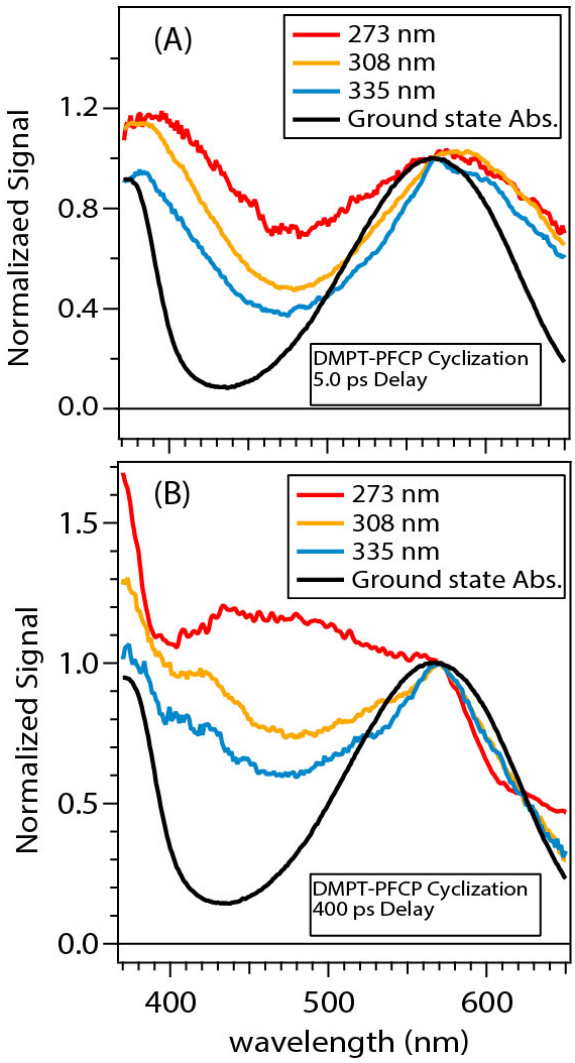

Figure 5.6: The transient absorption spectra at 5 and 400 ps are normalized to the peak of the closed-ring isomer absorption band. The 400 ps spectra represent the long-time limit of the ultrafast experiment where only closed-ring product and long-lived intermediates are present. The five ps spectra represent an intermediate position in the spectral evolution.

phasize the relative contribution of the long-lived signal that cannot be explained by the ground-state absorption of the product. The ground-state spectrum is scaled to prevent negative features in the subtracted spectrum which would not be physically meaningful. The three spectra show very similar structure indicating they originate from the same transient species with varying magnitude corresponding with pump wavelength.

To further examine the ps-scale kinetics, decay associated spectra (DAS) are generated using simultaneous fits across the spectrum while using fixed time constants to minimize the fitting

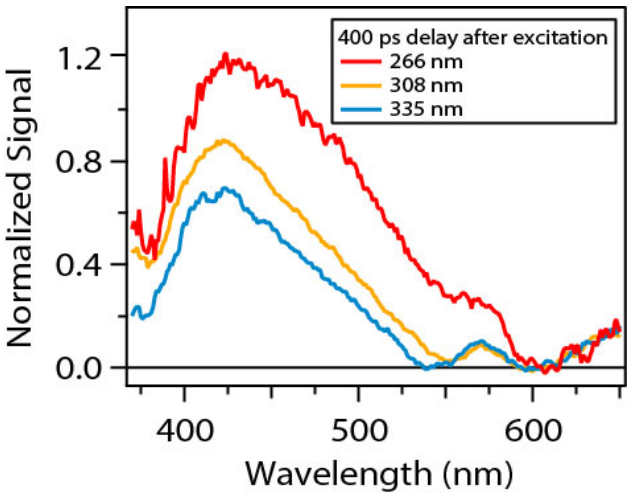

Figure 5.7: The 400 ps spectra from figure 5.6 have the closed-ring product subtracted out to produce the spectra of the long lived intermediate. The closed-ring spectrum was scaled such that there are no negative features due to the subtraction. The intensity of this species increases with increasing pump frequency.

function. The picosecond timescale decay-associated spectra represent the wavelength dependent amplitudes for each decay time constant. The fits to the data from 0.5 to 250 ps are performed with the sum of two exponentials and an offset term. The DAS for each excitation wavelength is presented in figure 5.8. The corresponding short and long decay components show very similar structure, even in the longer three ps decay component of the 335 nm pump spectrum. While there is one consistent negative component centered at 570 nm in the short time of all three spectra, it represents the excited-state population relaxing into the ground-state closed-ring isomer. The component that best represents the difference in the three pump wavelengths is the offset. The similarities of the relative magnitudes of the ps decay components suggest that the spectral differences originate in the femtosecond dynamics.

5.4 Discussion

Previous work by a number of research groups on analogous diarylethene-based photoswitches has described the photo-cyclization process.[10,11,13–16] First, the system experiences rapid state mixing accompanying relaxation out of the Franck-Condon region on a sub-picosecond timescale.

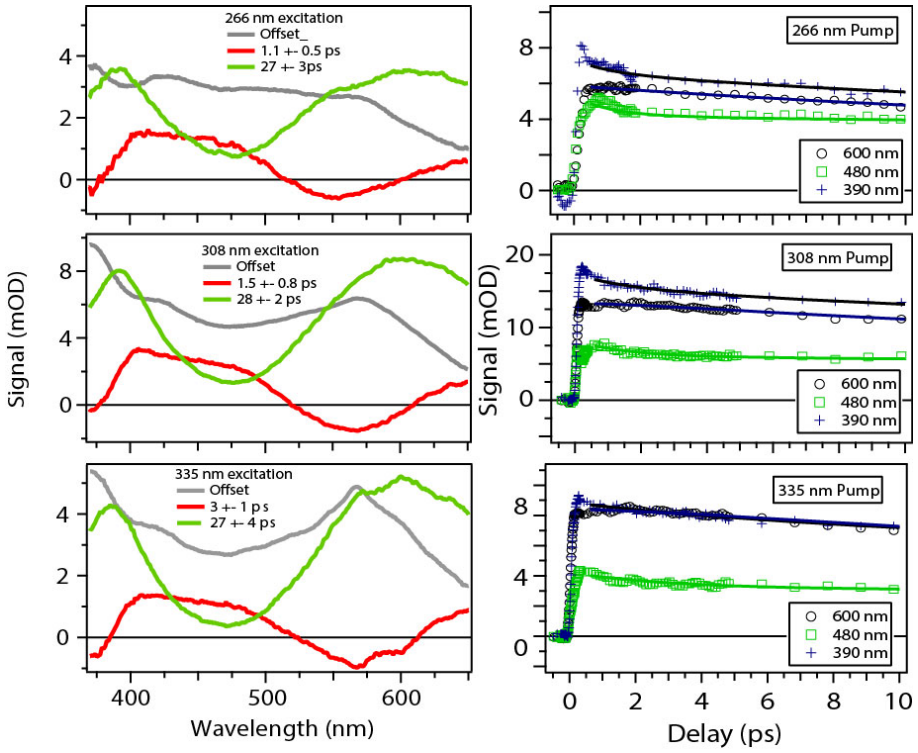

Figure 5.8: The decay-associated spectra for the three excitation wavelengths are shown. Alongside the DAS are several kinetic cuts with data point represented by markers and fits from the DAS overlaid as solid lines. The time constants come from global analysis of each data set. The decay spectra are strikingly similar in structure, but the offset vary significantly indicating that the spectral differences originate in the dynamics prior to the global fits.

Following this initial step, molecules with the appropriate anti-parallel (AP) geometry undergo cyclization to produce the ground-state closed-ring product on a $<$1 picosecond timescale. Finally, the ground-state species cools on a 10s of picoseconds timescale, reproducing the static closed-ring absorption spectrum. While the kinetics are consistent with our results for DMPT-PFCP at 266 nm and 308 nm excitation, the spectroscopy differs in several key ways which we will address below.

In the long time limit, no spectral evolution is observed. One limiting case is that no excited-state species remain and the remaining transient absorption is due to only the open- and closed-ring isomers. Within the spectral range of the experiment, the open-ring isomer has no absorption. However, the remaining transient absorption does not reproduce the ground-state closed-ring absorption spectrum. The ground-state closed-ring species contributes to a portion of the transient signal, but the spectral feature highlighted in figure 5.7 remains. The static spectrum shows that

there is no build-up of the additional absorptive features after extended irradiation and therefore a long-lived excited-state species that decays on a $>$ 1 ns timescale must be responsible. Due to the previously described importance of the DMPT chromophore to the overall DMPT-PFCP absorption spectrum, we can make further connections to the isolated chromophores ultrafast spectroscopy. Specifically, DMPT has been observed to efficiently generate triplet species with an intersystem crossing (ISC) time constant of 21 ps.[12] As such, we assign this additional signal to triplet species of DMPT-PFCP generated by excitation of the non-reactive parallel conformer. Importantly, the assignment of the triplet species implies that the triplet yield is dependent on the excitation wavelength.

Recent work by Hamdi et al. has studied both the microsecond and femtosecond cyclization reaction in DMPT-PFCP.[17] Their work proposes a set of competitive channels in the reactive conformer as the system relaxes out of the Franck-Condon region. These channels are described as either the immediate cyclization or the formation of a triplet species from the AP conformer on the fs time scale. As Hamdi et al. point out, this branching is challenging to resolve because the transient absorption for the parallel and AP species are identical, significantly complicating any global or target analysis. However, the proposed branching channels involve either the formation of the closed-ring species or vibrational cooling leading to ISC. The general model for this process is presented in scheme 1.

Our data point to the triplet species forming on a sub-picosecond timescale in addition to displaying a wavelength dependent branching. The spectra shown in figure 5.7 match the triplet species reported by Hamdi et al..[17] The calculations presented in figure 5.2 show that multiple states contribute to the first absorption band of the open-ring isomer. When exciting with higher energy into the open-ring absorption band, the transition is to a state above S_1. As the species relaxes out of the initial Franck-Condon region and undergoes internal conversion to S_1, the excess energy from the transition converts into vibrational energy in the molecule. Therefore, exciting with higher energy can change the trajectory of the system out of the Franck-Condon region, leading to changes in the branching ratio between the closed-ring species and the AP triplet species.

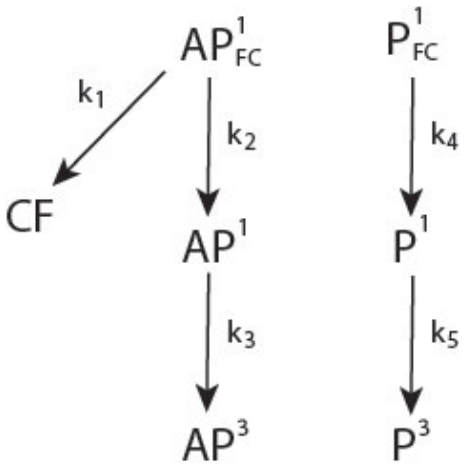

Figure 5.9: The kinetic model for the excitation of the open-ring isomer of DMPT-PFCP includes two independent pathways due to the difference in reactivity of the two conformers. The parallel form (P) relaxes out of the Franck-Condon region (FC) and undergoes ISC. The anti-parallel (AP)conformer branches out of the FC region forming an AP species which quickly undergoes ISC and the closed-ring product.

This result is consistent with the work of Hamdi et al., but no wavelength dependence was performed in their study.[17]

It is important to consider that the results highlighted by the triplet spectra in figure 5.7 show the contribution of the triplet species relative to the normalized closed-ring product. Therefore we must consider that the increase in excitation energy could decrease the formation of the closed-ring product.

One means of decreasing the formation of the closed-ring product is by proposing that the excited reactive conformer would need to have access to an additional pathway to generate triplet species. This would leave any ultrafast branching between the product and triplet unchanged, but produce relatively more triplet species in the long-time limit. Due to the similarities in spectroscopy between the reactive and non-reactive conformers, guiding the AP conformer to a non-reactive channel would increase the intensity of the spectral features of the parallel non-reactive conformer. However, careful consideration of the 27 ps DAS component, can provide insight into this potential mechanism. Specifically, the relative magnitude 605 nm band in the DAS should increase with the population of any non-reactive species. In other words, the magnitude of the decay at 605 should increase with excitation energy. The observed behavior is actually the relative

decrease of the 605 nm band indicating that this relaxation path is inconsistent with the data.

5.5 Conclusions

The wavelength dependent excitation of DMPT-PFCP has shown that relative yield for ISC increases with increasing excitation energy. The behavior of the kinetics and global analysis point to the difference being related to the sub-picosecond dynamics as the molecule relaxes out of the Franck-Condon region. By exciting the system to singlet states just above S_1 the trajectory of the system out of the Franck-Condon region changes, impacting the branching between ultrafast triplet formation and closed-ring product formation. This is consistent with a fast branching of the reactive conformer to generate both closed-ring product and triplet intermediate. Furthermore, it is unlikely that another deactivation pathway for the anti-parallel species is responsible for the excitation-dependent behavior as indicated by the careful consideration of the DAS and the long-time offset.

5.6 Bibliography

[1] Irie, M. (2000) Diarylethenes For Memories and Switches. *Chemical Reviews 100*, 1685–1716.

[2] Irie, M., and Mohri, M. (1988) Thermally Irreversible Photochromic Systems - Reversible Photocyclization of Diarylethene Derivatives. *Journal of Organic Chemistry 53*, 803–808.

[3] Terao, F., Morimoto, M., and Irie, M. (2012) Light-Driven Molecular-Crystal Actuators: Rapid and Reversible Bending of Rodlike Mixed Crystals of Diarylethene Derivatives. *Angew Chem Int Ed Engl 51*, 901–904.

[4] Irie, M., Fukaminato, T., Matsuda, K., and Kobatake, S. (2014) Photochromism of Diarylethene Molecules and Crystals: Memories, Switches, and Actuators. *Chem Rev 114*, 12174–277.

[5] Herder, M., Schmidt, B. M., Grubert, L., Patzel, M., Schwarz, J., and Hecht, S. (2015) Improving the Fatigue Resistance of Diarylethene Switches. *Journal of the American Chemical Society 137*, 2738–2747.

[6] Irie, M., Sakemura, K., Okinaka, M., and Uchida, K. (1995) Photochromism of Dithienylethenes with Electron-Donating Substituents. *Journal of Organic Chemistry 60*, 8305–8309.

[7] Cox, J. M., Walton, I. M., Patel, D. G., Xu, M. Y., Chen, Y. S., and Benedict, J. B. (2015) The Temperature Dependent Photoswitching of a Classic Diarylethene Monitored by in Situ X-ray Diffraction. *Journal of Physical Chemistry A 119*, 884–888.

[8] Joachim, C., Gimzewski, J. K., and Aviram, A. (2000) Electronics Using Hybrid-Molecular and Mono-Molecular Devices. *Nature 408*, 541–548.

[9] Uchida, K., Tsuchida, E., Aoi, Y., Nakamura, S., and Irie, M. (1999) Substitution Effect on

the Coloration Quantum Yield of a Photochromic Bisbenzothienylethene. *Chemistry Letters* 63–64.

[10] Hania, P. R., Telesca, R., Lucas, L. N., Pugzlys, A., van Esch, J., Feringa, B. L., Snijders, J. G., and Duppen, K. (2002) An Optical and Theoretical Investigation of the Ultrafast Dynamics of a Bisthienylethene-Based Photochromic Switch. *Journal of Physical Chemistry A 106*, 8498–8507.

[11] Hania, P. R., Pugzlys, A., Lucas, L. N., de Jong, J. J. D., Feringa, B. L., van Esch, J. H., Jonkman, H. T., and Duppen, K. (2005) Ring Closure Dynamics of BTE-Based Photochromic Switches: Perfluoro- Versus Perhydrocyclopentene Derivatives. *Journal of Physical Chemistry A 109*, 9437–9442.

[12] Zheldakov, I. L., Wasylenko, J. M., and Elles, C. G. (2012) Excited-State Dynamics and Efficient Triplet Formation in Phenylthiophene Compounds. *Physical Chemistry Chemical Physics 14*, 6211–6218.

[13] Ishibashi, Y., Umesato, T., Kobatake, S., Irie, M., and Miyasaka, H. (2012) Femtosecond Laser Photolysis Studies on Temperature Dependence of Cyclization and Cycloreversion Reactions of a Photochromic Diarylethene Derivative. *Journal of Physical Chemistry C 116*, 4862–4869.

[14] Miyasaka, H., Murakami, M., Okada, T., Nagata, Y., Itaya, A., Kobatake, S., and Irie, M. (2003) Picosecond and Femtosecond Laser Photolysis Studies of a Photochromic Diarylethene Derivative: Multiphoton Gated Reaction. *Chemical Physics Letters 371*, 40–48.

[15] Ward, C. L., and Elles, C. G. (2014) Cycloreversion Dynamics of a Photochromic Molecular Switch via One-Photon and Sequential Two-Photon Excitation. *The Journal of Physical Chemistry A 118*, 10011–10019.

[16] Pontecorvo, E., Ferrante, C., Elles, C. G., and Scopigno, T. (2014) Structural Rearrange-

ment Accompanying the Ultrafast Electrocyclization Reaction of a Photochromic Molecular Switch. *Journal of Physical Chemistry B 118*, 6915–6921.

[17] Hamdi, I., Buntinx, G., Perrier, A., Devos, O., Jaïdane, N., Delbaere, S., Tiwari, A. K., Dubois, J., Takeshita, M., Wada, Y., and Aloïse, S. (2016) New Insights Into the Photoswitching Mechanisms of Normal Dithienylethenes. *Physical Chemistry Chemical Physics 18*, 28091–28100.

Chapter 6

Photoswitching in Diverse Diarylethene Derivatives

6.1 Introduction

Diarylethene-based photoswitches (DAEs) are an interesting class of molecules which reversibly isomerize when exposed to UV or visible light. Accompanying the isomerization, the chemical and electronic properties of the molecules change. This switchable behavior has led to many proposed applications in optical data storage, optoelectronics, and activated materials.[1–6] While a number of different model systems have been carefully studied to represent the general behavior of DAEs, the functional substitutions required for certain applications can significantly affect the switching behavior.[2,3,5,7–13]

Two DAEs studied in this chapter provide an interesting means to study the effects of substitution on the switching dynamics. The first DAE structure uses a modified ethene bridge to act as a metal linker incorporated into metal-organic frameworks (MOFs). Currently, MOFs are employed in gas separation and storage, especially hydrogen gas, due to the ability of gasses to adsorb into the crystal structure.[14,15] With the inclusion of DAEs in the organic linkers of MOFs, the properties of the MOFs crystals can be actively controlled. To understand the advantages and potential pitfalls of this specific substitution, ultrafast studies are performed on 9,10-bis(2,5-dimethylthiophen-3-yl)-phenanthrene-2,7-dicarboxylate (TPDC) in which the ethene bridge is fused with a phenanthrene structure. The second structure aims to eliminate a problem that has complicated the study of DAEs since their discovery. In solution, DAEs exist as a distribution of conformers which can be either reactive or non-reactive based on the orientation of the two aryl groups.[3,7,9] Importantly, the reactive and non-reactive species evolve along different mechanistic pathways.[3] A DAE, 4,4'-(1-methyl-

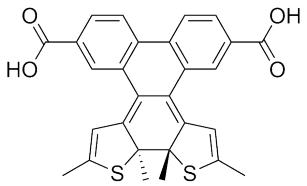

Figure 6.1: The structure of TPDC showing the phenanthrene structure fused with the ethene bridge of the diarylethene.

1H-indole-2,3-diyl)bis(5-methyl-2-phenylthiazole) (DTA), provides a set of weak intramolecular hydrogen bonds which preferentially leave the molecule in a reactive conformer.[8,16] Using ultrafast spectroscopy to study the transient absorption of DTA largely eliminates the complication of the non-reactive conformer clarifying the contributions to the spectral evolution.

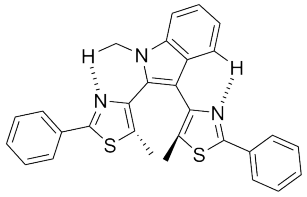

Figure 6.2: The structure of DTA showing the weak hydrogen bonds between the thiazole aryl groups and the methylindole group fused with the ethene bridge.

6.2 Experimental

For this work, an amplified Ti:Sapphire laser (Coherent, Legend Elite) with an output of 35 fs pulses at a 1 kHz repetition rate is used to generate laser pulses at the necessary wavelengths. For a more detailed discussion of the experimental considerations consult Chapter 2 of this dissertation. A pump laser wavelength of 308 nm is used for the cyclization experiments, and 500 nm is used for the cycloreversion measurements. (1.9 μJ 308, 10 μJ 500) The same detection equipment and parameters are used as described with pump-probe experiments from previous chapters. The pulse duration is estimated by the FWHM of the solvent cross-correlation signal. The 308 nm experiments have an estimated FWHM of 70 fs, and the 500 nm experiment has an estimated FWHM of 80 fs.

A sample solution of 3.0 mM 9,10-bis(2,5-dimethylthiophen-3-yl)- phenanthrene-2,7-dicarboxylate

(TPDC)[1] is prepared in 25 mL of DMSO (ACS Grade, Fisher). The TPDC material was provided by Dr. Jason Benedict from the University of Buffalo. For the cycloreversion reaction experiments, the prepared sample is then converted to a photostationary state by irradiating the solution using a 310 nm LED for several hours. The same 310 nm LED irradiates the sample reservoir during the measurements to help maintain the photostationary state over several hours of laser excitation. No evidence of sample degradation is observed via UV-vis. Experiments studying the cyclization reaction of TPDC, a White-light LED with a 420 nm long pass glass filter is used to irradiate the sample and prevent build up of the closed form species.

The sample solution of 0.05 mM 4,4'-(1-methyl-1H-indole-2,3-diyl)bis(5-methyl-2-phenyl-thiazole) (DTA)[8] is prepared in 25 mL of cyclohexane (spectroscopic grade, Fisher). The DTA photoswitch was provided by Dr. Takuya Nakashima from the Nara Institute of Science and Technology. A White-light LED with a 462 nm long pass glass filter is used to irradiate the sample and prevent build up of the closed form species. The sample flows through a flow cell with a 0.5 mm pathlength and recycles back into the sample reservoir.

6.3 Results and Discussion

6.3.1 TPDC Dynamics

As with all diarylethene-based photoswitches, the cyclization of TPDC produces an additional absorption band in the visible region. The UV-vis spectra for both isomers is shown in figure 6.3 The strong absorption band in UV region below 300 nm corresponds to the absorption of the phenanthrene moiety fused to the ethene bridge.

6.3.1.1 TPDC Cycloreversion

The transient absorption of the cycloreversion reaction is performed using a 500 nm pump pulse and is shown in 6.4. A portion of the spectrum is omitted due to the scattering from the 500 nm pump pulse used to photo-excite the sample. The transient absorption peaks at 40 nm and shifts

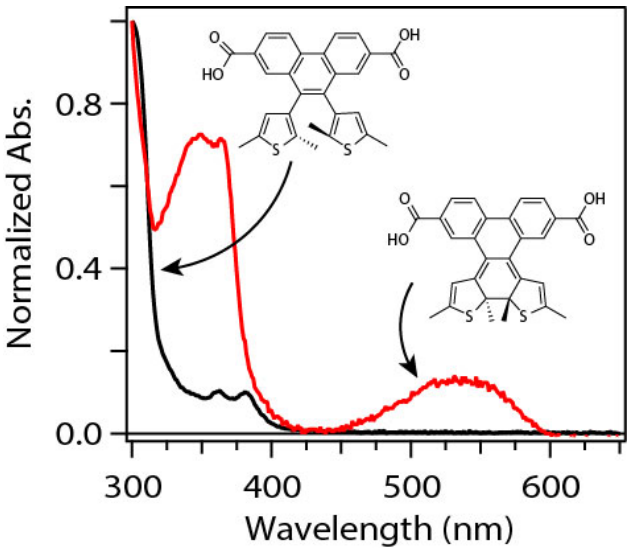

Figure 6.3: The open-ring isomer of TPDC (in black) reaches the absorbance baseline at approximately 450 nm. The closed-ring isomer shows similar UV absorption structure but with larger relative intensity, in additional to the visible band that peaks at 435 nm.

slightly to 455 nm and increases in intensity over the first few ps. The broad feature near 600 nm grows in slightly over this same few ps timescale. In addition, there is a negative feature near 350 nm with corresponds to a ground-state bleach. An isosbestic point is also observed at 375 nm between the excited-state absorption and the ground-state bleach. The ground-state bleach also contributes to the transient signal between 500 and 575 nm, but the scattering from the excitation pulse obscures most of this range. After the initial shifting, the spectrum decays back to near the baseline.

The kinetics of the excited-state absorption decay are shown in figure 6.5. Traces at 450 and 625 nm show bi-exponential decay with time constants of 3.8 and 104 ps before returning to the baseline. The kinetics of the 360 nm region show only single exponential decay with the 104 ps time constant for the recovery of the ground-state bleach caused by the second absorption band. Importantly, the bleach in this spectral region does not completely recover. The long-time bleach signal in this region is small (<1.0 mOD) indicating some cycloreversion taking place.

The decay-associated spectra (DAS) are displayed in figure 6.6 revealing two time constants across the spectrum. The DAS display the amplitude for the time constants as a function of wavelength and are fit between 0.2 and 500 ps. The first time constant of 3.8 ps is responsible for the

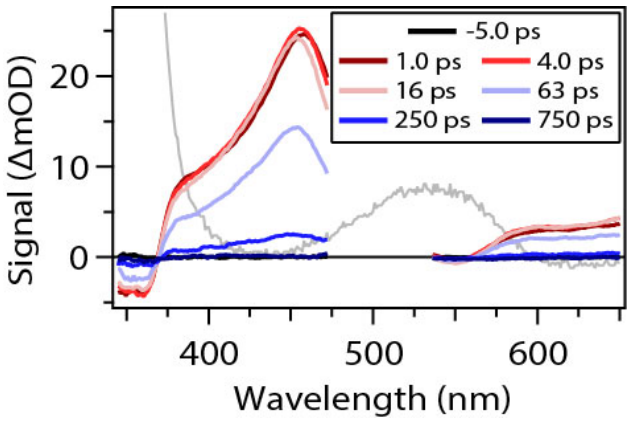

Figure 6.4: The transient absorption spectra of TPDC showing several time delays. The spectrum cools over the first few picoseconds followed by decay to the baseline. The ground-state bleach below 375 nm recovers nearly to the baseline but retains a small persistent bleach at long time delays. This persistent bleach is not observed in the bleach of the ground-state visible absorption band, likely due to the relatively small amplitude of the transition and the noise of the measurement.

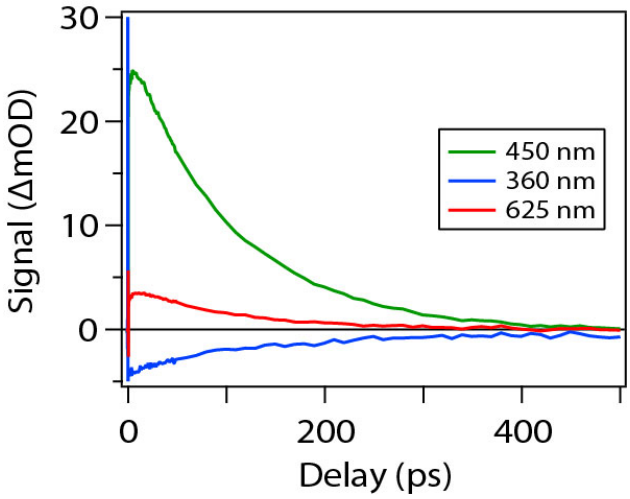

Figure 6.5: The kinetic traces of three wavelengths show the 3.8 ps growth component followed by the much longer 104 ps decay. The 360 nm kinetics are well represented by the single 104 ps decay component and shows a minor offset at long time delays. The offset indicates the formation of some open-ring product.

shifting and slight growth of the primary 460 nm band as well as the increase in the 600 nm region. With a 104 ps time constant the entire spectrum decays to the baseline in all regions except in the UV-bleach already mentioned.

The cycloreversion shows extended timescales relative to other smaller or model DAEs.[3,4,17,18] The 3.8 ps timescale represents the cooling of the excited-state species. The isosbestic point at 375

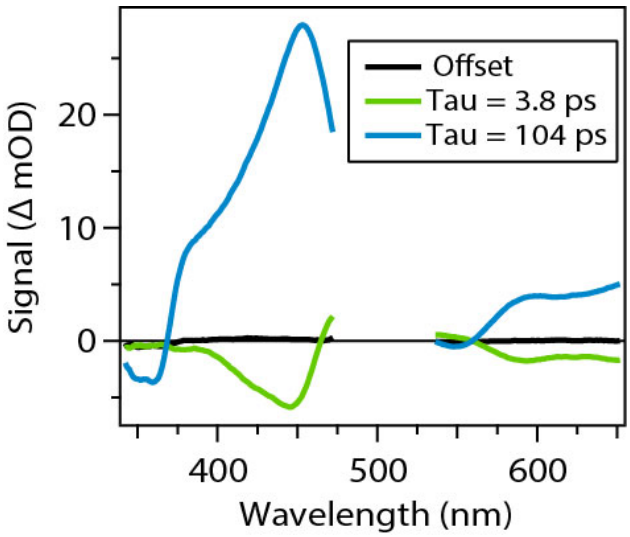

Figure 6.6: The DAS for the bi-exponential fits show a consistent growth in the 3.8 ps timescale and decay of the remaining transient absorption with the 104 ps time constant. The steep slope of the DAS near the obscured region around 500 indicates the amplitude of the DAS may be positive in this region

nm also indicates that the excited-state species decays directly back to the ground state. This leads to a description of the relaxation process as a sequential kinetic model with branching at the product formation that significantly favors the return to the closed form.

6.3.1.2 TPDC Cyclization

The transient spectra for the cyclization of TPDC is shown in figure 6.7. Interestingly, TPDC displays no evident dynamics on the sub-picosecond time scale and relatively low amplitude evolution overall. The spectrum within the probe window is mostly featureless immediately following excitation, but a shoulder grows in over the first few ps. A second overall spectral decay is then observed on a 10s of ps timescale. Importantly, the minimum of the transient absorption spectrum corresponds to the maximum of the ground-state closed-ring isomer (grey) in the visible region. Additionally, the strong ground-state absorptive feature at 370 nm points to an even small possible contribution from any closed-ring product formed on this timescale. This comparison indicates that on the picosecond timescale the closed-ring isomer is a relatively minor product if it forms at all.

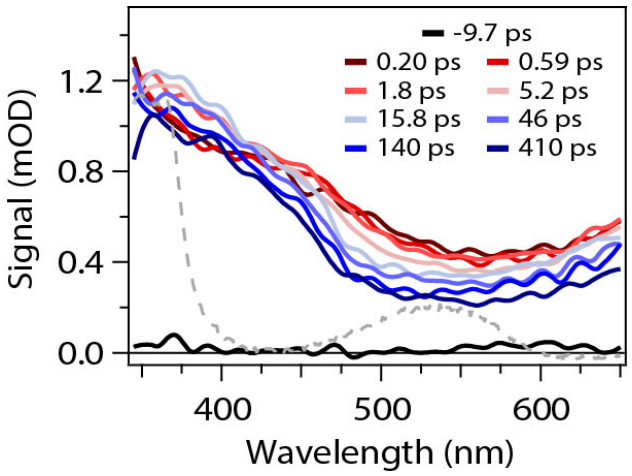

Figure 6.7: The transient spectra for the cyclization of TPDC at a number of delay times is shown. The spectra are initially broad and featureless with a set of peaks appearing between 350 and 450 nm after the first few picoseconds. The spectrum the slowly decays in a generally uniform manner. The dashed grey line corresponds to the UV-vis absorption spectrum of the closed-ring isomer.

The kinetics in figure 6.8 highlight the slight growth in the 405 nm trace with a 3.9 ps time constant and the small overall decay of the spectrum 76 ps time constant. The inset shows the kinetics at select wavelengths over the first few ps, to highlight the short time evolution of the spectrum.

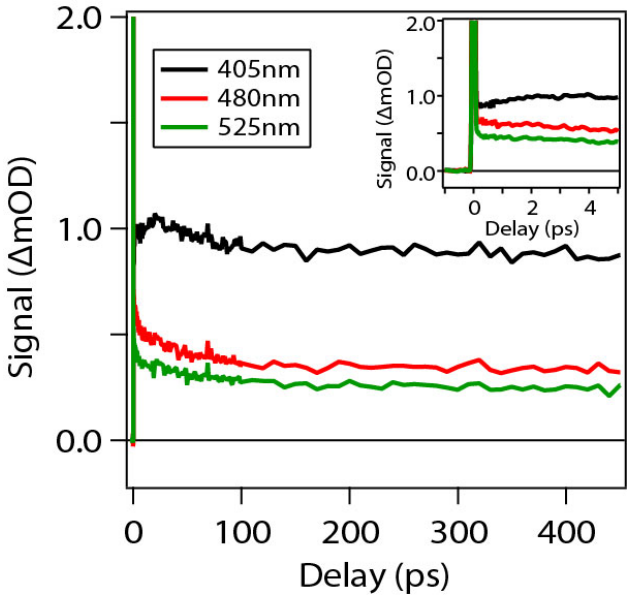

Figure 6.8: Kinetics cuts of three wavelengths are shown. The 405 nm trace highlights the ps rise while the 480 and 525 nm traces show monotonic decay. The inset is provided to emphasized the unique lack of spectral evolution on the $\leq$1 ps timescale

The DAS for the cyclization reaction, shown in figure 6.9, highlight the large offset remaining after the decay processes are complete. The large amplitude of the offset relative to the DAS also suggests that a limited fraction of the excited species contribute to the evolution of the transient spectrum. The shorter time constant displays a negative feature centered at 380 nm which is due to the rise in the transient absorption signal. Similar to the cyclization reaction, this 3.9 ps time constant is due to cooling of the broad absorption band below 500 nm. The 380 nm feature corresponds to the first absorption band of the open-ring isomer. The longer decay component has a time constant of 76 ps which has a double-peaked structure that peaks at 380 and 460 nm.

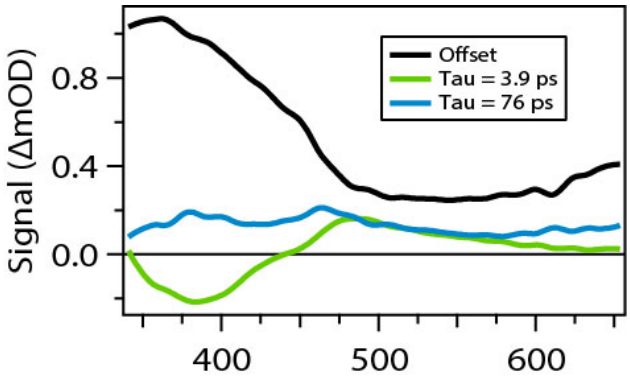

Figure 6.9: DAS of the TPDC cyclization reaction. The 3.9 ps spectrum shows the cooling of the excited- state species for the absorption band below 500 nm. The longer 76 ps DAS represents a decay of the entire spectrum with slightly larger amplitudes at 380 and 460 nm.

The lack of observable sub-picosecond evolution and the relatively low contribution that any closed-ring species can provide points to a lack of the fs cyclization mechanism in TPDC as discussed in Chapter 4. The peak that grows in at 380 nm on the 3.9 ps timescale is consistent with the second absorption band of the closed form. However, the relatively low amplitude of the spectral evolution suggest that the cyclization occurs on a much longer timescale. Potentially, the aromaticity of the phenanthrene fused to the ethene bridge creates a barrier to the reaction, even on the excited-state. To perform the cyclization reaction, the aromatic ethene bridge must break that aromaticity to generate the new cyclohexadiene moiety. This barrier would reduce the rate of closed-ring isomer formation by many orders of magnitude relative to the essentially barrier-less reactivity displayed in other DAEs.

6.3.2 DTA Cyclization Dynamics

The static absorption of DTA is shown in figure 6.10. The spectra display the characteristic strong UV absorption band in the open-ring isomer and the new visible absorption band for the closed-ring isomer. Additionally, a low amplitude tail is present in the open-ring isomer absorption spectrum which extends to approximately 450 nm.

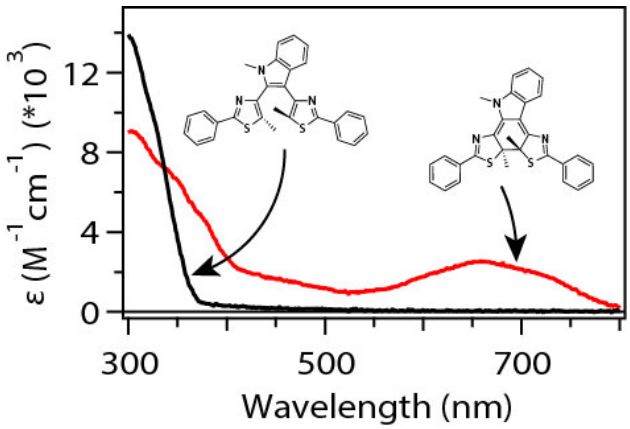

Figure 6.10: The UV-vis absorption of DTA for both the open- and closed-ring isomers. The first absorption band for the close-ring isomer peaks in the visible region at 660 nm. The open-ring isomer absorbs mainly in the UV, but has a weak tail the extends out to approximately 450 nm.

In figure 6.11 the ultrafast evolution of the spectrum is displayed with 10 fs intervals out to 200 ps. A section of the spectrum near 560 nm is omitted due to excessive 2nd order scattering of the pump pulse in the imaging spectrograph. The spectra have two growth components, highlighted by the verticle arrows over this 200 fs timescale. The first timescale represents the instrument limited rise of roughly 70 fs. The second timescale is isolated to the 475 to 550 nm range and represents a new absorption feature.

After the initial rise over the first 200 fs, figure 6.12 shows the absorption bands near 400 and 500 nm decay while the absorption above 650 nm grows in slightly. The evolution of the spectrum is complete by 2 ps. It is also worth noting that, although scattering prevents directly observing the spectrum between 540 and 580, the structure on either side of this range is consistent with an isosbestic point at roughly 560.

In figure 6.13 the kinetics at several key wavelengths including the blue edge of the spectral

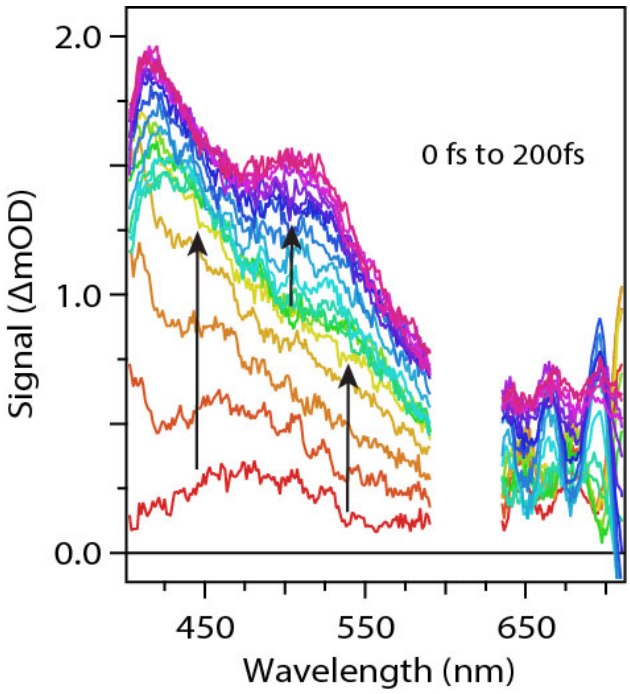

Figure 6.11: The spectra from 0 to 200 fs are plotted in 10 fs steps. The spectrum displays one distinct rises within and narrow rise neat 460 nm in addition to rise due to the instrument limited responce of the system.

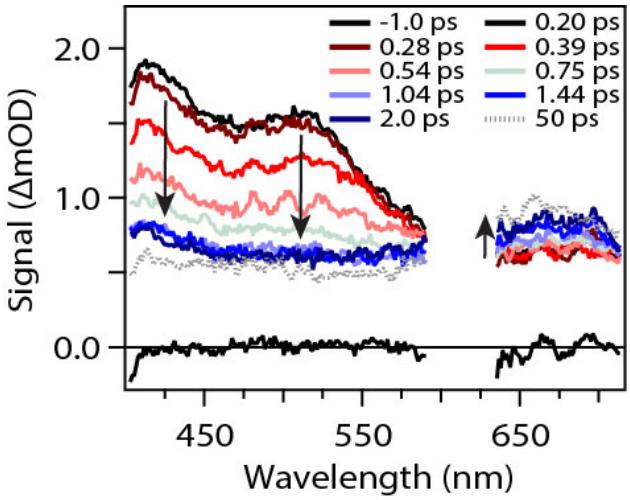

Figure 6.12: The transient spectrum after 0.2 to 2 ps is show at various time delays to demonstrate the evolution of the spectrum. The spectrum at 50 ps is also show to demonstrate lack of change between it and the 2 ps spectrum. In this 2 ps window the transient absorption below 550 nm decays while the spectrum above 550 grows in slightly.

range which represents the strongest transient absorption amplitude, the red side of the spectrum where no decay components are evident, and 525 nm where the absorption band grows in im-

mediately following excitation. The solid lines are fits based on the global analysis of the data using three time constants. The instrument response as approximated by the cross-phase modulation in the solvent is 70 fs. For this reason, the global fits were started at a delay of 80 fs. The initial growth occurs with a time constant of 100 $\pm$ 10 fs followed by decay with a 310 $\pm$ 40 fs time constant. The last exponential component is a 5.4 ps with small amplitude across the entire spectrum.

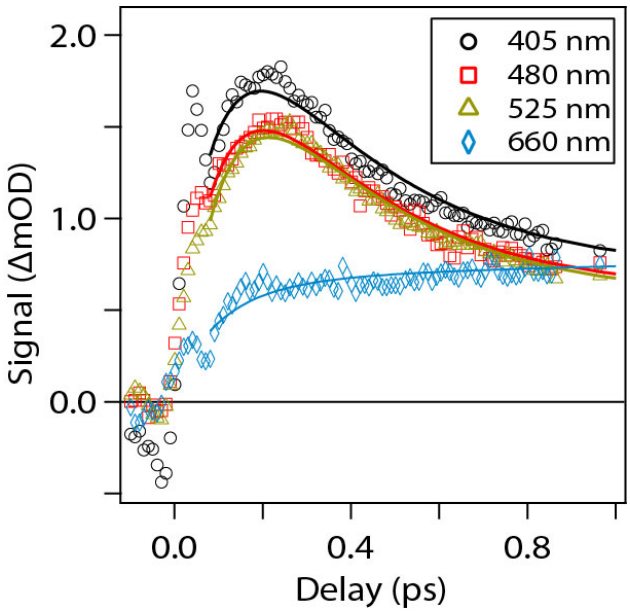

Figure 6.13: Traces at four wavelengths show the kinetics of DTA. The solid line represent the results of the global fit using the sum of three exponentials. The fits begin at 80 fs to avoid the instrument response.

The DAS for the three exponential fit is displayed in figure 6.14. The structure of the DAS for the 0.1 and 0.3 ps time constants are near mirror images while the long-time limit of the transient absorption matches the absorption spectrum of the closed-ring isomer.

In the long-time limit, we can take the remaining transient absorption signal and compare it to the static UV-vis absorption to approximate the contribution of any other potential long-lived species. In figure 6.15 the 80 ps delay of DTA is overlaid with the scaled UV-vis absorption. The two spectra show excellent agreement except for the edge near the UV. However, the ground-state absorption of the DTA open-ring isomer has some absorption in this range, and the difference can be attributed to this ground-state bleach.

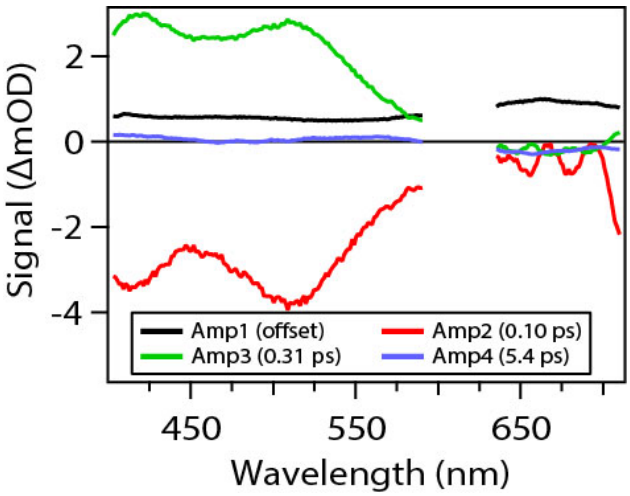

Figure 6.14: The DAS is extracted from the global analysis of the spectrum using a sum of three exponentials and an offset term. The portion of the

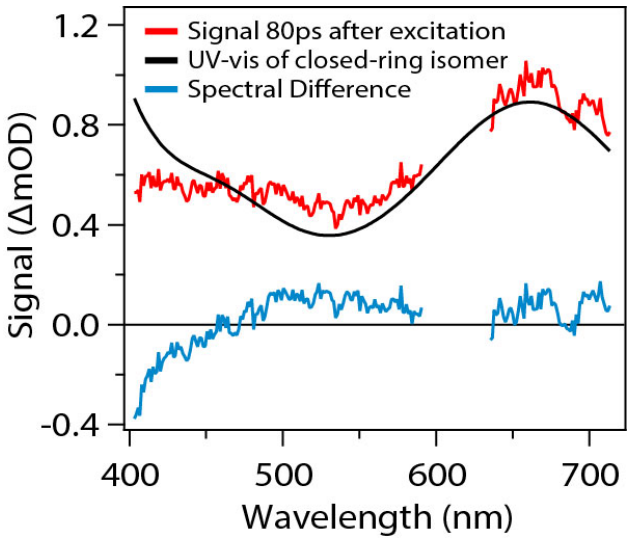

Figure 6.15

Of fundamental interest in the evolution of this spectrum is the low amplitude of any change on the >1 ps timescale. The lack of a significant >1 ps component points to the system being dominated the reactive conformer and that there is nearly complete conversion to the closed-ring product. While the 5.4 ps time constant is consistent with internal conversion of the non-reactive conformers in DAEs with analogous phenylthiophene based aryl groups,[3,4,17,18] it shows a negative amplitude above 650 nm, which is inconsistent with the relaxation an excited-state species to the ground state. One potential explanation is that a small population of non-reactive conformer is

present and the 5.2 ps component represents the time for the aryl-groups to reorient into the reactive conformer.

6.4 Conclusions

We have presented the reaction dynamics for two specialized DAEs, which have been designed with particular properties in mind. TPDC, as a component in MOFs, displays, at best, limited efficiency in the cyclization and cycloreversion reactions on the timescale of our experiments. In the cyclization reaction, the long-lived excited-state species may undergo additional evolution on nano- or microsecond timescale. The cycloreversion reaction has clear bi-exponential decay, but only produce the open-ring isomer as a minor product. Ultimately the phenanthrene group, incorporated as part of the ethene bridge, lengthens the timescales that the system evolves on. On the other hand, DTA shows tri-exponential decay with a complete production of closed-form product from the excited molecules. Not only does the added intramolecular hydrogen bonding effectively eliminate the contributions of the non-reactive conformer, but it also accelerates the rate of reaction compared to a system like DMPT-PFCP (see Chapter 5). These two systems provide an interesting range of behaviors form DAEs and demonstrate the complexity of the relationship between switching dynamics and structure.

6.5 Bibliography

[1] Patel, D. G., Walton, I. M., Cox, J. M., Gleason, C. J., Butzer, D. R., and Benedict, J. B. (2014) Photoresponsive Porous Materials: the Design and Synthesis of Photochromic Diarylethene-Based Linkers and a Metal-Organic Framework. *Chemical Communications 50*, 2653–2656.

[2] Walton, I. M., Cox, J. M., Coppin, J. A., Linderman, C. M., Patel, D. G., and Benedict, J. B. (2013) Photo-Responsive MOFs: Light-Induced Switching of Porous Single Crystals Containing a Photochromic Diarylethene. *Chemical Communications 49*, 8012–8014.

[3] Irie, M. (2000) Diarylethenes For Memories and Switches. *Chemical Reviews 100*, 1685–1716.

[4] Tani, K., Ishibashi, Y., Miyasaka, H., Kobatake, S., and Irie, M. (2008) Dynamics of Cyclization, Cycloreversion, and Multiphoton-Gated Reaction of a Photochromic Diarylethene Derivative in Crystalline Phase. *Journal of Physical Chemistry C 112*, 11150–11157.

[5] Irie, M., Fukaminato, T., Matsuda, K., and Kobatake, S. (2014) Photochromism of Diarylethene Molecules and Crystals: Memories, Switches, and Actuators. *Chem Rev 114*, 12174–277.

[6] Parthenopoulos, D. A., and Rentzepis, P. M. (1989) 3-Dimensional Optical Storage Memory. *Science 245*, 843–845.

[7] Matsuda, K., and Irie, M. (2004) Diarylethene As a Photo Switching Unit. *Journal of Photochemistry and Photobiology C-Photochemistry Reviews 5*, 169–182.

[8] Fukumoto, S., Nakashima, T., and Kawai, T. (2011) Intramolecular Hydrogen Bonding in a Triangular Dithiazolyl-Azaindole for Efficient Photoreactivity in Polar and Nonpolar Solvents. *European Journal of Organic Chemistry* 5047–5053.

[9] Irie, M., and Mohri, M. (1988) Thermally Irreversible Photochromic Systems - Reversible Photocyclization of Diarylethene Derivatives. *Journal of Organic Chemistry 53*, 803–808.

[10] Miyasaka, H., Murakami, M., Okada, T., Nagata, Y., Itaya, A., Kobatake, S., and Irie, M. (2003) Picosecond and Femtosecond Laser Photolysis Studies of a Photochromic Diarylethene Derivative: Multiphoton Gated Reaction. *Chemical Physics Letters 371*, 40–48.

[11] Ishibashi, Y., Okuno, K., Ota, C., Umesato, T., Katayama, T., Murakami, M., Kobatake, S., Irie, M., and Miyasaka, H. (2010) Multiphoton-Gated Cycloreversion Reactions of Photochromic Diarylethene Derivatives with Low Reaction Yields Upon One-Photon Visible Excitation. *Photochemical and Photobiological Sciences 9*, 172–180.

[12] Terao, F., Morimoto, M., and Irie, M. (2012) Light-Driven Molecular-Crystal Actuators: Rapid and Reversible Bending of Rodlike Mixed Crystals of Diarylethene Derivatives. *Angew Chem Int Ed Engl 51*, 901–904.

[13] Nakamura, S., Uchida, K., and Hatakeyama, M. (2013) Potential Energy Surfaces and Quantum Yields for Photochromic Diarylethene Reactions. *Molecules 18*, 5091–5103.

[14] Czaja, A. U., Trukhan, N., and Muller, U. (2009) Industrial Applications of Metal-Organic Frameworks. *Chemical Society Reviews 38*, 1284–1293.

[15] Chae, H. K., Siberio-Perez, D. Y., Kim, J., Go, Y., Eddaoudi, M., Matzger, A. J., O'Keeffe, M., and Yaghi, O. M. (2004) A Route To High Surface Area, Porosity and Inclusion of Large Molecules in Crystals. *Nature 427*, 523–527.

[16] Takami, S., Kawai, T., and Irie, M. (2002) Photochromism of Dithiazolylethenes Having Methoxy Groups At the Reaction Centers. *European Journal of Organic Chemistry* 3796–3800.

[17] Hania, P. R., Pugzlys, A., Lucas, L. N., de Jong, J. J. D., Feringa, B. L., van Esch, J. H., Jonkman, H. T., and Duppen, K. (2005) Ring Closure Dynamics of BTE-Based Photochromic Switches: Perfluoro- Versus Perhydrocyclopentene Derivatives. *Journal of Physical Chemistry A 109*, 9437–9442.

[18] Hania, P. R., Telesca, R., Lucas, L. N., Pugzlys, A., van Esch, J., Feringa, B. L., Snijders, J. G., and Duppen, K. (2002) An Optical and Theoretical Investigation of the Ultrafast Dynamics of a Bisthienylethene-Based Photochromic Switch. *Journal of Physical Chemistry A 106*, 8498–8507.

Chapter 7

Conclusions

In this dissertation, we have used a combination of vibrational and electronic spectroscopies to understand the excited state dynamics of several photoactive molecules. These molecules include three three photochromic molecular switches, 1,2-bis(2,4-dimethyl-5-phenyl-3-thienyl) perfluorocyclopentene (DMPT-PFCP), 9,10-bis(2,5-dimethylthiophen-3-yl)-phenanthrene-2,7-dicarboxylate (TPDC), and 4,4'-(1-methyl-1H-indole-2,3-diyl)bis(5-methyl-2-phenylthiazole) (DTA), and a phenylthionphene derivative, 2,5-diphenylthiophene. The resonant femtosecond stimulated Raman spectroscopy (R-FSRS) experiments used in portions of this dissertation represent some of the first time-resolved excited-state resonance Raman spectra collected in our lab.[1] Furthermore, these are among the first examples of transient resonance Raman used to study electronic excited-states above S_1 using the electronic transition from the S_1 state.

The wavelength dependent resonant femtosecond stimulated Raman spectroscopy (R-FSRS) study of DPT in this dissertation demonstrated that the excited-state Raman spectra are sensitive to the resonance condition. The mode dependent enhancements associated with the resonant excited-state (S_n) show that the electronic transition corresponds to motions along the C-S-C bending and symmetric stretching coordinates. This conclusion is manifest in excitation profiles for these C-S-C vibrational modes which demonstrate enhancements greater than the relative increase in electronic transition strength. The additional presence of combination and overtone bands involving these C-S-C vibrations point to significant displacements between electronic potentials in these particular vibrational coordinates. Moving forward, similar information is theoretically accessible through the depolarization ratios of the excited-state Raman spectrum. However, the increasing density of states and experimental difficultly of R-FSRS measurements make measurements of the

depolarization ratio challenging.

Also, the simulation of the excited-state resonant Raman spectra of DPT, based on the time-dependent resonance Raman formalism, produced results that captured the main features of the experimental spectra. However, the quality of agreement between experimental and simulated spectra proved to depend on the level of theory used in the calculations with higher level theories providing better agreement in a handful of key vibrational modes.

By applying the similar theoretical approach used to interpret the excited-state Raman spectra of DPT, the R-FSRS spectrum of DMPT-PFCP was collected to track the dynamic behavior of the cycloreversion reaction. DMPT-PFCP has a rich history of spectroscopic study,[2–5] but the direct probing of its higher-lying excited-states has not been the focus of any previous studies. Work using pump-probe (PP) and pump-repump-probe (PReP) spectroscopies have taken advantage of different excited-state absorptions and shown the different electronic transitions produce different effects on the cycloreversion reaction yield.[2,3]

R-FSRS experiments using a 400 nm Raman pump pulse reveals a spectrum that is dominated by excited-state vibrations with delocalized motions that then decay on a $\sim$2.4 ps timescale. Importantly, the electronic spectroscopy and the bleach of the ground-state vibrational spectrum have a second component $\sim$7.2 ps. These two time-constants correspond to a previously observed excited-state barrier crossing and excited-state population decay, respectively.[2] These timescales point to the excited-state barrier crossing also corresponding to a change in the electronic character of the system or reduced polarizability of the system. As the conical intersection between the S_1 and S_0 states exists at a configuration somewhere between the open-ring and closed-ring isomers of DMPT-PFCP, the system is proposed to adopt a less conjugated electronic structure with rehybridization of the central cyclohexadiene ring. This is of particular interest because this behavior is not observed in measurements resonant with a different excited-state transition at 800 nm. A key result of this comparison is that when using a resonant transition to study the S_1 dynamics, the resonant electronic state can impact the dynamics that the experiment is sensitive to. Further refinement of the R-FSRS measurements could provide vibrational signatures of the intermediate

excited-state species. Due to the significant differences in the bonding structure between the open- and closed-ring isomers, detection of only a few key open-ring isomer vibrational modes would prove useful in describing the structure of DMPT-PFCP near the conical intersection.

While the experiments with DPT and DMPT-PFCP show that the use of established resonance Raman formalisms works to interpret the excited-state spectroscopy, additional work should still consider the complications of Duschinsky rotations and Herzberg-Teller coupling. The work presented in this dissertation ignore these effects on the resonant excited-state spectra, possible complications due to Duschinsky rotations and Herzberg-Teller coupling are more likely in dynamic systems. As an important extension of this work, understanding these effects, especially in the context of an evolving system, provide additional information about how multiple higher-lying electronic states interact and change the dynamics on the S_1 potential energy surface.

The impact of higher-lying excited-states can also be addressed by direct excitation using shorter wavelength pump pulses with PP experiments. This approach was used to study the cyclization reaction of DMPT-PFCP at a series of excitation wavelengths. In DMPT-PFCP the transitions with large oscillator strength relate to the phenylthiophene side groups. However, the HOMO$\rightarrow$LUMO transition is calculated to transfer electron density to the cyclopentane ring. Pumping the system at 335 nm, using this transition, does not provide a distinct difference in the cyclization yield, compared to excitation at 308 nm. When comparing excitations at 266, 308 and 335 nm, the basic structure of the spectrum is similar. However, at long time delays, the relative signal intensities across each spectrum show different contributions from long-lived species. One of these long-lived species is the closed-ring product and a second is the triplet species which is formed primarily by open-ring species that are not able to execute the photo-induced cyclization. The difference in the spectra for each pump wavelength emerge within the first ps after excitation. By attributing this to sub-picosecond dynamics, we confirm the proposal by Hambi et al. that there is an ultrafast mechanism for triplet formation.[6] Furthermore, because the picosecond dynamics remain relatively unchanged, this provides indirect evidence that a competitive channel between triplet formation and cyclization. While R-FSRS measurements have been performed on

DMPT-PFCP studying the signatures of the long lived species,[7] a systematic study with changing actinic pulse wavelengths could reveal direct spectroscopic evidence and further insight into the sub-picosecond dynamics of the photoswitch.

Additional PP experiments on TPDC and DTA demonstrate how functionalizing diarylethene-based photoswitches can substantially impact the cyclization and cycloreversion dynamics of the system. TPDC while demonstrates bulk switching in solution, shows a limited efficiency of cyclization and cycloreversion on the picosecond timescale. In particular, the transient spectroscopy of the cyclization shows only minor changes which are assigned as cooling of the excited-state species. Due to the change in bonding patterns between the open- and close-ring species it is likely that the partial breaking of the aromatic character of the phenanthrene moiety induces a sizeable excited state barrier along the cyclization coordinate. This excited-state barrier then slows the rate beyond the scope of our experiments.

In the cycloreversion reaction of TPDC, only vibrational cooling and excited state decay are observed. The regions where the ground-state bleach is observed show a minor offset and long time delays, but indicate that there is not a particularly strong driving force for the formation of the open-ring isomer. Performing additional calculations to map the reaction path of TPDC would help strengthen our experimental conclusions.

For DTA, the experimental focus was limited to the cyclization reaction since its weak intramolecular hydrogen bonding is intended to eliminate the non-reactive open-ring conformer. While both DMPT-PFCP and TPDC generated long-lived species other than the cyclization product, the long-delay spectrum of DTA is well represented by the static absorption spectrum of the closed-ring isomer. Furthermore, the spectral evolution of DTA is complete within $\sim$2 ps and lacks common signatures of internal conversion found in the non-reactive conformers of other diarylethene-based systems. These results allow us to conclude that the weak intramolecular hydrogen bonding effectively eliminates the contribution of non-reactive isomers to the transient absorption spectrum. However, the and thiazole substitutions into the basic diarylethene-based photoswitch structure are not as well studied as the thiophene and benzothiophene derivatives.

The study of analogous systems to DTA which lack the hydrogen bonding would provide further clarity of the role of the aryl groups in this class of molecules.

This dissertation demonstrates the use of a combination of PP and R-FSRS spectroscopies along with previous work using PReP, to further develop a fundamental understanding of the role of higher-lying excited-states. The information provided by R-FSRS measurements is complementary to PReP results, by providing a means to directly probe the forces which excitation to higher-lying electronic states applies to the system. Additionally, we have shown new insights into the cyclization and cycloreversion reactions of DMPT-PFCP. This work also provides spectroscopic benchmarks for further computational studies aiming to simulate resonance Raman spectra in the excited-state.

7.1 Bibliography

[1] Barclay, M. S.; Quincy, T. J.; Williams-Young, D. B.; Caricato, M.; Elles, C. G. *Journal of Physical Chemistry A* **2017**, *121*, 7937–7946.

[2] Ward, C. L.; Elles, C. G. *Journal of Physical Chemistry Letters* **2012**, *3*, 2995–3000.

[3] Ward, C. L.; Elles, C. G. *The Journal of Physical Chemistry A* **2014**, *118*, 10011–10019.

[4] Ward, C. L.; Houk, A. L.; Elles, C. G. *Abstracts of Papers of the American Chemical Society* **2013**, *245*, 1.

[5] Ishibashi, Y.; Okuno, K.; Ota, C.; Umesato, T.; Katayama, T.; Murakami, M.; Kobatake, S.; Irie, M.; Miyasaka, H. *Photochemical and Photobiological Sciences* **2010**, *9*, 172–180.

[6] Hamdi, I.; Buntinx, G.; Perrier, A.; Devos, O.; Jaïdane, N.; Delbaere, S.; Tiwari, A. K.; Dubois, J.; Takeshita, M.; Wada, Y.; Aloïse, S. *Physical Chemistry Chemical Physics* **2016**, *18*, 28091–28100.

[7] Pontecorvo, E.; Ferrante, C.; Elles, C. G.; Scopigno, T. *Journal of Physical Chemistry B* **2014**, *118*, 6915–6921.